SRNL-STI-2010-00805
Revision 0

Keywords: *High level waste glass, structure, durability*

Retention: *Permanent*

Summary of 2010 DOE EM International Program Studies of Waste Glass Structure and Properties

K. M. Fox
A. S. Choi
J. C. Marra
A. L. Billings
S. V. Stefanovsky

December 2010

Savannah River National Laboratory
Savannah River Nuclear Solutions, LLC
Aiken, SC 29808

Prepared for the U.S. Department of Energy under contract number DE-AC09-08SR22470.

DISCLAIMER

Printed in the United States of America

Prepared for
U.S. Department of Energy

REVIEWS AND APPROVALS

AUTHORS:

K. M. Fox, Process Technology Programs	Date
A. S. Choi, Engineering Process Development	Date
J. C. Marra, DOE-EM Office of Technology Innovation and Development	Date
A. L. Billings, Process Technology Programs	Date

TECHNICAL REVIEW:

D. K. Peeler, Process Technology Programs	Date

APPROVAL:

C. C. Herman, Manager Process Technology Programs	Date
A. B. Barnes, Manager Engineering Process Development	Date
S. L. Marra, Manager Environmental & Chemical Process Technology Research Programs	Date

ACKNOWLEDGEMENTS

The authors would like to thank Dr. Fabienne Johnson for assistance with glass composition selection and data interpretation, Irene Reamer, Phyllis Workman, David Best, Patricia Simmons, Whitney Riley, and David Missimer for assistance with fabricating and characterizing the study glasses, and Dr. Tanya Albert for skilled translations. The twelve glass samples used for Task 3 were prepared by Don Miller, and his efforts are greatly appreciated. The authors also acknowledge the International Program and the EM-31 Technology Development & Deployment (TDD) Program at the U.S. Department of Energy Office of Environmental Management for financial support of this work.

EXECUTIVE SUMMARY

Collaborative work between the Savannah River National Laboratory (SRNL) and SIA Radon in Russia was divided among three tasks for calendar year 2010. The first task focused on the study of simplified high level waste glass compositions with the objective of identifying the compositional drivers that lead to crystallization and poor chemical durability. The second task focused on detailed characterization of more complex waste glass compositions with unexpectedly poor chemical durabilities. The third task focused on determining the structure of select high level waste glasses made with varying frit compositions in order to improve models under development for predicting the melt rate of the Defense Waste Processing Facility (DWPF) glasses.

The majority of these tasks were carried out at SIA Radon. Selection and fabrication of the glass compositions, along with chemical composition measurements and evaluations of durability were carried out at SRNL and are described in this report. SIA Radon provided three summary reports based on the outcome of the three tasks. These reports are included as appendices to this document.

Briefly, the result of characterization of the Task 1 glasses may indicate that glass compositions where iron is predominantly tetrahedrally coordinated have more of a tendency to crystallize nepheline or nepheline-like phases. For the Task 2 glasses, the results suggested that the relatively low fraction of tetrahedrally coordinated boron and the relatively low concentrations of Al_2O_3 available to form $[BO_{4/2}]^-Me^+$ and $[AlO_{4/2}]^-Me^+$ tetrahedral units are not sufficient to consume all of the alkali ions, and thus these alkali ions are easily leached from the glasses.

All of the twelve Task 3 glass compositions were determined to be mainly amorphous, with some minor spinel phases. Several key structural units such as metasilicate chains and rings were identified, which confirms the current modeling approach for the silicate phase. The coordination of aluminum and iron was found to be mainly tetrahedral, with some octahedral iron ions. In all samples, trigonally-coordinated boron was determined to dominate over tetrahedrally-coordinated boron. The results further suggested that BO_4 tetrahedra and BO_3 triangles form complex borate units and may be present as separate constituents. However, no quantification of tetrahedral-to-trigonal boron ratio was made.

TABLE OF CONTENTS

LIST OF TABLES

LIST OF ABBREVIATIONS

AD	Analytical Development
ARM	Approved Reference Material
CCC	Canister Centerline Cooling
CT	Computed Tomography
DSC	Differential Scanning Calorimeter
DWPF	Defense Waste Processing Facility
EA	Environmental Assessment
EDS	Energy Dispersive Spectroscopy
EPR	Electron Paramagnetic Resonance
EXAFS	Extended X-ray Absorption Fine Structure
HLW	High Level Waste
ICP-AES	Inductively Coupled Plasma – Atomic Emission Spectroscopy
IR	Infrared
LM	Lithium Metaborate
NL	Normalized Leachate
NMR	Nuclear Magnetic Resonance
PCT	Product Consistency Test
PF	Peroxide Fusion
PSAL	Process Science Analytical Laboratory
SB6	Sludge Batch 6
SEM	Scanning Electron Microscopy
SRNL	Savannah River National Laboratory
SRS	Savannah River Site
XANES	X-ray Absorption Near Edge Spectroscopy
XPS	X-ray Photoelectron Spectroscopy
XRD	X-ray Diffraction

1.0 Introduction

The Savannah River National Laboratory (SRNL) performs extensive development work on immobilization of high level waste (HLW) in glass. The applied nature of this work dictates that the glass compositions are very complex, and therefore characterization of the glass structure becomes difficult. A study of simplified glass compositions would be useful in providing insight into the performance of the more complex glasses while making characterization data easier to interpret. For example, the formation of nepheline crystals in complex glass compositions, which reduces the chemical durability of the glass waste form, may be easier to understand by characterizing a simplified composition.

The structure of Al_2O_3-B_2O_3-Na_2O-SiO_2 glasses has been reported in the literature using Nuclear Magnetic Resonance (NMR) and optical characterization techniques (see Pierce *et al.* for a brief review[1]). The published work has been successful in identifying compositionally driven coordination changes in aluminum and boron, changes in the fraction of non-bridging oxygens, and the tendency for sodium to preferentially associate with aluminum. However, the addition of iron – a major component of high level waste glass at the Savannah River Site (SRS) – makes NMR studies difficult. Therefore, the first task of this international, collaborative study was developed to characterize the chemistry and structure of Al_2O_3-B_2O_3-Na_2O-SiO_2 glasses with the addition of Fe_2O_3 using a unique suite of characterization tools at SIA Radon in Russia. These tools include Scanning Electron Microscopy with Energy Dispersive Spectroscopy (SEM/EDS), Infrared (IR) and Raman Spectroscopy, X-ray Absorption Near Edge Structure (XANES), and Extended X-ray Absorption Fine Structure (EXAFS). As described later in this report, simplified versions of several glass compositions based on SRS HLW glasses are selected and characterized, and the results are used to help identify compositional factors influencing crystallization and chemical durability.

A second task of this collaborative study is to investigate more complex glass compositions that have exhibited unexpected performance. SRNL has identified a small number of simulated, multi-component waste glass compositions that, while amorphous via XRD, have unusually poor chemical durability. The cause of the reduction in durability is not known, but is suspected to be amorphous phase separation. The objective of this task is to recreate three of the previously identified glass compositions and characterize them using SEM in an attempt to screen for amorphous phase separation. If phase separation can be identified using SEM, EDS will be used to approximate the compositions of each phase. IR and Raman Spectroscopy will also be used in order to identify any changes in the chemistry and structure of these anomalous glasses and possibly each phase.

The third task in this collaborative study is to provide glass structural data for full DWPF glass compositions to support the development of predictive models for the melting behavior of glass. SRNL has developed several models of the processes occurring as a glass batch is converted to a melt,[2] although additional glass structural data are needed to improve these models. This portion of the study will apply the insight gained from the first task in studying the impact of varying levels of boron, alkali, and some additives such as Ca and Mn on the coordination chemistry of simulated HLW glass systems using X-ray Photoelectron Spectroscopy (XPS), XANES, EXAFS, Electron Paramagnetic Resonance (EPR), and IR and Raman spectroscopy. The sample glass compositions for this task have been made using simulated Defense Waste Processing Facility (DWPF) Sludge Batch 6 (SB6) simulant (high in both Al and Fe concentrations) with 12 different frit compositions at a constant waste loading of 36 wt %. The baseline frit composition is Frit 418 and the remaining frit compositions contain 8-16 wt % B_2O_3, 4-8 wt % Na_2O, 0-4 wt % MnO and

0-2 wt % CaO. The rate of melting of these various sludge and frit combinations has been measured at SRNL using visual as well as X-ray imaging and Computed Tomography (CT) techniques. The structural information determined at SIA Radon will be used to link the melt rate performance with the composition and structure of these glasses.

2.0 Experimental Procedure

2.1 Selection of Glass Compositions

Glasses for Task 1 were selected based on a range of compositions of interest for SRS HLW. SB6 was being prepared for processing at the DWPF when this study was initiated, and therefore was selected as the first composition. SB19, which was projected to be the last sludge batch processed at the DWPF, and which also has a significantly different composition than SB6, was selected as the next composition of interest. Previous work on a glass composition identified as 121506-07 showed that while this composition was predicted to form nepheline crystals with a subsequent reduction in chemical durability, it was in fact free of nepheline with good durability.[3] This composition is therefore of interest since a better understanding of its structure may aid future efforts in preventing nepheline crystallization. An additional SB19 composition was also selected, and combined with a frit composition where all of the Na_2O has been removed and replaced with B_2O_3. The compositions of each of these four glasses were simplified by eliminating all of the components except for Al_2O_3, B_2O_3, Fe_2O_3, Na_2O, and SiO_2, and then normalizing the concentrations of these remaining components to 100 wt %. A second version of each of these glasses was developed by removing the Fe_2O_3 component, and again normalizing the concentrations of the remaining components to 100 wt %. This will provide for the opportunity to specifically study the impact of Fe_2O_3. The target compositions for these glasses are given in Table 2-1.

Glasses for Task 2 were selected from a previous study of glasses for enhanced melter throughput.[4] These glasses were found to be free of any crystallization detected by X-ray Diffraction (XRD), but had unexpectedly poor durabilities. The target compositions of these glasses are given in Table 2-2.

The glass compositions selected for Task 3 were prepared as part of the EM-31 melt rate program. The composition of the SB6 simulant used is the same as that used for the DWPF melter bubbler demonstration tests (Table 2-3);[5] it contained neither Hg nor noble metals. The twelve frit compositions tested in conjunction with the SB6 simulant are given in Table 2-4. The theoretical compositions of the resulting glasses are included in the report from SIA Radon in Appendix C.

Table 2-1. Target Compositions for the Task 1 Glasses.

Glass ID	Composition	Al_2O_3 (wt %)	B_2O_3 (wt %)	Fe_2O_3 (wt %)	Na_2O (wt %)	SiO_2 (wt %)
A1	Simplified SB6 Glass	12.46	5.00	11.48	22.27	48.79
A2	Simplified SB6 Glass, without Iron	14.14	5.90	0.00	25.32	54.64
B1	Simplified SB19 Glass	21.07	4.03	11.66	25.18	38.07
B2	Simplified SB19 Glass, without Iron	24.06	4.62	0.00	28.34	42.98
C1	Simplified 121506-07 Glass	34.62	23.28	8.21	6.38	27.51
C2	Simplified 121506-07 Glass, without Iron	37.72	25.29	0.00	7.09	29.91
D1	Simplified SB19 Glass with High B_2O_3 Frit	20.91	8.09	12.01	21.19	37.79
D2	Simplified SB19 Glass with High B_2O_3 Frit, without Iron	23.94	9.19	0.00	24.10	42.76

Table 2-2. Target Compositions for the Task 2 Glasses (wt %).

Oxide	FY09EM21-02	FY09EM21-07	FY09EM21-21
Al_2O_3	4.01	4.87	4.86
B_2O_3	5.07	13.92	9.01
BaO	0.08	0	0.08
CaO	0	3.92	0
CdO	0.3	0	0.3
Ce_2O_3	0.36	0	0.36
Cr_2O_3	0	0	0.2
CuO	0.13	0	0.13
Fe_2O_3	20.63	17.98	19.95
La_2O_3	0.1	0	0.1
Li_2O	4	4	7
MgO	1.5	1.5	0
MnO	0.3	5.5	1
Na_2O	17.98	12.71	14.67
NiO	2.5	0	0
PbO	0.22	0	0.22
SO_4	0.48	0	0.48
SiO_2	40.02	33.6	39.31
TiO_2	2	2	2.01
ZnO	0.13	0	0.13
ZrO_2	0.21	0	0.21

Table 2-3. Composition of DWPF SB6 Simulant used in Task 3.

Elements	wt %	Oxides	wt %
Fe	18.9	Fe_2O_3	27.0218
Al	15.9	Al_2O_3	29.9505
Mn	5.92	MnO	7.6441
Ca	0.949	CaO	1.3271
Mg	0.454	MgO	0.7526
P	<0.100	P_2O_5	0.0000
Ni	2.54	NiO	3.2318
Cr	-	Cr_2O_3	-
Cu	0.181	CuO	0.2266
Ti	0.014	TiO_2	0.0234
Si	0.141	SiO_2	0.3006
Na	15.4	Na_2O	20.7589
Zn	0.00	ZnO	0.0000
K	0.07	K_2O	0.0843
Ce	<0.010	Ce_2O_3	-
Sr	0.049	SrO	0.0579
Ba	<0.010	BaO	-
Pb	<0.010	PbO	-
La	<0.010	La_2O_3	-
Zr	0.217	ZrO_2	0.2924
S	0.37	SO_3	0.9240
Total	61.054	Total	92.5959

Table 2-4. Composition of Frits Used in Task 3 (wt%).

Frit	**418**	**510**	**CEF1**	**CEF2**	**CEF3**	**CEF4**	**CEF5**	**CEF6**	**CEF7**	**CEF8**	**CEF9**	**CEF10**
B_2O_3	8	14	11	11	11	8	8	8	8	8	8	16
CaO	0	0	0	0	0	0	0	0	2	2	2	0
Li_2O	8	8	8	8	9	8	8	8	8	8	8	8
MnO	0	0	0	2	4	1	2	4	1	2	4	0
Na_2O	8	8	8	6	5	8	7	6	7	6	6	4
SiO_2	76	70	73	73	71	75	75	74	74	74	72	72
Total	100	100	100	100	100	100	100	100	100	100	100	100
MRF Run # (10-xxx)	35	36	37	38	39	40	41	42	43	44A	45	46

2.2 Fabrication of Glasses

Each of the glasses for Tasks 1 and 2 were prepared from the proper proportions of reagent-grade metal oxides, carbonates, and boric acid in 150 g batches. The raw materials were thoroughly mixed and placed into platinum/gold, 250 ml crucibles. The batch was placed into a high-temperature furnace at the melt temperatures shown in Table 2-5. The crucible was removed from the furnace after an isothermal hold for 60 minutes. The glasses were poured onto clean, stainless steel plates and allowed to air cool (quench). Glasses D1 and D2 were melted for only 30 minutes to reduce volatilization at the high melting temperature. Glasses C1 and C2 would not melt at the maximum furnace temperature of 1550 °C, and therefore were eliminated from the rest of the study.

Approximately 25 g of each glass was heat-treated to simulate cooling along the centerline of a DWPF-type canister[6] to gauge the effects of thermal history on the product performance. This cooling schedule is referred to as the CCC heat treatment.

Portions of each glass were annealed in order to produce stress-free samples for the structural characterization at SIA Radon. The annealing temperatures for each composition were determined by using a Differential Scanning Calorimeter (DSC) to determine the glass transition temperature for each composition, and then subtracting approximately 5 °C from this value. The glasses were annealed at these temperatures, given in Table 2-5, for approximately 4 hours and then slowly cooled.

Table 2-5. Melt and Annealing Temperatures for the Task 1 and 2 Glass Compositions.

Glass ID	Composition	Melt Temperature (°C)	Annealing Temperature (°C)
A1	Simplified SB6 Glass	1350	520
A2	Simplified SB6 Glass, without Iron	1350	520
B1	Simplified SB19 Glass	1450	505
B2	Simplified SB19 Glass, without Iron	1500	505
C1	Simplified 121506-07 Glass	-*	-
C2	Simplified 121506-07 Glass, without Iron	-*	-
D1	Simplified SB19 Glass with High B_2O_3 Frit	1500	525
D2	Simplified SB19 Glass with High B_2O_3 Frit, without Iron	1500	525
FY09EM21-02	From FY09 EM Study	1150	425
FY09EM21-07	From FY09 EM Study	1150	425
FY09EM21-21	From FY09 EM Study	1150	425

*Glasses C1 and C2 would not melt at 1550 °C.

The glass samples for Task 3 were prepared by fusing the blend of dried SB6 simulant and the frit in the Melt Rate Furnace (MRF). When the MRF reached the target temperature of 1,150 °C, a stainless steel beaker containing enough sludge and frit to make 50-60 g of glass at a target waste loading of 36 wt% was lowered into the MRF and heated from the bottom for ~20 min. After the beaker was removed from the furnace, any loose material not yet fully melted was poured out, and the remaining 30-40 g of glass and froth materials were collected for shipment to SIA Radon.

2.3 Composition Analysis

To confirm that the as-fabricated glasses met the target compositions, a representative sample from each quenched glass was submitted to the SRNL Process Science Analytical Laboratory (PSAL) for chemical analysis. Two dissolution techniques, sodium peroxide fusion (PF) and lithium-metaborate (LM), were used to prepare the glass samples for analysis. Each of the samples was analyzed, twice for each element of interest, by Inductively Coupled Plasma – Atomic Emission Spectroscopy (ICP-AES).

2.4 X-Ray Diffraction Analysis

Representative samples of each of the Task 2 quenched and CCC glasses were submitted to SRNL Analytical Development (AD) for XRD analysis. Samples were run under conditions providing a detection limit of approximately 0.5 vol %. That is, if crystals (or unincorporated batch material) were present at 0.5 vol % or greater, the diffractometer would not only be capable of detecting the crystals but would also allow a qualitative determination of the type of crystal(s) present. Otherwise, a characteristically high background signal (amorphous hump) devoid of crystalline peaks indicates that the glass is free of crystallization, suggesting either a completely amorphous product or that the degree of crystallization is below the detection limit.

2.5 Product Consistency Test

The Product Consistency Test (PCT) Method-A[7] was performed in triplicate on each quenched and CCC glass to assess chemical durability. Also included in the experimental test matrix was the Environmental Assessment (EA) benchmark glass,[8] the Approved Reference Material (ARM) glass,[9] and blanks from the sample cleaning batch. Samples were ground, washed, and prepared according to the standard procedure.[7] Fifteen milliliters of Type-I ASTM water were added to 1.5 g of glass in stainless steel vessels. The vessels were closed, sealed, and placed in an oven at 90 ± 2 °C where the samples were maintained at temperature for 7 days. Once cooled, the resulting solutions were sampled (filtered and acidified), then labeled and analyzed by PSAL using ICP-AES. Normalized leachate (NL) values were calculated based on the targeted compositions using the average of the common logarithms of the leachate concentrations.

2.6 Structural Characterization

Detailed characterization of the structure of the glasses was carried out at SIA Radon. These results and their interpretation are provided in the reports included as appendices in this document. Appendix A describes the results for the Task 1 glasses, Appendix B describes the results for the Task 2 glasses, and Appendix C describes the results for the Task 3 glasses.

3.0 Results and Discussion

3.1 Composition Analysis

The results of the chemical composition measurements for the Task 1 glass compositions are shown in Table 3-1. The measured values are the mean of two measurements from the ICP-AES instrument. The targeted concentrations and the percent difference between the targeted and measured values are also given in the table. The B_2O_3 and the Na_2O concentrations are slightly low for each of the glasses, which is likely due to volatility during melting. The Fe_2O_3 concentration is low for glass A1. These issues are not expected to impact the outcome of the study.

The results of the chemical composition measurements for the Task 2 glasses are shown in Table 3-2. It appears that NiO was omitted from the batch for glass FY09EM21-02. The MnO concentration is low for glass FY09EM21-07. The Fe_2O_3 concentration is high for glass FY09EM21-21. Again, these issues are not expected to impact the outcome of the study.

Table 3-1. Target and Measured Compositions of the Task 1 Glasses (wt %).

Glass ID	Al_2O_3 (wt %)			B_2O_3 (wt %)			Fe_2O_3 (wt %)			Na_2O (wt %)			SiO_2 (wt %)		
	Target	**Meas.**	**Diff.**	**Target**	**Meas.**	**Diff.**	**Target**	**Meas.**	**Diff.**	**Target**	**Meas.**	**% Diff.**	**Target**	**Meas.**	**Diff.**
A1	12.46	12.50	0.3%	5.00	4.88	-2.5%	11.48	10.35	-9.8%	22.27	21.42	-3.8%	48.79	48.31	-1.0%
A2	14.14	14.31	1.2%	5.90	5.57	-5.5%	0.00	-	-	25.32	23.80	-6.0%	54.64	54.33	-0.6%
B1	21.07	21.00	-0.3%	4.03	3.79	-5.9%	11.66	11.08	-5.0%	25.18	24.04	-4.5%	38.07	38.03	-0.1%
B2	24.06	24.05	0.0%	4.62	4.35	-5.9%	0.00	-	-	28.34	26.79	-5.5%	42.98	43.32	0.8%
D1	20.91	20.63	-1.3%	8.09	7.73	-4.4%	12.01	12.55	4.5%	21.19	20.24	-4.5%	37.79	37.36	-1.1%
D2	23.94	23.51	-1.8%	9.19	8.98	-2.3%	0.00	-	-	24.10	22.96	-4.7%	42.76	42.34	-1.0%

Table 3-2. Target and Measured Compositions of the Task 2 Glasses (wt %).

Oxide	FY09EM21-02			FY09EM21-07			FY09EM21-21		
	Target	**Meas.**	**% Diff.**	**Target**	**Meas.**	**% Diff.**	**Target**	**Meas.**	**% Diff.**
Al_2O_3	4.01	4.31	7%	4.87	5.07	4%	4.86	4.75	-2%
B_2O_3	5.07	5.29	4%	13.92	13.75	-1%	9.01	8.77	-3%
BaO	0.08	0.08	-2%	0.00	-	-	0.08	0.07	-12%
CaO	0.00	-	-	3.92	3.88	-1%	0.00	-	-
CdO	0.30	0.28	-8%	0.00	-	-	0.30	0.27	-11%
Ce_2O_3	0.34	0.34	0%	0.00	-	-	0.32	0.32	0%
Cr_2O_3	0.00	-	-	0.00	-	-	0.20	0.20	2%
CuO	0.13	0.14	6%	0.00	-	-	0.13	0.13	-4%
Fe_2O_3	20.63	22.24	8%	17.98	17.88	-1%	19.95	23.40	17%
La_2O_3	0.10	0.09	-12%	0.00	-	-	0.10	0.08	-17%
Li_2O	4.00	3.98	0%	4.00	3.88	-3%	7.00	6.63	-5%
MgO	1.50	1.51	1%	1.50	1.47	-2%	0.00	-	-
MnO	0.30	0.33	11%	5.50	4.36	-21%	1.00	1.01	1%
Na_2O	17.98	18.00	0%	12.71	12.49	-2%	14.67	13.68	-7%
NiO	2.50	0.00	-100%	0.00	-	-	0.00	-	-
PbO	0.22	0.21	-2%	0.00	-	-	0.22	0.21	-6%
SO_4	0.48	0.55	14%	0.00	-	-	0.48	0.53	9%
SiO_2	40.02	38.73	-3%	33.60	32.21	-4%	39.31	36.17	-8%
TiO_2	2.00	1.97	-2%	2.00	1.90	-5%	2.01	1.84	-8%
ZnO	0.13	0.13	3%	0.00	-	-	0.13	0.12	-8%
ZrO_2	0.21	0.20	-4%	0.00	-	-	0.21	0.19	-9%

3.2 XRD Results

The XRD results for the quenched and CCC versions of the Task 2 glasses are shown in Table 3-3. All of the quenched glasses were XRD amorphous. Magnetite was identified in the CCC version of glass FY09EM21-07. Lithium silicate was identified in glass FY09EM21-21. Based on previous experience, magnetite will not likely impact the durability of the glass while lithium silicate is more likely to be detrimental.

Table 3-3. XRD Results for the BP-Series Glasses.

Glass ID	Heat Treatment	XRD Results
FY09EM21-02	Quenched	Amorphous
	CCC	Amorphous
FY09EM21-07	Quenched	Amorphous
	CCC	Magnetite (Fe_3O_4)
FY09EM21-21	Quenched	Amorphous
	CCC	Lithium Silicate (Li_2SiO_3)

3.3 PCT Results

The PCT results for the Task 1 and Task 2 glasses are listed in Table 3-4. A review of the data showed no issues with the blank vessels, no issues with the ARM reference glass, no water loss issues, and no issues with the surface to volume ratios of the study glasses. The PCT values are normalized based on the targeted glass compositions. Composition B1 has the highest normalized leachate concentration for boron (NL [B]) among the Task 1 glasses, with a value of 1.10 g/L. This may be due to the carnegieite phase identified in this composition at SIA Radon (see Appendix A). Overall, the durabilities of the Task 1 glass compositions are considerably better than that of the EA reference glass.

As reported in the original study from which the Task 2 glasses were selected,[4] the durabilities of these glasses are relatively poor. In particular, composition FY09EM21-21 has a durability that is worse than that of the EA reference glass. The identification of lithium silicate in the CCC version of this glass by XRD (see Section 3.2) may indicate the cause of poor durability for this composition. Lithium silicate removes silicon, a glass network former, from the residual amorphous phase. The XRD results do not explain the durability results of the other two Task 2 glasses. Composition FY09EM21-02 was found to be XRD amorphous. Composition FY09EM21-07 contained magnetite after slow cooling, which is not expected to impact durability. The intent of the study at SIA Radon was to further investigate the potential causes of these poor durability values (see Appendix B).

Table 3-4. PCT Results for the Task 1 and Task 2 Glasses.

Glass ID	Heat Treatment	NL [B] (g/L)	NL [Li] (g/L)	NL [Na] (g/L)	NL [Si] (g/L)
EA	n/a	15.08	8.58	11.82	3.73
A1	Quenched	0.83	-	0.81	0.42
A2	Quenched	0.78	-	1.29	0.46
B1	Quenched	1.10	-	1.19	0.58
B2	Quenched	0.65	-	1.29	0.49
D1	Quenched	0.54	-	0.62	0.40
D2	Quenched	0.48	-	0.55	0.32
FY09EM21-02	Quenched	3.36	2.30	2.75	2.63
	CCC	5.75	3.32	4.32	1.69
FY09EM21-07	Quenched	12.57	9.74	9.16	1.06
	CCC	3.18	2.62	2.41	0.78
FY09EM21-21	Quenched	19.16	11.38	12.17	3.17
	CCC	27.47	13.07	18.22	3.55

4.0 Summary

The complete Task 1 report from SIA Radon is included as Appendix A. Briefly, microscopy work showed that the glasses were amorphous except for composition B1, which contained carnegieite. No amorphous phase separation was identified. Iron, which is present mainly as Fe^{3+}, was found to reduce the glass network connectivity and increase the number of non-bridging oxygens. Iron ions are well distributed throughout the glasses. The coordination of the iron ions varied as a function of composition. In composition A1, 75% of the iron ions were octahedrally coordinated and 25% were tetrahedrally coordinated. In composition B1, 70% of the iron ions were tetrahedrally coordinated and 30% were octahedrally coordinated. In composition D1, all of the iron ions were octahedrally coordinated. These results may indicate that glass compositions where iron is predominantly tetrahedrally coordinated have more of a tendency to crystallize nepheline or nepheline-like phases.

The complete Task 2 report from SIA Radon is included as Appendix B. Briefly, the glasses were homogeneous and free of both crystalline phases and liquid-liquid phase separation. Composition FY09EM21-02 has the highest degree of glass network connectivity, followed by composition FY09EM21-21 and then by composition FY09EM21-07. Aluminum is tetrahedrally coordinated in all of the glasses. Boron is present in both trigonal and tetrahedral coordinations. The fraction of tetrahedrally coordinated boron is highest for composition FY09EM21-02, and lowest for composition FY09EM21-07. Iron was homogeneously distributed throughout the glasses, and was predominantly trivalent and tetrahedrally coordinated. The report also offers a potential reason for the low chemical durability of these glasses: the relatively low fraction of tetrahedrally coordinated boron and the relatively low concentrations of Al_2O_3 available to form $[BO_{4/2}]^-Me^+$ and $[AlO_{4/2}]^-Me^+$ tetrahedral units are not sufficient to consume all of the alkali ions, and thus these alkali ions are easily leached from the glasses.

The complete Task 3 report from SIA Radon is included as Appendix C. Additional glasses were produced using the same experimental procedures as used for those sent to SIA Radon and characterized at SRNL using X-ray imaging and CT techniques for melt rate evaluation. A report summarizing the CT results of these and other glass samples produced during FY10 under the EM-31 melt rate program is currently being drafted. Briefly, the report in Appendix C showed that all of the Task 3 glass compositions were mainly amorphous, with some minor spinel phases.

Some aggregation of the crystals was identified. The coordination of aluminum and iron was found to be mainly tetrahedral, with some octahedral iron ions (FeO_6). Iron was mainly present as Fe^{3+}. Boron was present mainly in trigonal coordination, along with some tetrahedrally coordinated boron forming complex borate units. SRNL researchers will further evaluate the results of the Task 3 glass studies to determine their impact on melt rate modeling efforts.

5.0 Future Work

Future studies should focus on the role of tetrahedrally coordinated iron in influencing crystallization behavior in glass. It would be useful to determine whether iron is present in a similar local environment in more complex HLW glasses, and to determine whether compositional changes can shift iron into octahedral coordination. In terms of factors influencing durability, further study is needed to better determine the impacts of boron coordination along with aluminum and alkali concentrations on leaching of components from the glass network. It is recommended that a method to quantify the fraction of tetrahedrally-coordinated boron in high-Fe glasses be sought after with a focus on its impact on NBO distribution.

6.0 References

1. Pierce, E. M., L. R. Reed, W. J. Shaw, B. P. McGrail, J. P. Icenhower, C. F. Windisch, E. A. Cordova and J. Broady, "Experimental Determination of the Effect of the Ratio of B/Al on Glass Dissolution Along the Nepheline (NaAlSiO4)-Malinkoite(NaBSiO4) Join," *Geochimica et Cosmochimica Acta,* **74** 2634-2654 (2010).

2. Choi, A. S., "Thermodynamic Modeling of Comparitive Melt Rates: FY08 Summary," *U.S. Department of Energy Report SRNL-PSE-2008-00178,* Savannah River National Laboratory, Aiken, SC (2008).

3. Fox, K. M. and D. K. Peeler, "Demonstration of Very High Aluminum Retention in Simulated HLW Glass," *U.S. Department of Energy Report SRNL-PSE-2007-00231,* Washington Savannah River Company, Aiken, SC (2007).

4. Johnson, F. C. and T. B. Edwards, "Results of the FY09 Enhanced DOE High-Level Waste Melter Throughput Studies at SRNL," *U.S. Department of Energy Report SRNL-STI-2009-00778, Revision 0,* Savannah River National Laboratory, Aiken, SC (2010).

5. Choi, A. S., "DWPF Melter Off-Gas Flammability Assessment," *U.S. Department of Energy Memorandum X-CLC-S-00164, Revision 4,* Savannah River National Laboratory, Aiken, SC (2009).

6. Marra, S. L. and C. M. Jantzen, "Characterization of Projected DWPF Glass Heat Treated to Simulate Canister Centerline Cooling," *U.S. Department of Energy Report WSRC-TR-92-142, Revision 1*, Westinghouse Savannah River Company, Aiken, SC (1993).

7. ASTM, "Standard Test Methods for Determining Chemical Durability of Nuclear Waste Glasses: The Product Consistency Test (PCT)," *ASTM C-1285*, (2002).

8. Jantzen, C. M., N. E. Bibler, D. C. Beam, C. L. Crawford and M. A. Pickett, "Characterization of the Defense Waste Processing Facility (DWPF) Environmental Assessment (EA) Glass Standard Reference Material," *U.S. Department of Energy Report WSRC-TR-92-346, Revision 1,* Westinghouse Savannah River Company, Aiken, SC (1993).

9. Jantzen, C. M., J. B. Picket, K. G. Brown, T. B. Edwards and D. C. Beam, “Process/Product Models for the Defense Waste Processing Facility (DWPF): Part I. Predicting Glass Durability from Composition Using a Thermodynamic Hydration Energy Reaction Model (THERMO),” *U.S. Department of Energy Report WSRC-TR-93-672, Revision 1,* Westinghouse Savannah River Company, Aiken, SC (1995).

Appendix A. Final Report from SIA Radon on Task 1: Chemistry and Structure of Al_2O_3-B_2O_3-Fe_2O_3-Na_2O-SiO_2 Glasses

FINAL REPORT

Subcontract Number AC69549N

Task 1: Chemistry and Structure of Al_2O_3-B_2O_3-Fe_2O_3-Na_2O-SiO_2 Glasses

Glass Structural Characterization and Analysis

INTRODUCTION

SRNL performs extensive development work on immobilization of high level waste in glass. The applied nature of this work dictates that the glass compositions are very complex [1-3], and therefore structural characterization becomes difficult. A study of simplified glass compositions would be useful in providing insight into the performance of the more complex glasses while making characterization data easier to interpret. For example, the formation of nepheline crystals in complex glass compositions, which reduces the chemical durability of the glass waste form [1,2], may be easier to understand by characterizing a simplified composition.

The structure of Al_2O_3-B_2O_3-Na_2O-SiO_2 glasses has been reported in the literature using NMR and optical characterization techniques [4-6]. The published work has been successful in identifying compositionally driven coordination changes in aluminum and boron, changes in the fraction of non-bridging oxygens, and the tendency for sodium to preferentially associate with aluminum. However, the addition of iron (a major component of HLW glass) makes NMR studies difficult. The objective of this task would be to characterize the chemistry and structure of Al_2O_3-B_2O_3-Na_2O-SiO_2 glasses with the addition of Fe_2O_3 using XPS, XANES, EXAFS, IR and Raman Spectroscopy. Comparisons would be made with the literature data, with any additional influences of Fe_2O_3 being identified and described.

EXPERIMENTAL

Samples of glasses were delivered by customer (SRNL). Their target and actual chemical compositions are given in Table I.

Actual chemical compositions of the glasses were determined at SRNL using a Perkin-Elmer 403 ICP-AAS spectrometer. Samples were examined by X-ray diffraction (XRD) using a Rigaku D / Max 2200 diffractometer (Cu Kα radiation, 40 keV voltage, 20 mA current, stepwise 0.02 degrees 2θ), scanning electron microscopy with energy dispersive spectrometry using a JSM-5610LV+JED-2300 analytical unit, Fourier-transform infrared spectroscopy (FTIR) using a Perkin-Elmer 2000 Fourier spectrophotometer (compaction of glass powders in pellets with KBr at recording within the range of 4000-350 cm^{-1}, and placement of micron-sized powder between two glass plates at recording within the range of 600-30 cm^{-1}), and Raman spectroscopy using a Jobin Yvon U1000 spectrophotometer operated at an excitation wavelength of 532 nm.

X-ray absorption (XAS) spectra were recorded at the Structural Materials Science (STM) Beamline of the synchrotron source at RRC “Kurchatov Institute”. The glass samples were measured at room temperature either as dispersed powder or as pellets pressed from powder mixed with sucrose in the transmission mode using a Si(220) channel-cut monochromator and two air-filled ionization chambers. Fluorescence spectra were also acquired. Powders of chemically pure Fe oxides Fe_2O_3 and FeO were used as standards and measured under identical conditions. Experimental XAFS spectra were fitted in R-space using an IFEFFIT package [7] and crystal structures of corresponding oxides and silicates. In the fitting, *ab initio* photoelectron backscattering amplitudes and phases calculated self-consistently using FEFF8 [8] were used.

Wavelet transform (WT) is commonly applied to evaluation of complex time-frequency signals. As shown in refs [9,10], WT is easily adapted to EXAFS analysis, and the expression of the WT of the k^n-weighted EXAFS data takes the form:

$$W_{\chi}^{\psi}(k,r) = (2r)^{1/2} \int_{-\infty}^{\infty} \chi(k')k'^{n}\, \psi^{*}[2r(k'-k)]dk', \qquad (1)$$

where $\chi(k)$ is the EXAFS signal and $\psi^{*}[2r(k'-k)]$ is the complex wavelet function.

The WT is able to resolve the k dependence of the absorption signal, which potentially allows separation of contributing backscattering atoms even situated at the same distances from the core. One of the advantages of the wavelet analysis is the visualization of the WT modulus in a k-R plot, which provides an easy way to interpret the results. Our analysis of EXAFS data for Pu and Hf were performed using the FORTRAN program HAMA employing Morlet wavelet algorithm [11]. The Morlet wavelet is well-suited for EXAFS signal since it consists of a slowly varying amplitude term and a fast oscillating phase term. Its mathematical description is broadly analogous to the Fourier transform. The Morlet wavelet is obtained by taking a complex sine wave with frequency η (as in FT) and by confining it with a Gaussian envelope with the half width σ,

$$\psi(k) = \frac{1}{(2\pi)^{1/2}\sigma} \exp(i\eta k)\exp(-k^2/2\sigma^2). \qquad (2)$$

The choice of the η and σ parameters is important for data analysis since, besides other issues, it determines resolution in k-R space. Various combinations of these parameters were used in an attempt to resolve contributions from atoms at close distances from the central atom. As shown in ref.[8] use of higher k-weighting decreases resolution in the k-space, since backscattering amplitudes become flattened and shifted to higher values. Nevertheless, WT modulus plots for different k weights are shown to emphasize contributions of light and heavy backscatterers. Note, that in all plots of the WT modulus the interatomic distances are given without phase shift correction.

Table I. Chemical Compositions of SRNL Borosilicate Glasses.

Oxides	A1 (SB6)			A2 (SB6 w/o Fe)			B1 (SB19)			B2 (SB19 w/o Fe)			D1 (high B_2O_3 frit)			D2 (high B_2O_3 frit w/o Fe)		
	target		actual	target		actual	target		actual	target		actual	target		actual	target		actual
	mol%	wt.%	wt.%	mol%	wt.%	wt.%	mol%	wt.%	wt.%	mol%	wt.%	wt.%	mol%	wt.%	wt.%	mol%	wt.%	wt.%
Al_2O_3	8.5	12.46	12.50	9.0	14.14	14.30	15.0	21.06	21.00	16.0	24.06	24.05	15.0	20.91	20.60	16.0	23.94	23.50
B_2O_3	5.0	5.00	4.88	5.5	5.90	5.58	4.2	4.03	3.80	4.5	4.62	4.35	8.5	8.09	7.73	9.0	9.19	8.98
Fe_2O_3	5.0	11.48	10.35	-	-	0.08	5.3	11.66	11.05	-	-	0.12	5.5	12.01	12.55	-	-	0.05
Na_2O	25.0	22.27	21.45	26.5	25.31	23.80	29.5	25.18	24.05	31.0	28.34	26.80	25.0	21.19	20.25	26.5	24.10	22.95
SiO_2	56.5	48.80	48.30	59.0	54.64	54.30	46.0	38.07	38.00	48.5	42.98	43.30	46.0	37.80	37.35	48.5	42.77	42.35
Total	100.0	100	97.48	100.0	100	98.06	100.0	100	98.90	100.0	100	98.62	100.0	100.00	98.58	100.0	100.00	97.83
ψ_B	3.3			3.2			3.5			3.3			1.2			1.2		
ψ_B (Fe)	3.0						3.1						1.0					

THEORETICAL REMARKS

There are several structural parameters characterizing some features of the structure of glasses. The most important among them are degree of connectedness of the silica-oxygen network (f_{Si}) for silicate-based and relative fraction of four-coordinated boron (ψ_B) for borate and borosilicate glasses [12]:

$$\psi_B = \{(Na_2O+K_2O+BaO)+[0.7(CaO+SrO)+[0.3(MgO+ZnO+PbO)]-Al_2O_3\}/B_2O_3 \qquad (3)$$

Formally, boron is three-coordinated if $0 \leq \psi_B \leq 1/3$ and forms boron-oxygen triangles. At $1/3 < \psi_B < 1$ both three- and four-coordinated boron atoms co-exist and are present in complex borate groups. At $\psi_B \geq 1$ all the boron is four-coordinated and forms boron-oxygen tetrahedra associated with alkali and, in less extent, alkali earth cations as, for example, $Me^+[BO_{4/2}]$ units. Actually, significant excess of alkali or/and alkali earth oxides as oxygen donors to form BO_4 tetrahedra and convert all the boron into four-coordinated state is needed. This process depends also on silica content in glass. At relatively high silica content (60-80 wt.%) the ψ_B value is estimated to be 1.5-2. At lower silica contents (44-60 wt.%) this value should be much higher. We have demonstrated using IR and electron paramagnetic resonance (EPR) spectroscopy that in borosilicate glasses for high-sodium intermediate level waste immobilization containing 40-50 wt.% SiO_2 minor fraction of trigonally coordinated boron is present even at $\psi_B \cong 4\div5$ [13].

Because Al_2O_3 is stronger acceptor of oxygen than B_2O_3, oxygen introduced with alkali and alkali earth oxides is in the first instance spent for transformation of Al into four-coordinated state. Scheme of coordination transformations for aluminoborosilicate glasses is shown in Table II [6].

Table II. Coordination of boron and aluminum in glasses at various ψ_B values [12].

φ_B	Coordination			
$\psi_B>1$	$[AlO_4]$	$[BO_4]$	-	-
$1/3<\psi_B<1$	$[AlO_4]$	$[BO_4]$	$[BO_3]$	-
$0<\psi_B<1/3$	$[AlO_4]$	-	$[BO_3]$	-
$\psi_B<0$	$[AlO_4]$	-	$[BO_3]$	$[AlO_6]$

As seen from Table III, aluminum offers negative effect on transformation of trigonally coordinated boron into tetragonally coordinated one. Stability of coordination state depends on a value of cationic to anionic radii ratio (r_c/r_a). For tetrahedral oxygen coordination this ratio ranges between 0.22 and 0.41 [14] (radius of O^{2-} anion is assumed to be 1.36 Å). Deviation from average value of the r_c/r_O^{2-} ratio expressed as $|\Delta| = [r_c/r_O^{2-}]_{av} - [r_c/r_O^{2-}]_{calc}$ may be considered as a measure of stability of tetrahedral coordination for the given cation. The values calculated from two different reference data are given in Table III. Due to higher stability of $[AlO_4]$ tetrahedra as compared to $[BO_4]$ tetrahedra oxygen delivered by alkali oxides is firstly spent for formation of AlO_4 tetrahedra and at relatively high Al_2O_3 concentrations major boron remains three-coordinated. Nevertheless this does not offer negative effect on chemical durability of glasses, because aluminosilicate glass network built from SiO_4 and AlO_4 tetrahedra with associated alkali ions is leach resistant [16,17].

Table III. Cationic radii, cationic to oxygen anion radii ratios and their deviations from average value (0.315 Å) for tetrahedrally coordinated ions.

Cation	B^{3+}		Si^{4+}		Al^{3+}		Fe^{3+}	
Refs	[14]	[15]	[14]	[15]	[14]	[15]	[14]	[15]
r_c, Å	0.20	0.11	0.39	0.26	0.57	0.39	0.67	0.49
r_c/r_O^{2-}	0.15	0.08	0.29	0.19	0.42	0.29	0.49	0.36

$\lvert\Delta\rvert$	0.165	0.235	0.025	0.125	0.105	0.025	0.175	0.045

Effect of iron oxides on boron coordination in borosilicate glasses is more complicated. Fe^{3+} ions being network-formers act similarly to Al^{3+} ions forming FeO_4 tetrahedra and suppressing $B^{III} \rightarrow B^{IV}$ transformation. However, since stability of $[Fe^{3+}O_4]$ tetrahedron is lower then that of $[AlO_4]$, the effect of Fe_2O_3 on $B^{III} \rightarrow B^{IV}$ transformation is weaker. Molar concentration of Fe_2O_3 should be subtracted like Al_2O_3 in eq. (2) but with a coefficient less than 1. Taking into account that energy of Fe^{3+}—O bond is lower than that of Al—O bond by ~3 times, this coefficient may be suggested to be ~3 as well. Therefore, in the numerator of the eq. (2) we have to subtract additionally $\sim 0.3 \times [Fe_2O_3]$. Thus in the presence of Fe_2O_3 the ψ_B values for the glasses studied are somewhat lower (Table I). At high concentrations in glasses Fe^{3+} ions may become network-modifiers with higher coordination number (CN=6) or form separate crystalline phase – hematite (Fe_2O_3) or spinel, especially in the presence of Fe^{2+} ions or different transition metal ions (Mn^{2+}, Ni^{2+}, Co^{2+}, Cu^{2+}, Zn^{2+}) as well as Mg^{2+} and Al^{3+} ions. Fe^{2+} ions, if present, are network-modifiers, but often form spinel type phase.

RESULTS AND DISCUSSION

Chemical Composition and XRD Patterns

Target and actual chemical compositions of glasses are similar (Table I). Trace of Fe_2O_3 is present in glasses which should not contain it due to impurity in chemicals.

All the glasses except glass B1 are X-ray amorphous (Figure 1). XRD pattern of glass B1 contains reflections due to carnegieite. Positions of reflections are a little different from tabular values due to isomorphic substitutions with various ions in its crystal lattice.

Glass B1 has complex texture and contains crystalline phase carnegieite (Figures 1, 3-5). Carnegieite is a high temperature variety of nepheline. Features of chemical composition of this phase will be discussed later.

Optical and SEM/EDS Data

Glasses A1 and A2 have uniform texture and does not contain any imhomogeneities (Figure 2, *1*-*3* and Figure 3, *1*-*3*). Tables IV and V demonstrate homogeneous distribution of major elements over the bulk of the glass. Optical microscopy study shows that thin section of the glass A1 is predominantly composed of transparent glass. Minor brown-colored glass also occurs. Local aggregations of fine gas bubbles are observed (Figure 2, *4*). Glass A2 is nearly optically uniform but is characterized by cracking (Figure 3, *4*).

As follows from optical and SEM data areas of devitrified glass B1 have symmetric zoned structure (Figures 4 and 5). The rim is uniform and composed of carnegieite structure crystalline phase. Optical microscopy data in transparent cross-section at single Nichol shows that unlike the glass having light-brown color carnegieite is colorless and has double reflection in the crossed Nichols. It has also contraction cracks being characteristic of devitrification of glass. This zone with a thickness of 50-70 μm is darker than the glass in backscattered electrons (Figure 5).

Chemical composition of carnegieite is similar to that of glass but does not contain boron (Tables VI and VII). It is calculated well to formula with four oxygen ions (Table VII).

The next symmetric zone (Figures 3-5) has a thickness of about 25 μm and clear borders and brown color at single Nichol. It is isotropic in crossed Nichols (Figure 3) and has light-gray color and uniform texture in backscattered electrons (Figure 5). It is different in chemical composition from carnegieite (Table VIII). At similar sodia and silica contents it is depleted with alumina and enriched with ferrous oxides. This phase is also satisfactory recalculated to a formula with four oxygen ions and may be referred to ferrous carnegieite.

The core is dark-brown and nearly opaque in transparent cross-sections (Figure 3). This zone is composed of two phases. Phase-1 having light-gray color on SEM images is aggregate of micro-scales (Figure 5). Its chemical composition was determined by scanning over area and is given in Table IX. Chemical composition and structure of this phase is similar to the previous ones. Phase-2 of the core is represented by dendrite crystals of spinel up to 10 μm in size (Figures 5 and 6). This phase is not appeared on XRD patterns due to low content in glass.

Glasses B2, D1 and D2 are homogeneous (Figures 7-9). Chemical compositions determined by EDS scanning over areas shown on Figure 9 (right) are given in Tables VIII-X.

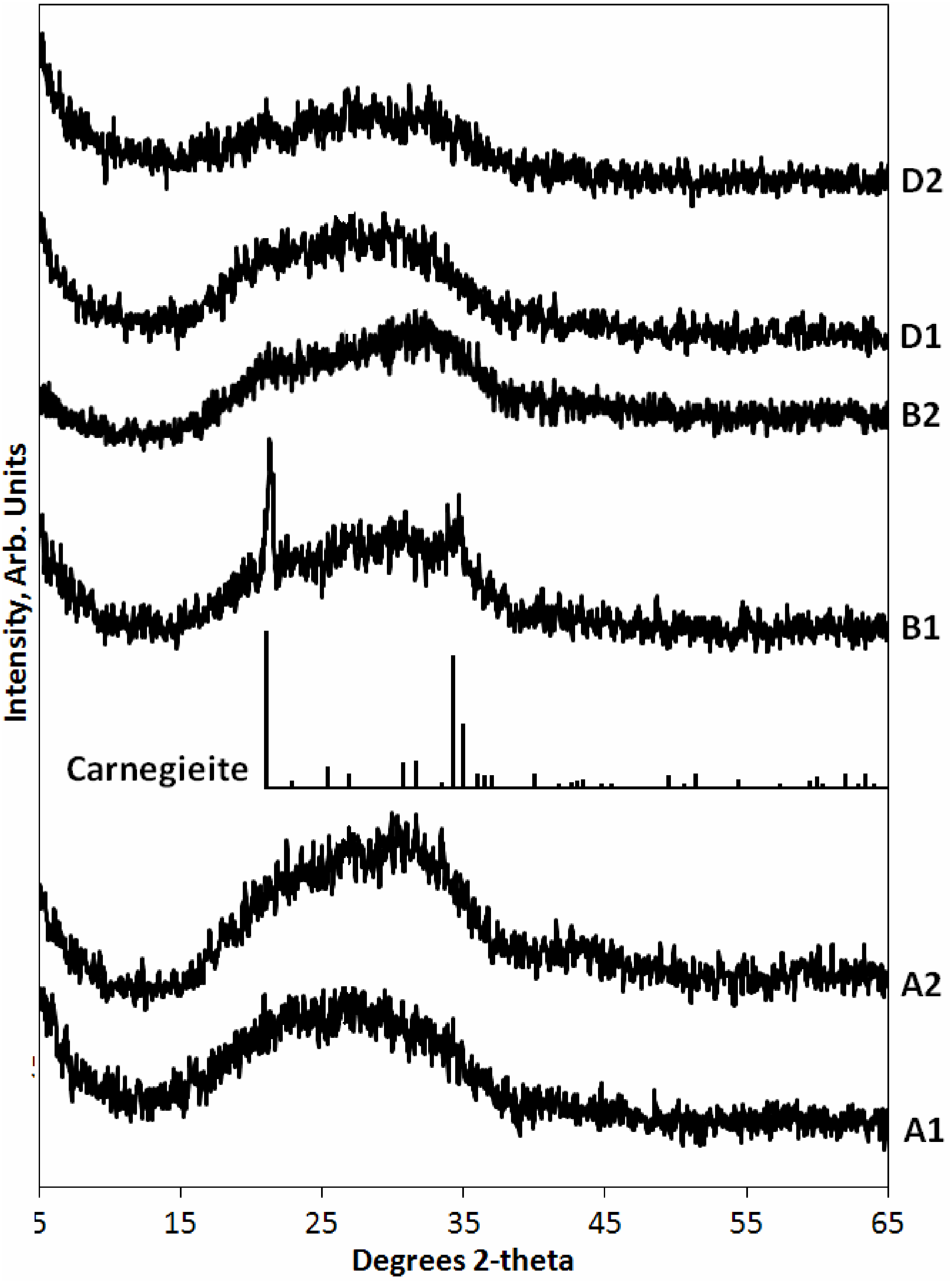

Figure 1. XRD Patterns of Glass Samples.

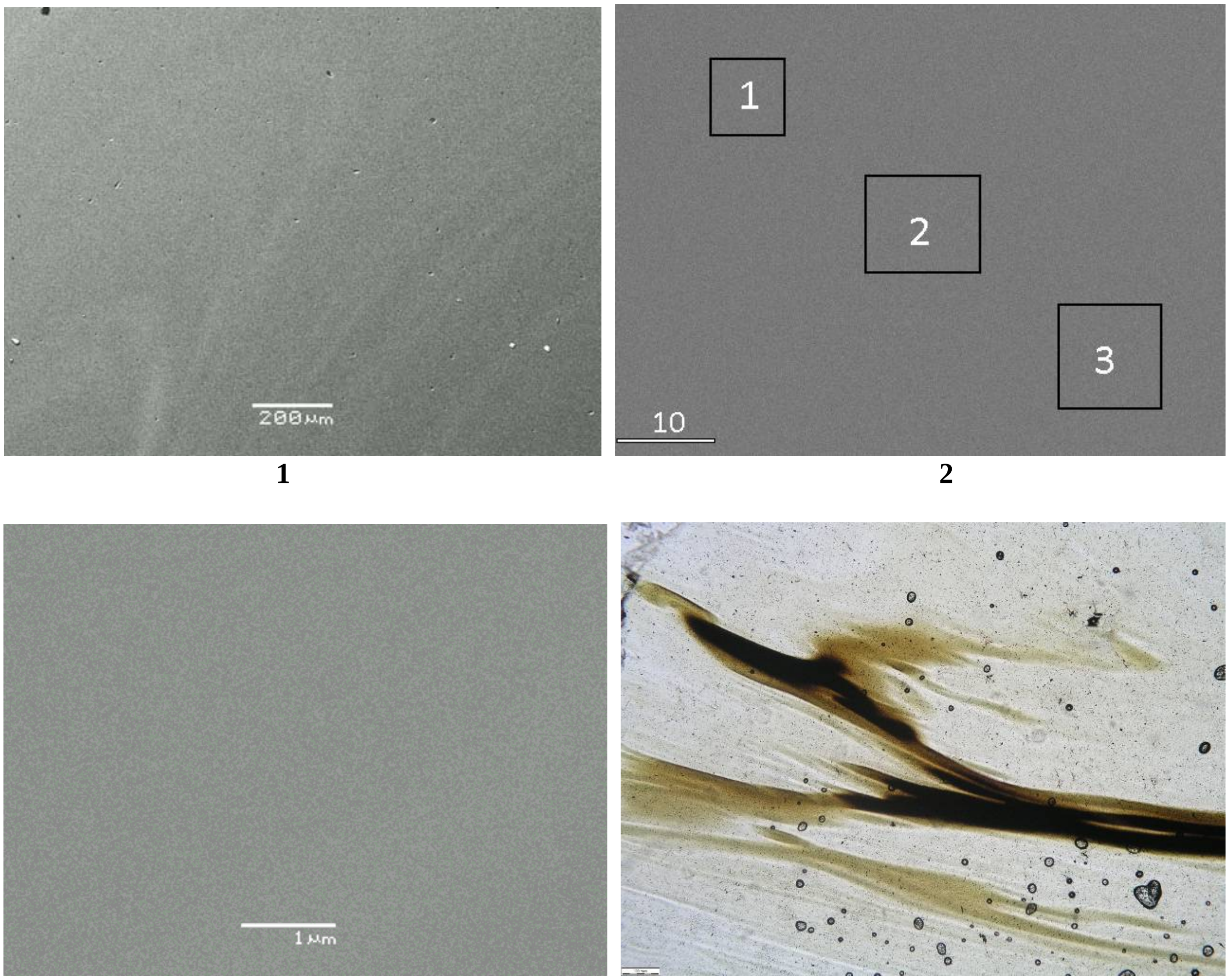

1 2

3 4

Figure 2. SEM Image in Backscattered Electrons (1-3) and Optical Microscopy Image (4) of Sample A1 at Various Magnifications.

Scale bar on he middle photo is given in microns.

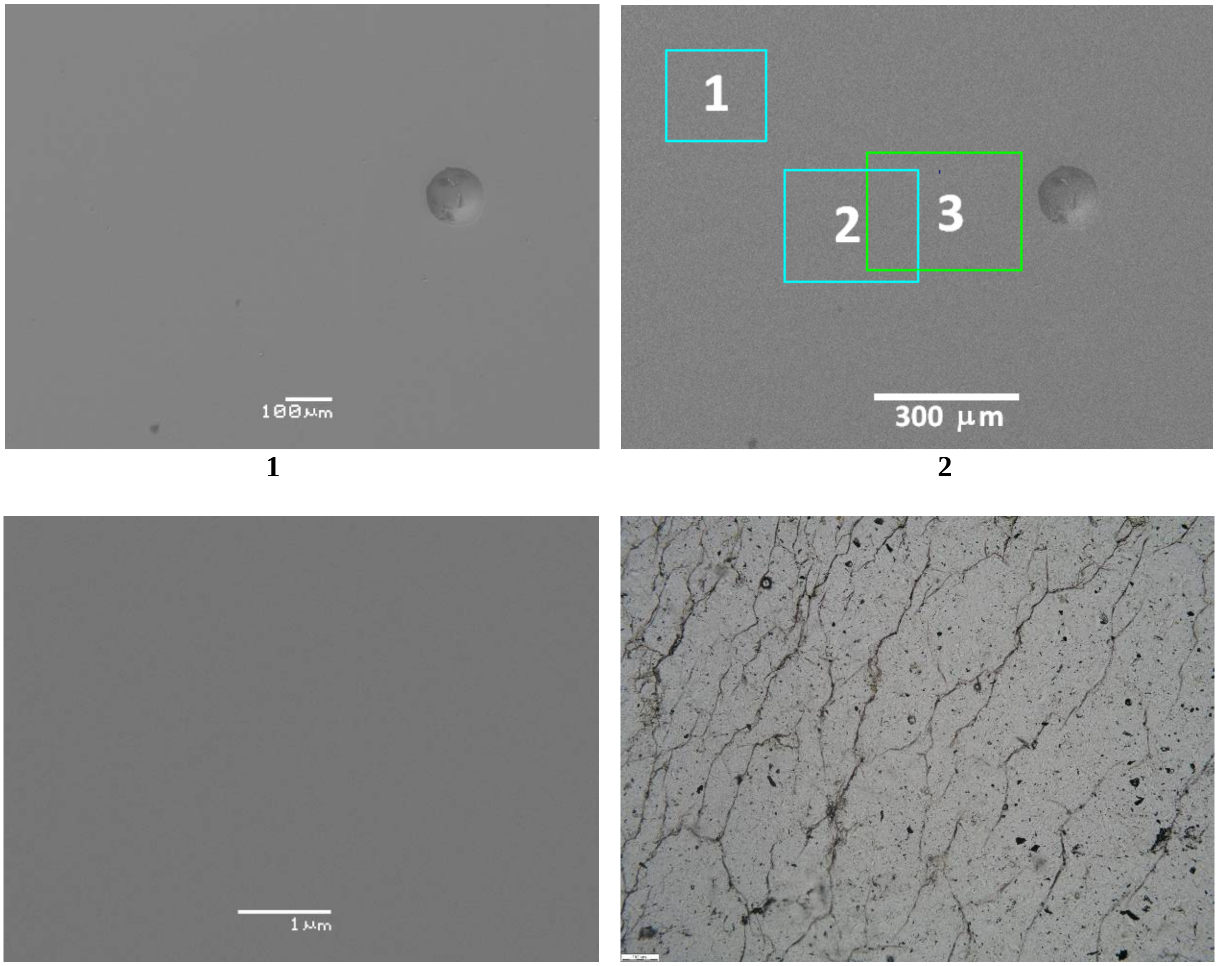

1 2

3 4

Figure 3. SEM Image in Backscattered Electrons (1-3) and Optical Miscoscopy Image (4) of Sample A2 at Various Magnifications.

Scale bars are given in microns.

Table IV. Chemical Composition of Sample A1 by SEM/EDS Data.

Oxides	Target		Actual wt.%	Scanned Areas on Fig. 2			Average
	mol.%	wt.%		1	2	3	
Na_2O	25.0	22.27	21.45	20.74	20.71	20.51	20.65
Al_2O_3	8.5	12.46	12.50	14.11	13.8	13.98	13.96
SiO_2	56.5	48.80	48.30	48.45	48.95	48.37	48.59
Fe_2O_3	5.0	11.48	10.35	8.66	8.40	8.26	8.44
B_2O_3	5.0	5.00	4.88	ND	ND	ND	ND
Sum	100.0	100.00	97.48	91.96	91.86	91.12	91.64

ND – not determined

Table V. Chemical Composition of Sample A2 by SEM/EDS Data.

Oxides	Target,		Actual, wt.%	Scanned areas on Fig. 3			Average, wt.%
	mol.%	wt.%		1	2	3	
Na_2O	26.5	25.31	23.80	22.9	22.08	22.00	22.33
Al_2O_3	9.0	14.14	14.30	15.07	15.54	15.02	15.21
Fe_2O_3	-	-	0.08	0.08	0.04	0.09	0.07
SiO_2	59.0	54.64	54.30	55.74	53.84	55.39	54.99
B_2O_3	5.5	5.90	5.58	ND	ND	ND	ND
Sum	100	100	98.06	93.79	91.50	92.50	92.60

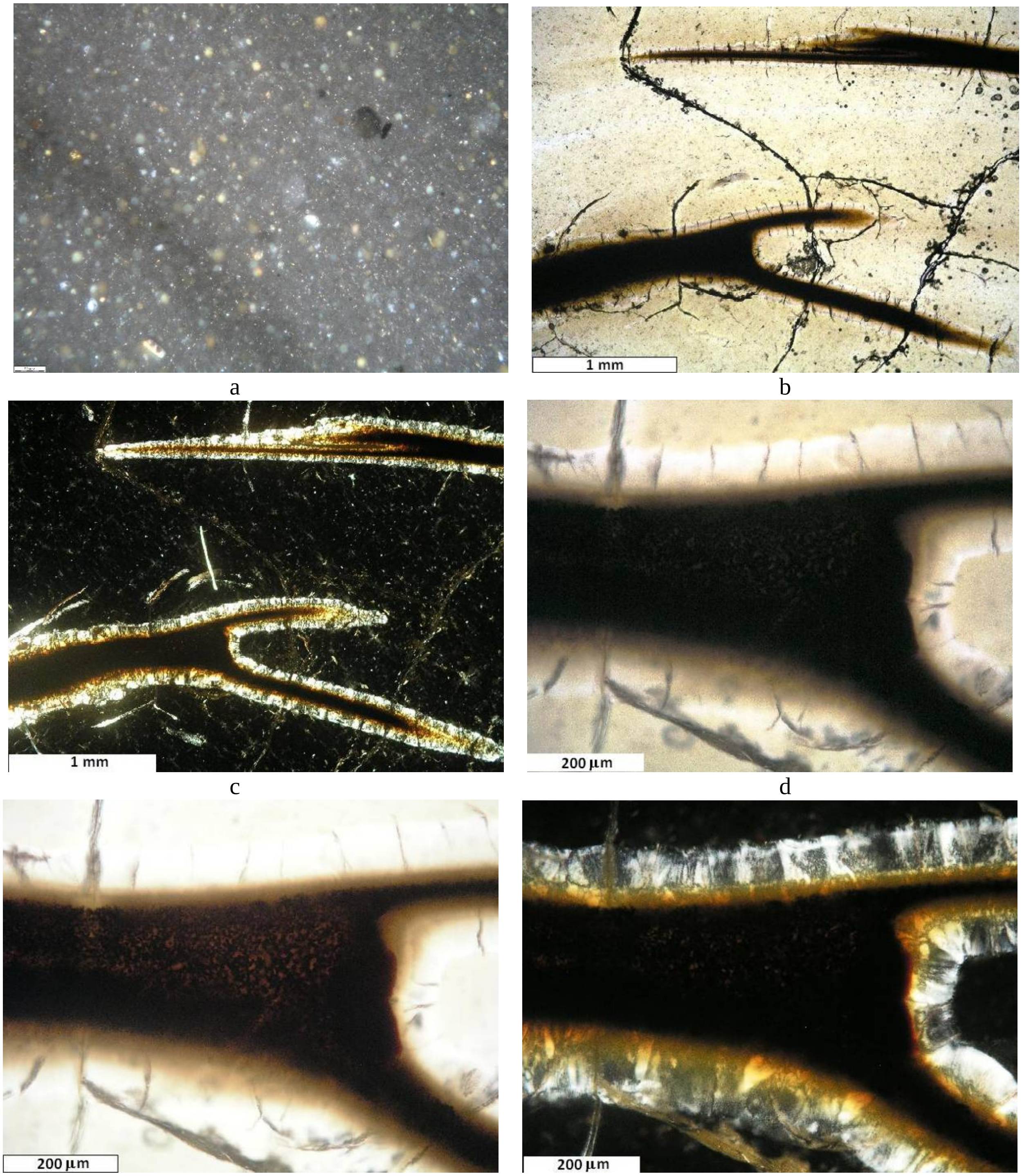

a b c d e f

Figure 4. Optical Microscopy Images in Transparent Cross-Sections of Sample B1 at One Nichol (a) and in Parallel (b, c, e) and Crossed Nichols (d, f).

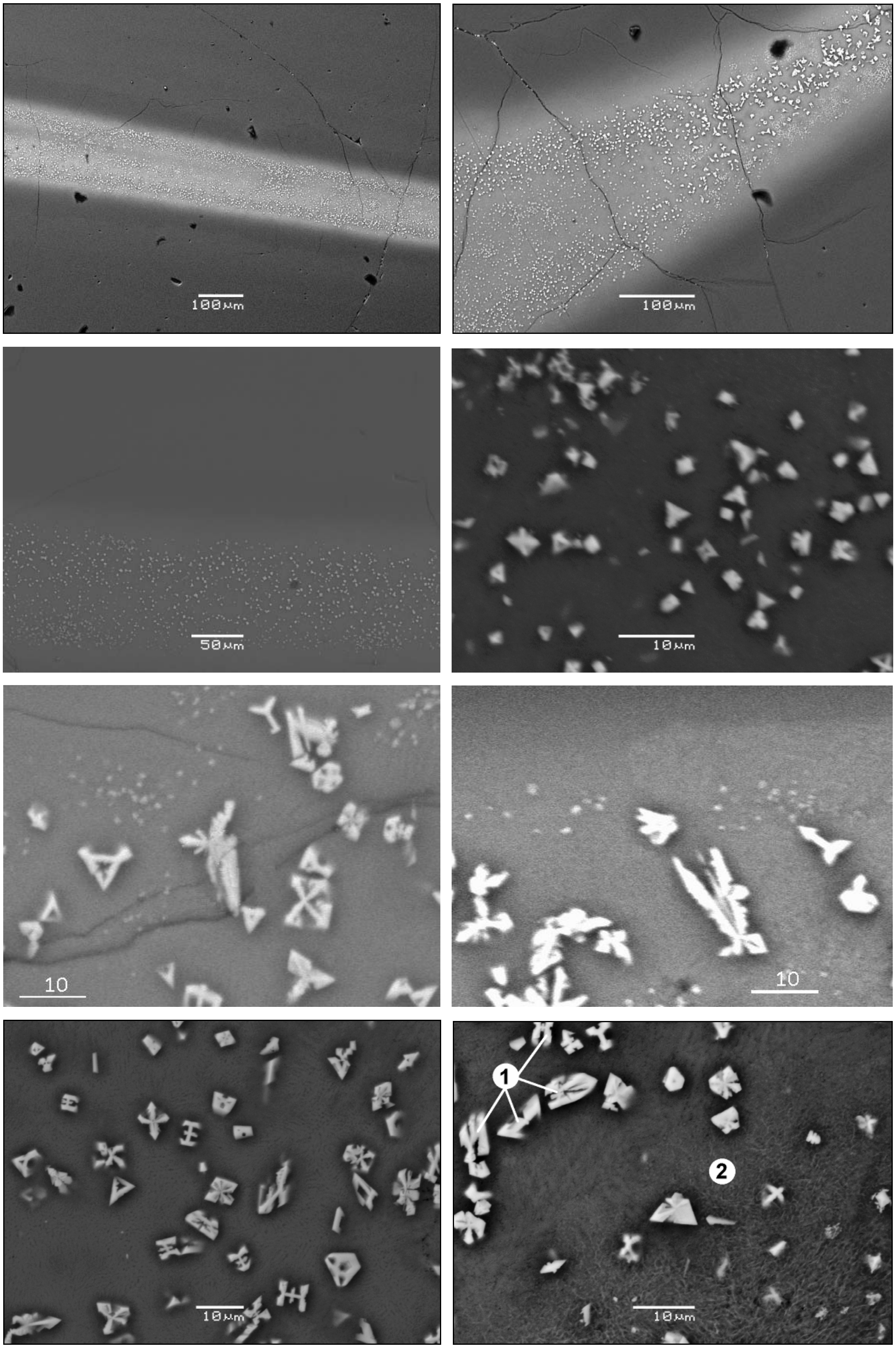

Figure 5. SEM Images in Backscattered Electrons of Sample B1 at Various Magnifications.

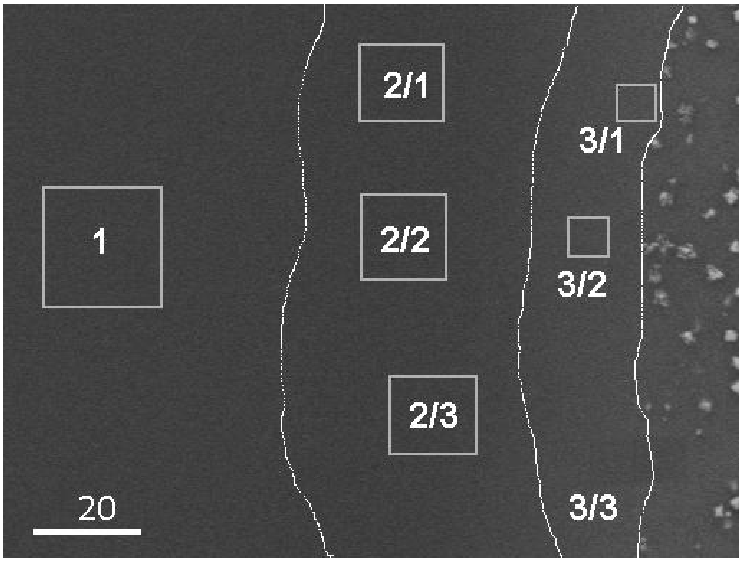

Figure 6. Zones in Bulk of Sample B1. Scale Bar is in Microns.

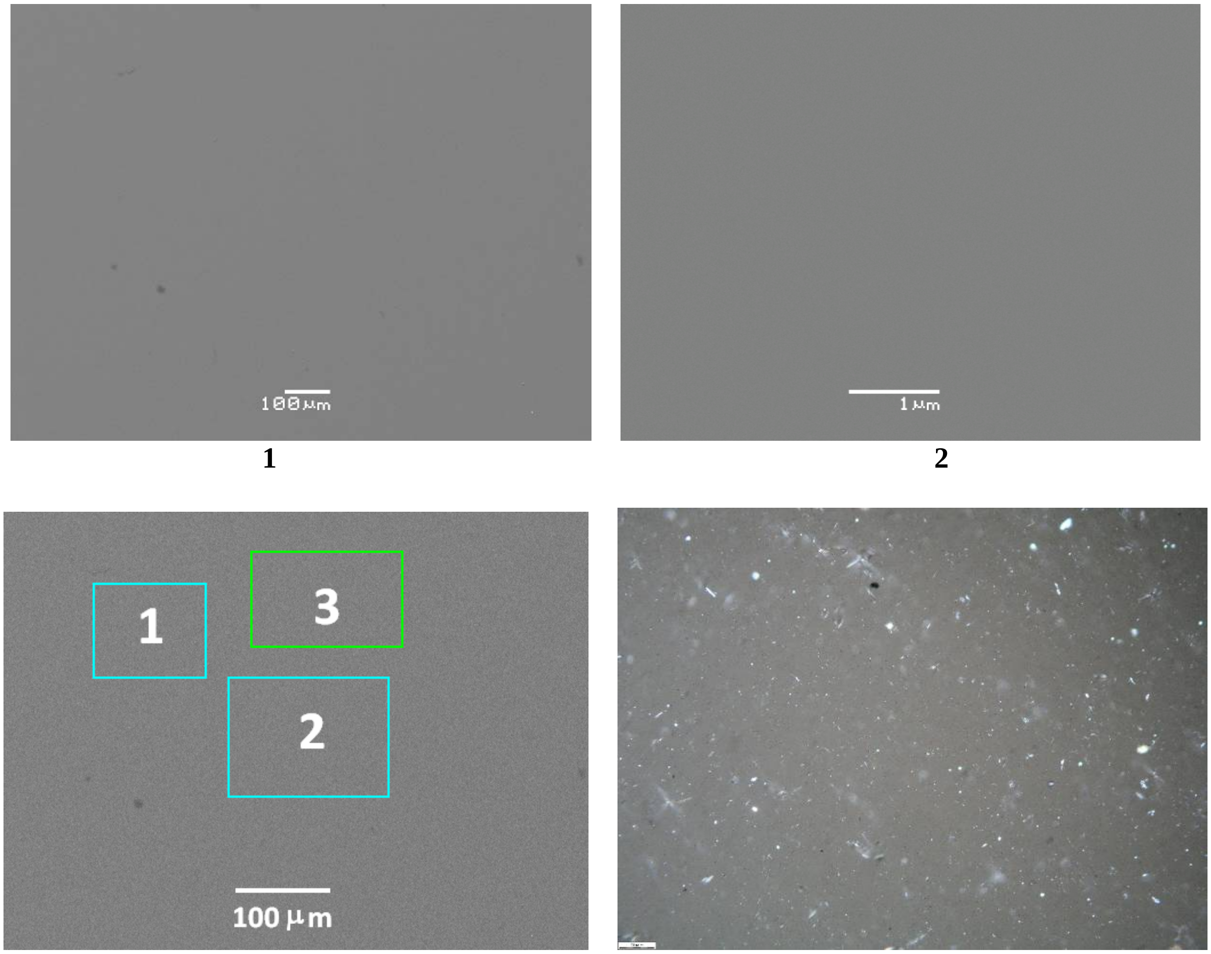

1 2

3 4

Figure 7. SEM Images in Backscattered Electrons of Sample B2 at Various Magnifications (1-3) and Optical Microscopy Image (4).

Table VI. Chemical Composition of Various Zones in Sample B1 by SEM/EDS Data.

Oxides	Target		Actual	Glass	Carnegieite				Carnegieite + Spinel			
	mol.%	wt.%	wt.%	1	2/1	2/2	2/3	Aver.	3/1	3/2	3/3	Aver.
Na_2O	29.5	25.18	24.05	23.48	22.16	22.07	21.55	21.93	19.72	18.95	19.94	19.54
Al_2O_3	15.0	21.06	21.00	23.34	24.12	23.74	23.65	23.84	16.75	19.73	17.41	17.96
SiO_2	46.0	38.07	36.00	37.41	37.29	37.12	37.02	37.14	29.89	32.3	29.87	30.69
Fe_2O_3	5.3	11.66	11.05	10.77	11.01	11.45	11.96	11.47	24.91	19.96	24.2	23.02
B_2O_3	4.2	4.03	3.80	ND	ND	ND	ND	ND	ND	ND	ND	ND
Sum	100.0	100.00	95.90	95.00	94.58	94.38	94.18	94.38	91.27	90.94	91.42	91.21

Table VII. Chemical Composition of Various Zones in Sample B2 by SEM/EDS Data.

Oxides	Target,		Actual, wt.%	Scanned areas on Fig. 7, wt.%			Average, wt.%
	mol.%	wt.%		1	2	3	
Na_2O	31.0	28.34	26.80	25.52	24.34	24.86	24.91
Al_2O_3	16.0	24.06	24.05	28.19	26.5	26.78	27.16
Fe_2O_3	-	-	0.12	0.13	0.08	0.09	0.10
SiO_2	48.5	42.98	43.30	43.56	41.3	41.02	41.96
B_2O_3	4.5	4.62	4.35	ND	ND	ND	ND
Sum	100.0	100.00	98.62	97.40	92.22	92.75	94.13

Table VIII. Chemical Compositions and Formulae of the "Phases" in Sample B1.

Oxides	Target, mol.%	Target, wt.%	Actual, wt.%	Glass	"Phase 1"*	"Phase 2"**
Na_2O	29.5	25.18	24.05	23.48	21.93	19.54
Al_2O_3	15.0	21.06	21.00	23.34	23.84	17.96
SiO_2	46.0	38.07	36.00	37.41	37.14	30.69
Fe_2O_3	5.3	11.66	11.05	10.77	11.00	23.02
B_2O_3	4.2	4.03	3.80	Не опр.	Не опр.	Не опр.
Sum	100.0	100.00	95.90	95.00	93.91	91.21
Ions				Formula Units		
Na^+				1.21	1.13	1.10
Al^{3+}				0.73	0.75	0.61
Si^{4+}				0.99	0.99	0.89
Fe^{3+}				0.21	0.22	0.50
Total				3.14	3.09	3.10
O^{2-}				4.00	4.00	4.00

* Phase 1: $Na_{1.13}Al_{0.75}Fe_{0.22}Si_{0.99}O_4$ – nepheline/carnegieite;
** Phase 2: nepheline/carnegieite + spinel.

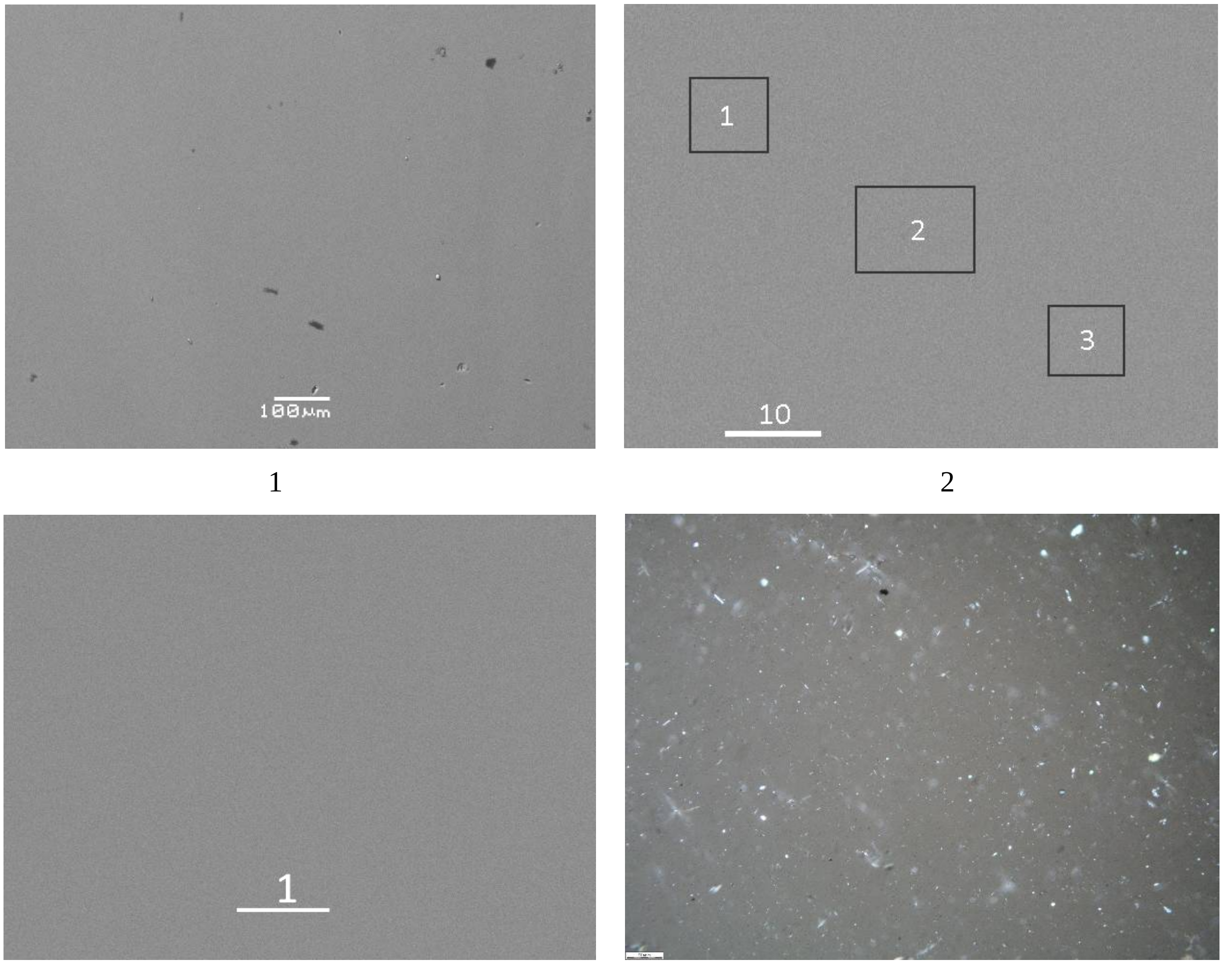

1 2

3 4

Figure 8. SEM Images in Backscattered Electrons (1-3) and Optical Miscroscopy Image (4) of Sample D1.

Scale Bars are given in Microns.

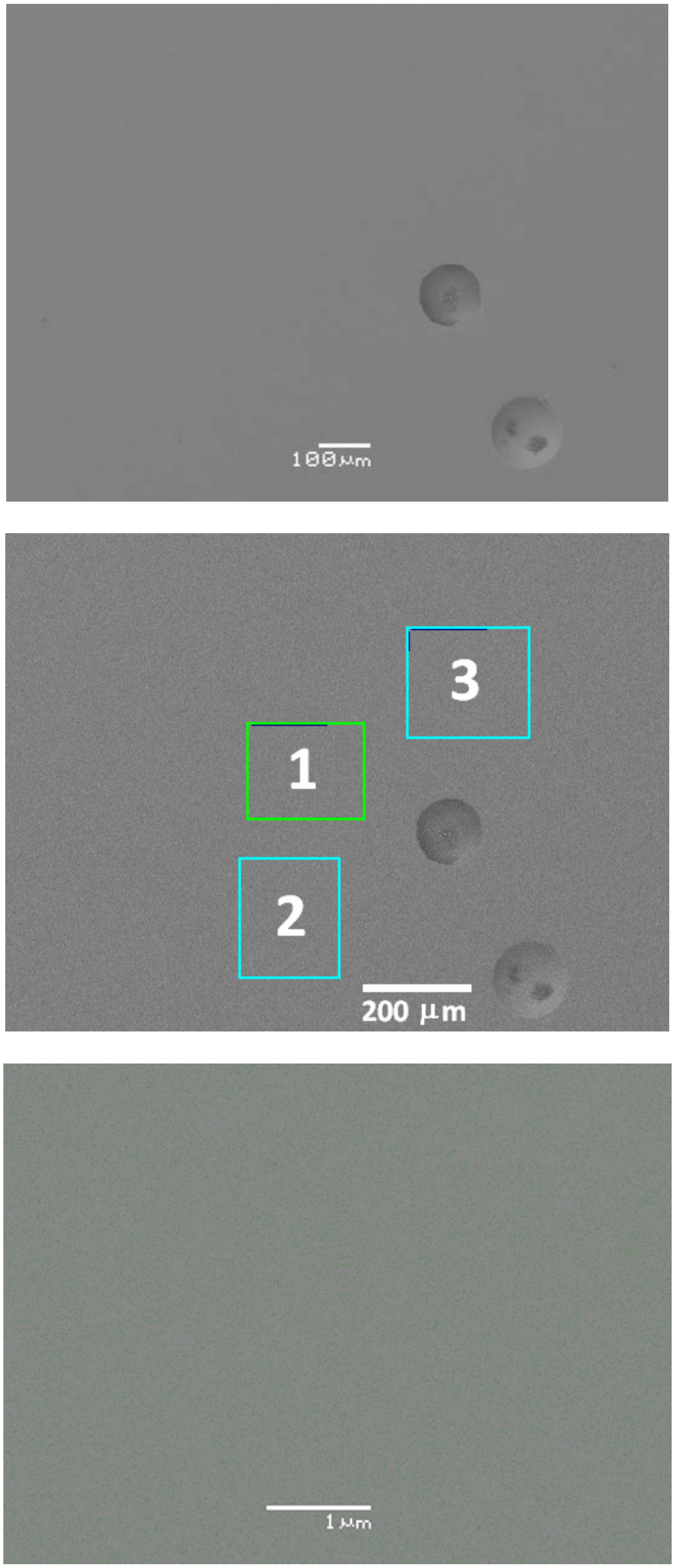

Figure 9. SEM Images in Backscattered Electrons of Sample D2.

Table IX. Chemical Compositions of Sample D1 by SEM/EDS Data.

Oxides	Target		Actual	Scanned Areas on Fig. 8			Average
	mol.%	wt.%	wt.%	1	2	3	
Na_2O	8.0	6.38	20.25	18.67	19.24	18.85	18.92
Al_2O_3	26.4	34.62	20.60	22.08	21.98	22.00	22.02
SiO_2	35.6	27.51	37.35	36.92	36.11	36.56	36.53
Fe_2O_3	4.0	8.21	12.55	11.53	11.22	10.94	11.23
B_2O_3	26.0	23.28	7.74	ND	ND	ND	ND
Sum	100.0	100.00	98.49	89.2	88.55	88.35	88.70

Table X. Chemical Compositions of Sample D2 by SEM/EDS Data.

Oxides	Target		Actual	Scanned Areas on Fig. 9			Average
	mol.%	wt.%	wt.%	1	2	3	
Na_2O	26.5	24.10	22.95	20.88	19.59	20.52	20.33
Al_2O_3	16.0	23.94	23.50	25.93	24.93	25.93	25.6
SiO_2	48.5	42.77	42.35	42.45	40.68	42.95	42.03
Fe_2O_3	-	-	0.05	0.04	0.06	0.05	0.05
B_2O_3	9.0	9.19	8.98	ND	ND	ND	ND
Sum	100.0	100.00	97.83	89,30	85,26	89,45	88,01

Effect of Etching on the Structure of the Surface of Glasses

The polished surfaces of the samples A1, A2, B1, B2, D1 and D2 were etched with 0.1M HCl for 1 day and studied by SEM/EDS.

Surface of the glasses after etching is corroded (Figures 10-15). Chemical compositions of corroded layer and unaltered bulk may be determined in the strongest corroded areas (Tables XI and XII).

As follows from theoretical consideration, glasses A1, A2, B1 and B2 should not have a tendency to liquid-liquid phase separation because the ψ_B values for their composition significantly exceed 1. Corrosion of these glasses proceeds by conventional mechanism with a damage of their surface layers (Figures 10-13) and formation of a rim enriched with silica and depleted with alkali ions. The strongest corrosion takes place along the fractures on the glass surface (Figure 11).

Nevertheless, drop-type structure was observed after etching of the surface of glass B2 (Figure 12) that suggests occurrence of liquid-liquid phase separation: the structure of the glass B2 consists of areas with higher and lower durability to acid attack and, therefore, different in chemical composition. The diameter of the drops is widely varied and reaches ~100 μm. The drops seems to be higher than the matrix glass, therefore, they have higher chemical durability.

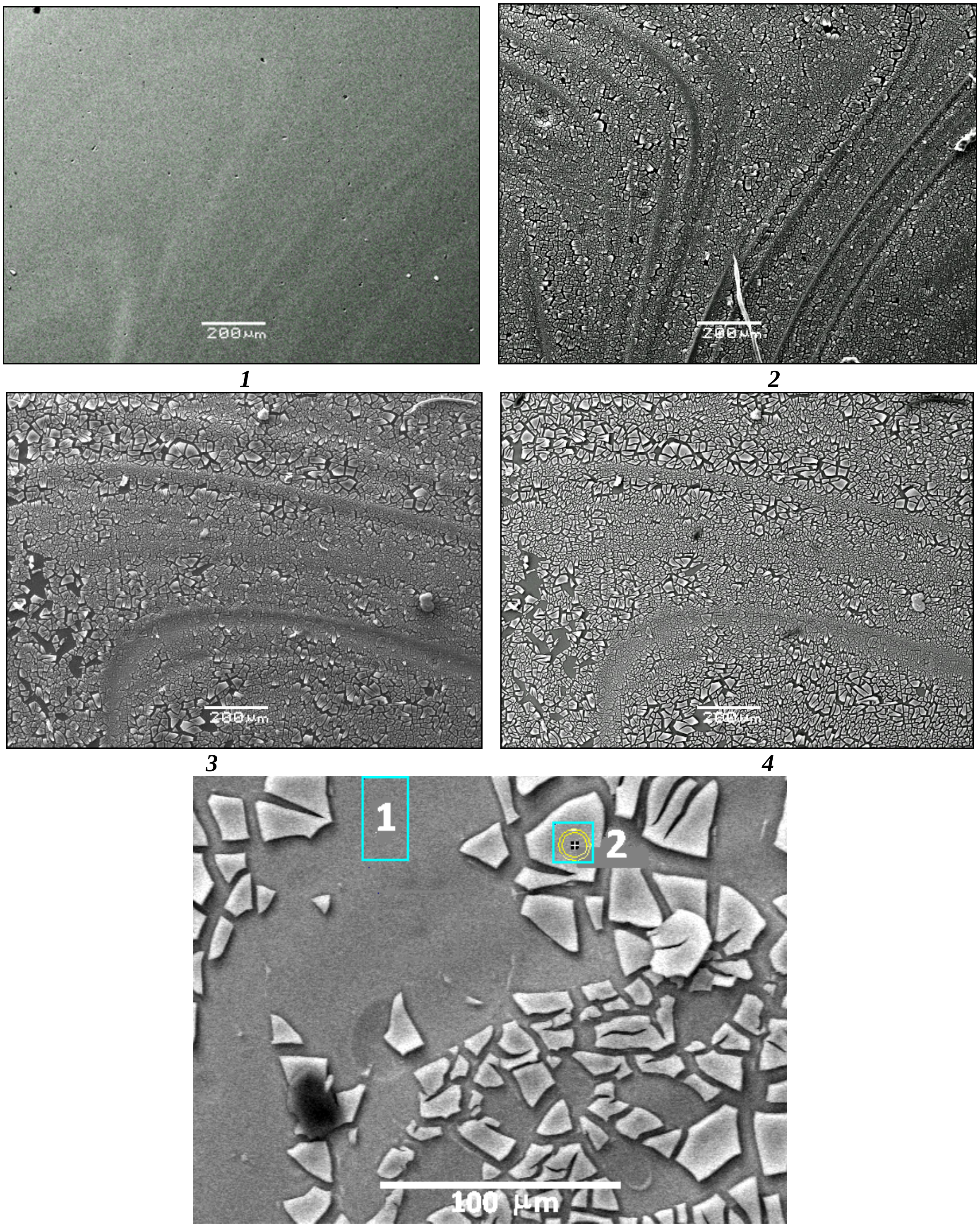

1 *2* *3* *4* *5*

Figure 10. BSE SEM Images of the Surface of the Glass A1 Before (1) and After (2-5) Etching in 0.1 M HCl.

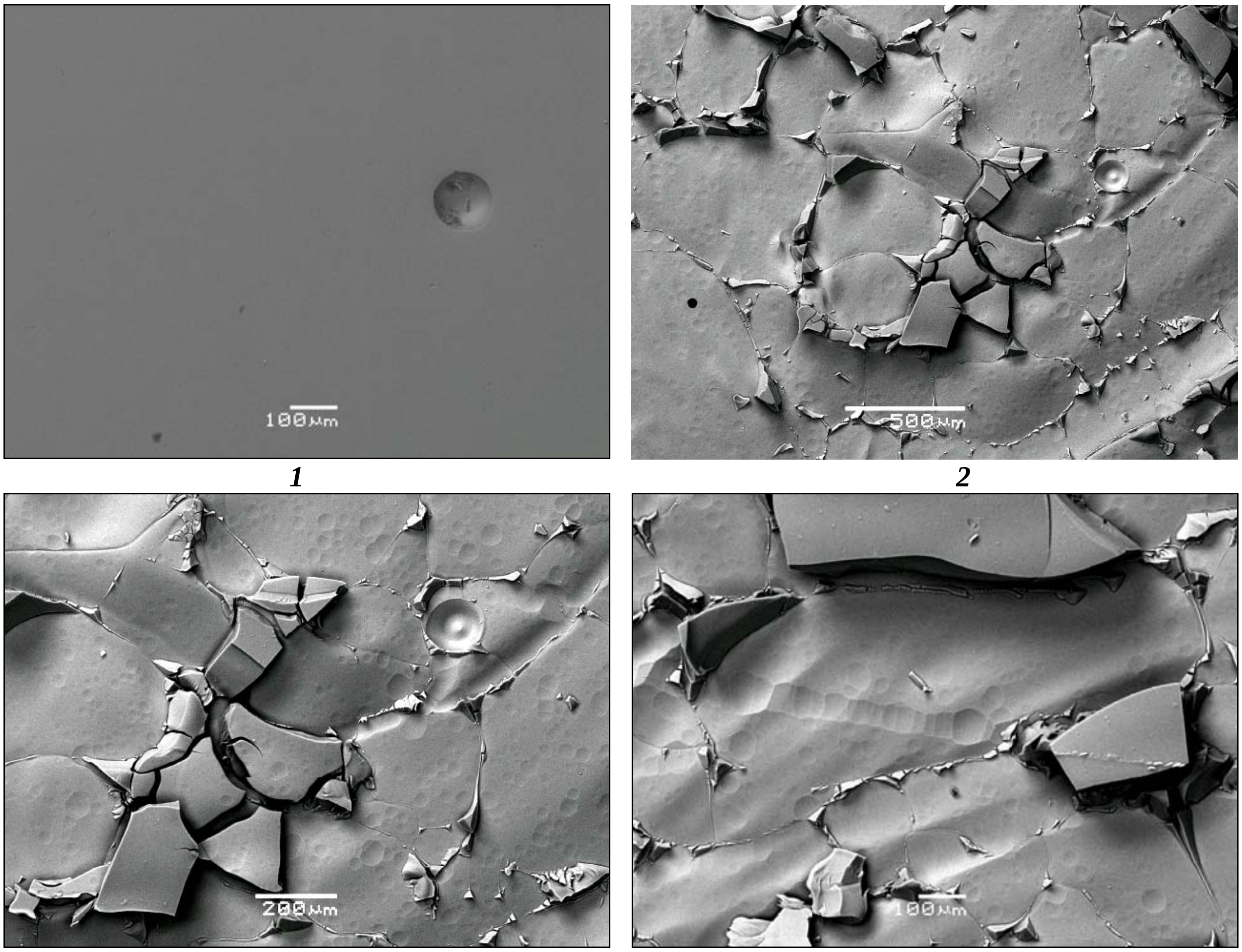

1 *2*

3 *4*

Figure 11. BSE SEM Images of the Surface of the Glass A2 Before (1) and After (2-5) Etching in 0.1 M HCl.

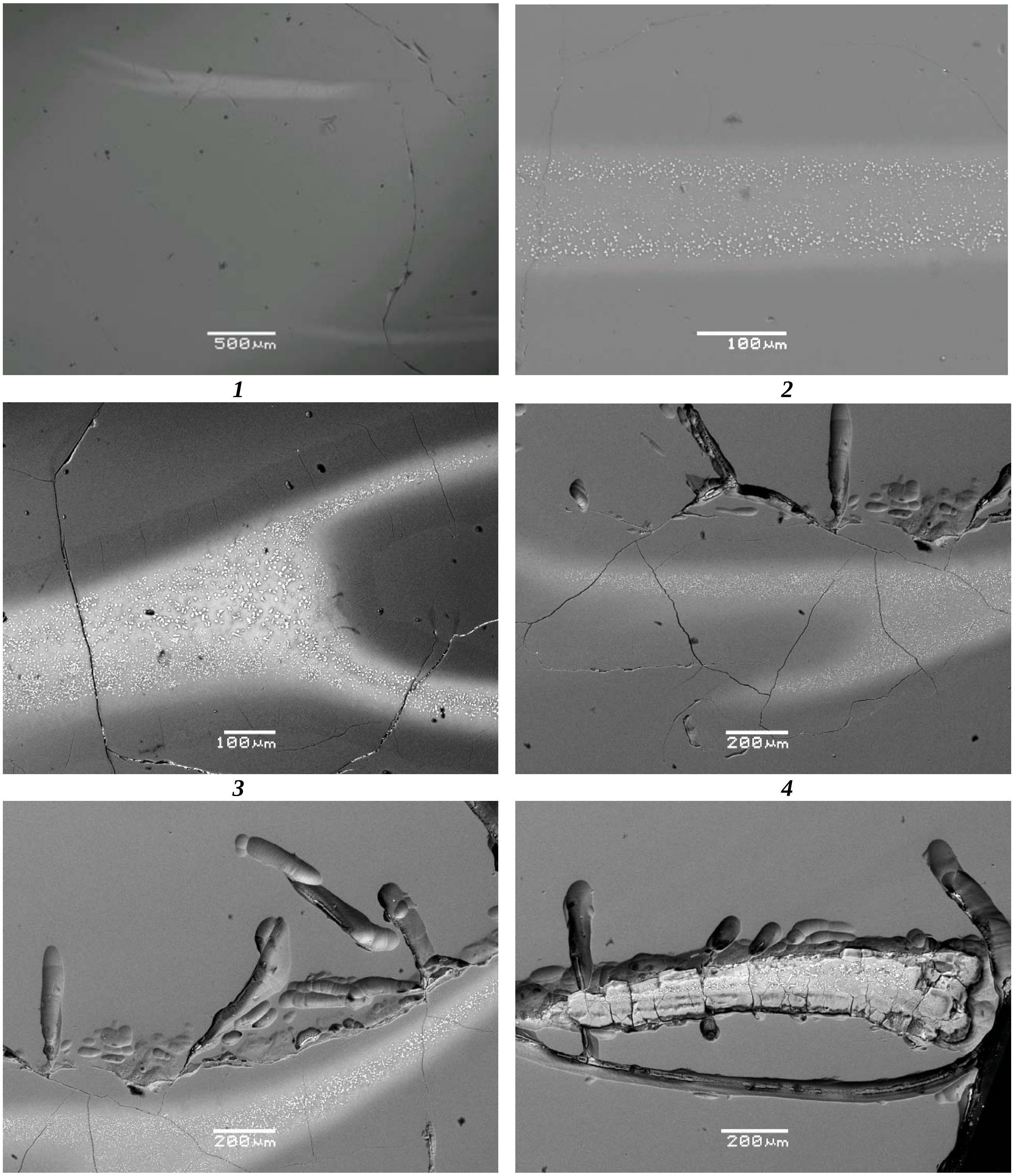

1

2

3

4

5

6

Figure 12. BSE SEM Images of the Surface of the Glass B1 Before (1-3) and After (3-6) Etching in 0.1 M HCl.

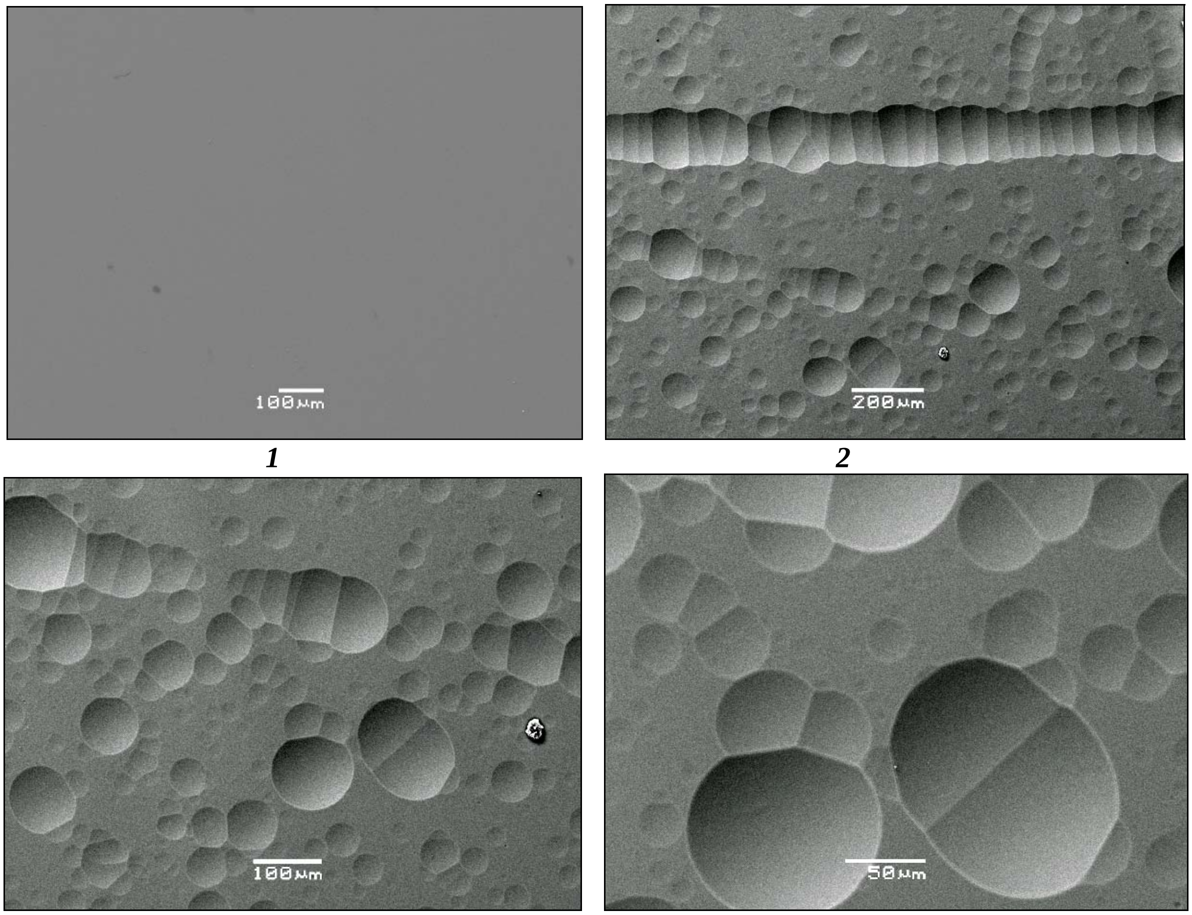

1 *2*

3 *4*

Figure 13. BSE SEM Images of the Surface of the Glass B2 Before (1-3) and After (3-6) Etching in 0.1 M HCl.

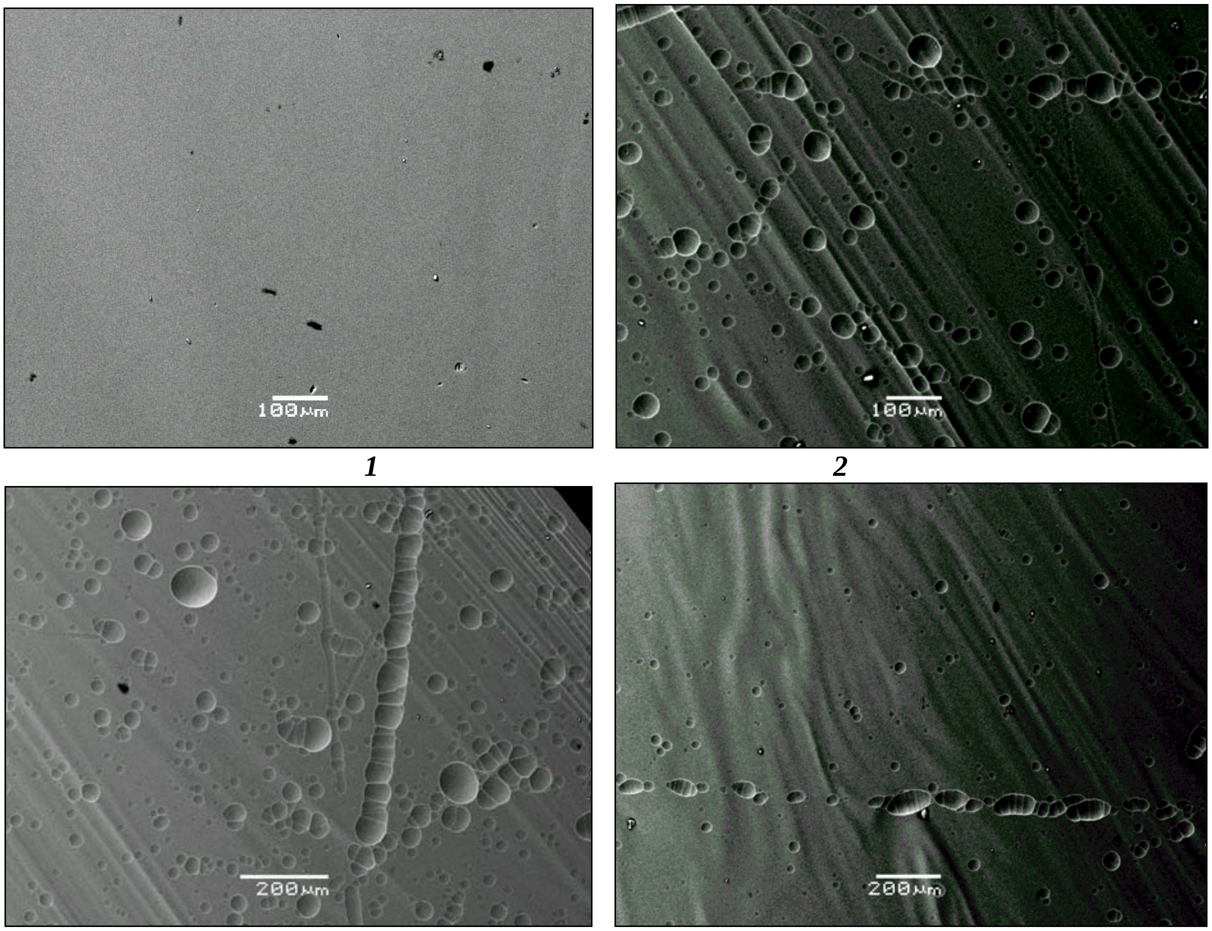

1 *2*

3 *4*

Figure 14. BSE SEM Images of the Surface of the Glass D1 Before (1) and After (2-4) Etching in 0.1 M HCl.

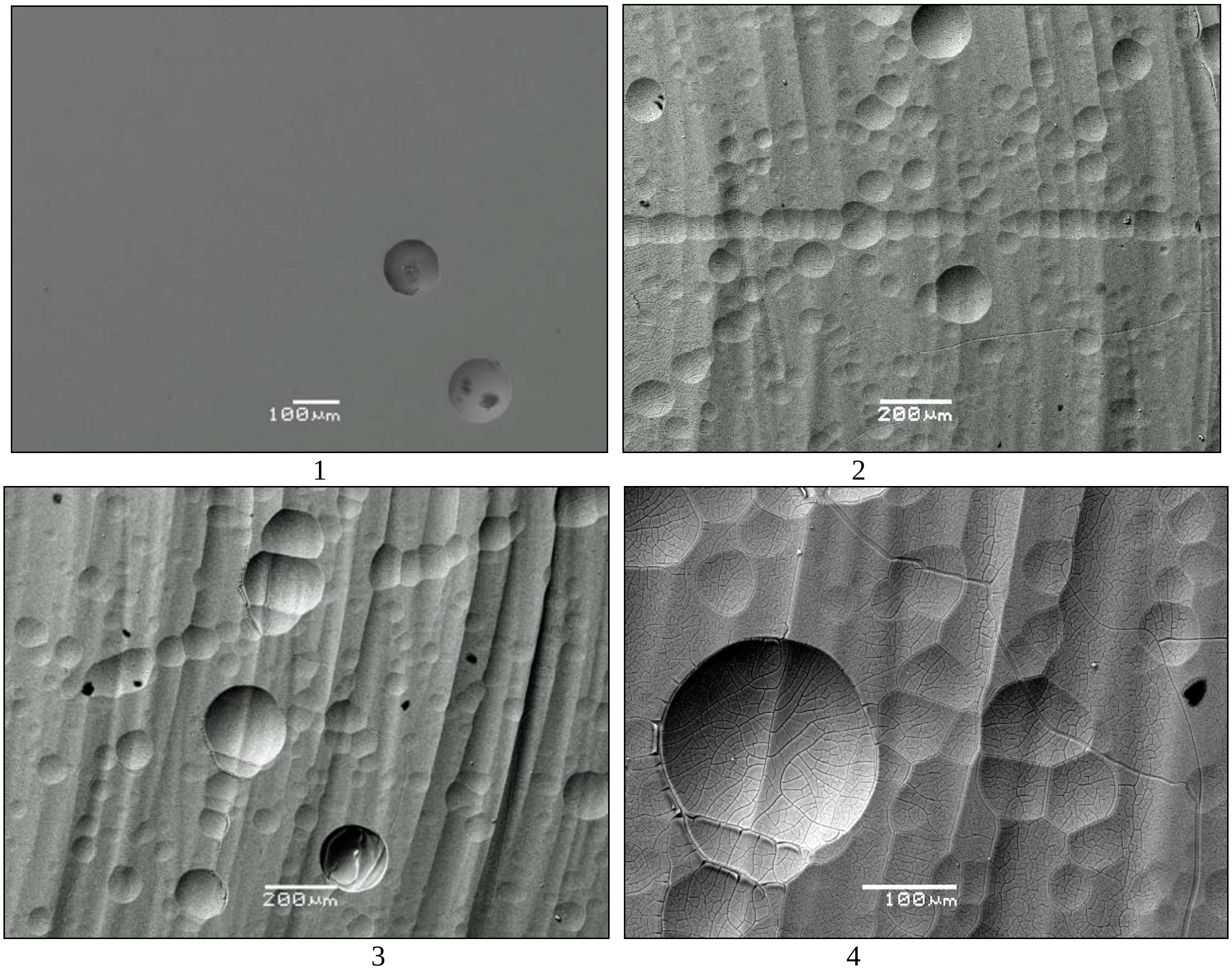

Figure 15. BSE SEM Images of the Surface of the Glass D2 Before (1) and After (2-4) Etching in 0.1 M HCl.

Table XI. Chemical Composition (wt.%) by EDS of Various Areas on the Etched Surfaces of the Glass A1.

Oxides	1 (core)	2a (rim)	2b (rim)	2c (rim)	Average (rim)
Na_2O	19.14	1.57	-	-	0.52
Al_2O_3	14.08	2.88	1.61	2.49	2.33
SiO_2	50.71	40.36	38.65	44.63	41.21
CaO	-	2.83	2.77	3.02	2.87
TiO_2	-	3.40	3.69	3.58	3.56
Fe_2O_3	8.92	18.38	18.51	18.52	18.47
ZnO	-	2.81	3.10	2.81	2.91
Sum	92.85	72.23	68.33	75.05	71.87
B_2O_3*	4.88	ND	ND	ND	ND

* actual content in unaltered glass, ND – not determined.

Table XII. Chemical Composition (wt.%) by EDS of Various Areas on the Etched Surfaces of the Glass D1.

Формула	Actual	1	2	Average
Na_2O	20.25	17.69	17.06	17.50
Al_2O_3	20.60	21.98	19.85	20.92
SiO_2	37.35	36.71	36.93	36.82
Fe_2O_3	12.55	11.87	12.87	12.37
B_2O_3	7.73	ND	ND	ND
Sum	98.48	88.25	70.71	87.61

IR Spectra of Glasses

IR spectra of glasses (Figure 16) consist of the bands due to stretching (3100-3600 cm^{-1}) and bending modes (1600-1800 cm^{-1}) in the molecules of absorbed and structurally bound water, weak bands due to hydrogen bonds in the structure of glasses and numerous bands lower 1600 cm^{-1} due to stretching and bending modes in the units forming anionic motif of the structure of glasses.

IR spectra of all the glasses within the range of 4000-1600 cm^{-1} (Figure 8) consist of the bands due to stretching and bending modes in silicon-oxygen, boron-oxygen, aluminum-oxygen and iron-oxygen (in spectra of glasses A1, B1 and D1 only) structural groups. The wavenumber ranges of 1550-1300 cm^{-1} and ~1260-1270 cm^{-1} are typical of oscillations in the boron-oxygen groups with trigonally coordinated boron (boron-oxygen triangles BO_3) [18]. These bands were attributed as components of twice degenerated asymmetric valence ν_3 O−B−O oscillations (stretching modes). The band with components ~710-730 and 650-670 cm^{-1} may be associated with twice degenerated asymmetric deformation δ (ν_4) O−B−O vibrations (bending modes) [18]. Strong absorption in both IR and Raman spectra within the range of 1150-850 cm^{-1} is caused by asymmetric ν_3 oscillations (stretching modes) in silicon-oxygen units bound to zero (850-900 cm^{-1}), one (~900-950 cm^{-1}), two (~950-1050 cm^{-1}), three (~1050-1100 cm^{-1}) and four (~1100-1150 cm^{-1}) neighboring SiO_4 tetrahedra (Q^0, Q^1, Q^2, Q^3, Q^4, respectively) [19] and, in less extent, BO_4 tetrahedra (1000-1100 cm^{-1}) [18]. In IR spectra of all the glasses the broad band within the range of ~800-1200 cm^{-1} is multicomponent due to superposition of oscillations (stretching modes) in SiO_4 and BO_4 tetrahedra. Stretching modes of Al—O bonds in AlO_4 tetrahedra and Fe—O bonds in FeO_4 tetrahedra are positioned at 700-800 cm^{-1} and 550-650 cm^{-1}, respectively. Bending modes of Si—O—Si bonds in SiO_4 tetrahedra are positioned within the range of 350-550 cm^{-1}.

In the low-wavenumber range 600-30 cm^{-1} (Figure 9) numerous weak bands are present and spectra of all the glasses are similar. Some of the bands may be attributed to Fe—O bonds in FeO_6 octahedra and Na—O bonds.

Glasses A1, A2, B1, and B2 are characterized by similar values of the ψ_B factor (3.0-3.3). As follows from theoretical suggestions major boron on these glasses must be four-coordinated on oxygen. In the structure of these glasses BO_4 tetrahedra are built in the network or chains of SiO_4 tetrahedra forming $[BO_{4/2}]^-Na^+$ units. Therefore, these glasses should have similar structure and their IR and Raman spectra should be similar as well.

IR spectra of glasses A1 and A2 are actually very similar. Two strong bands within the ranges of 850-1200 cm^{-1} and 400-550 cm^{-1} are due to stretching and bending modes of Si—O—Si and Si—O^- bonds. In IR spectra of both glasses the broad band at 850-1200 cm^{-1} consists of a shoulder at ~1160 cm^{-1}, three narrower bands centered at 1085, 1055-1056, and 1002-1006 cm^{-1} and a shoulder at ~890 cm^{-1} due to asymmetric stretching modes in Q^4, Q^3, Q^2, and Q^1 units, including valence oscillations of Si—O—Si(Al) bridging bonds (970-1100 cm^{-1}) and non-bridging Si—O^- bonds (850-950 cm^{-1}). As it is seen from relative intensity of the bands Q^2 units dominate. However, it should be taken into account that oscillations (stretching modes) of Si—O—B bridges linking SiO_4 and BO_4 tetrahedra are also positioned at 950-1000 cm^1 and may make a contribution to this band, although due to low content of B_2O_3 in glasses this contribution should be minor. There is also a weak absorption within the range of 1300-1550 cm^{-1}, 1250-1300

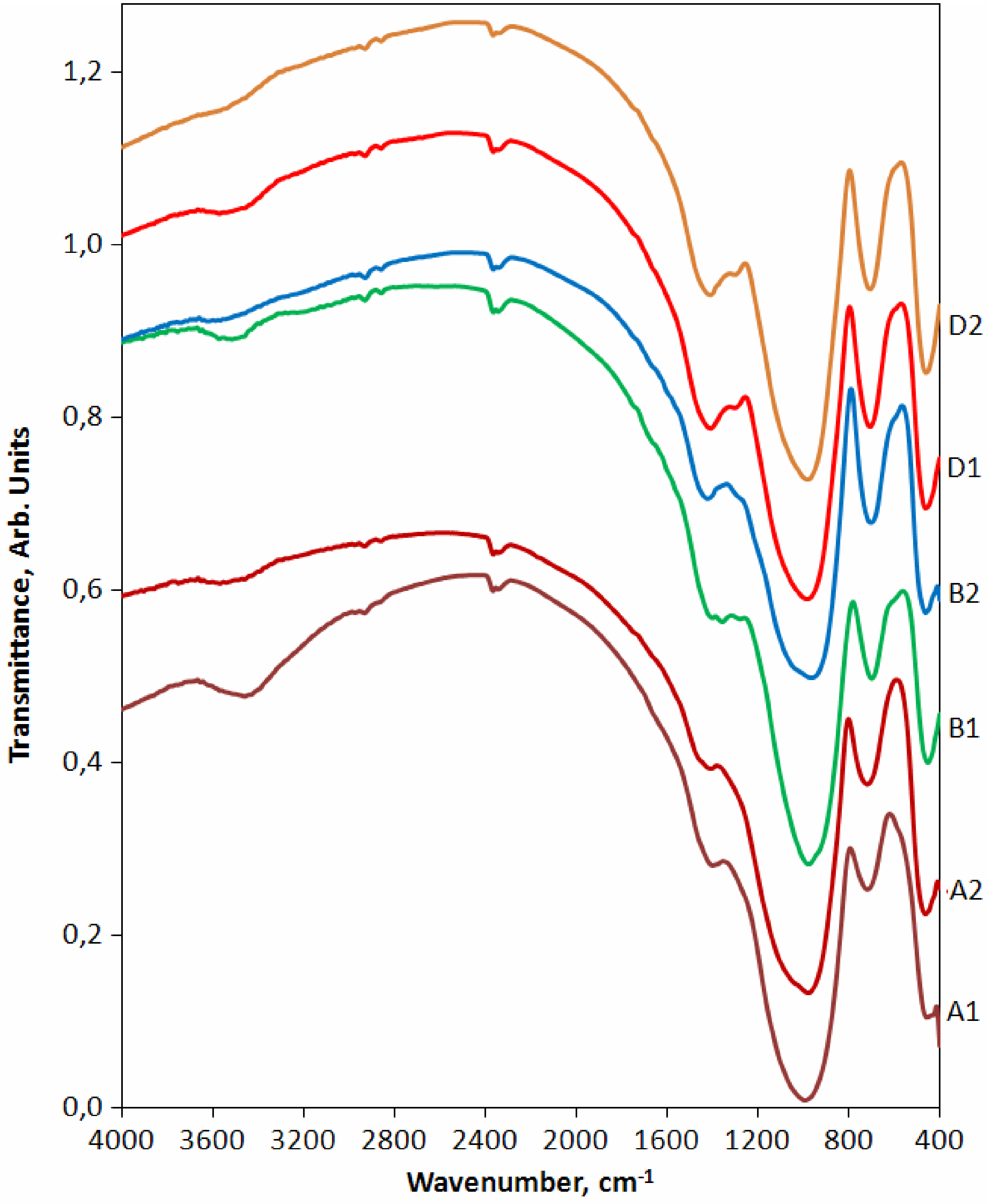

Figure 7. Infrared Spectra of Glasses within the Range of 4000-400 cm^{-1}.

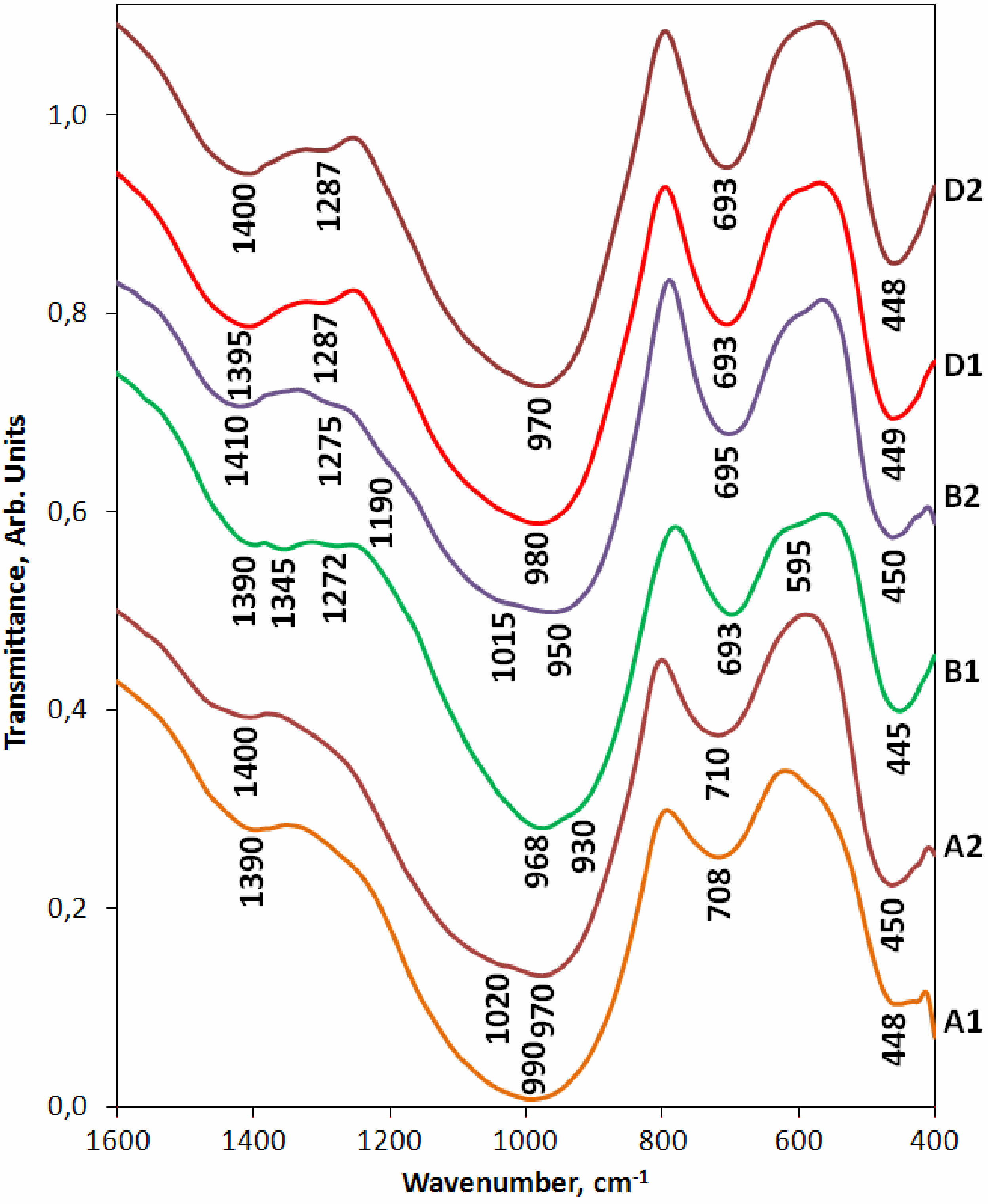

Figure 8. Fragments of Infrared Spectra of Glasses within the Range of 1600-400 cm^{-1}.

cm^{-1} and stronger band within the range of 650-800 cm^{-1}. Because these bands are associated with ternary coordinated boron, it may be concluded that its amount is low that is consistent well with theoretical representations. Nevertheless, major contribution to the band at 650-800 cm^{-1} is made by Al—O oscillations in AlO_4 tetrahedra and symmetric stretching modes of Si—O^- bonds. Incorporation of 5 mol.% Fe_2O_3 in glass does not effect on its IR spectra with the exception of very weak absorption near 575 cm^{-1} which may be assigned to oscillations of Fe—O bonds in FeO_4 tetrahedra [20].

In the whole, the structure of A1 and A2 glasses is formed by network of SiO_4 and AlO_4 tetrahedra with minor contribution of BO_4 tetrahedra; some of them enters complex borate groups with BO_3 triangles.

IR spectra of glasses B1 and B2 are also similar (Figures 7-9) but some different from those of glasses A1 and A2. We observe weak band centered at 1390-1410 cm^{-1} and a shoulder at ~1272-1275 cm^{-1} due to oscillations in the units with trigonally coordinated boron, two broad strong bands within the range of 800-1200 cm^{-1} and 400-550 cm^{-1} due to stretching and bending modes of Si—O—Si bridges and Si—O^- bonds and moderate on intensity band at 700-800 cm^{-1}. IR spectra of glasses B1 and B2 within the range of -800-1200 cm^{-1} differ in intensities of higher and lower wavenumber components. In the spectrum of glass B1 this band has a maximum at 968 cm^{-1} and a shoulder at ~930 cm^{-1} whereas in the spectrum of the glass B2 maximum of this band is positioned at 950 cm^{-1} while the lower intensity shoulder is located at ~1015 cm^{-1}. Thus, incorporation of 5.3 mol.% Fe_2O_3 in glass increases fraction of Q^2 and Q^1 units and, therefore, the number of non-bridging oxygen ions or decrease the degree of polymerization of the structural network although this effect is negligible.

Combining of IR spectra of glass B1 and nepheline [21] it can be shown that no combination of their spectra would allowed to obtain spectra of carnegieite/nepheline containing glass B2 (Figure 10). Increase of nepheline content in glass should result in growth in intensity absorption within the range of 950-1000 cm^{-1} and formation of additional bands at lower wavenumber values (see spectra 95/05, 90/10, 85/15, 80/20, and N on Figure 10). However, this does not occur. Therefore, cernegieite/nepheline content in glass is within the accuracy of determination by XRD, i.e. ≤ 5 vol.%.

IR spectra of glasses D1 and D2 are some different from those of other glasses. Major difference is much stronger absorption in wavenumber range of 1250-1550 cm^{-1}. If in the spectra of glasses A1, A2, B1 and B2 a weak shoulder a ~1280-1285 is present, then in the spectra of glasses D1 and D1 well-formed band centered at ~1285-1300 cm^{-1} occurs. Because the bands centered at ~1400 and ~1270-1300 cm^{-1} are due to ternary coordinated boron, it may be concluded that the fraction of trigonally coordinated boron in D1 and D2 glasses is much higher than in other glasses. This is in a good agreement with theoretical suggestions – the ψ_B factor for these glasses is about 1 whereas for A and B glasses it is about 3. The edge of broad band at 850-1200 cm^{-1} is shifted to higher wavenumbers pointing to markedly smaller contribution of four-coordinated boron as compared to A and B glasses. High wavenumber side of this band is similar to that of A1 and A2 glasses.

In the whole, glasses D1 and D2 have lower degree of connectedness (polymerization) of silicon-oxygen network as follows from lower wavenumber maxima of the band due to vibrations in SiO_4 tetrahedra and low intensity of its higher wavenumber component.

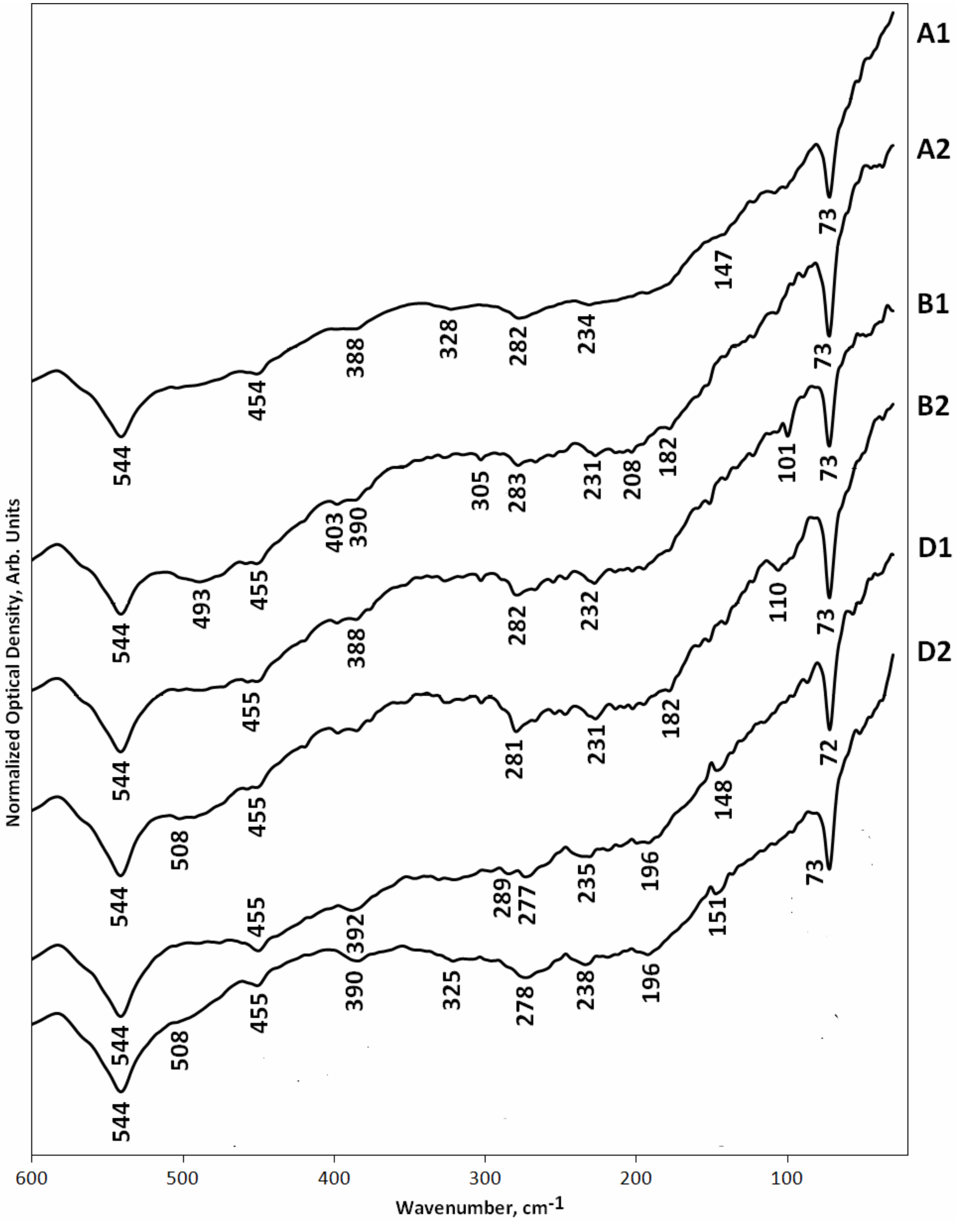

Figure 9. Infrared Spectra of Glasses within the Range of 600-30 cm^{-1}.

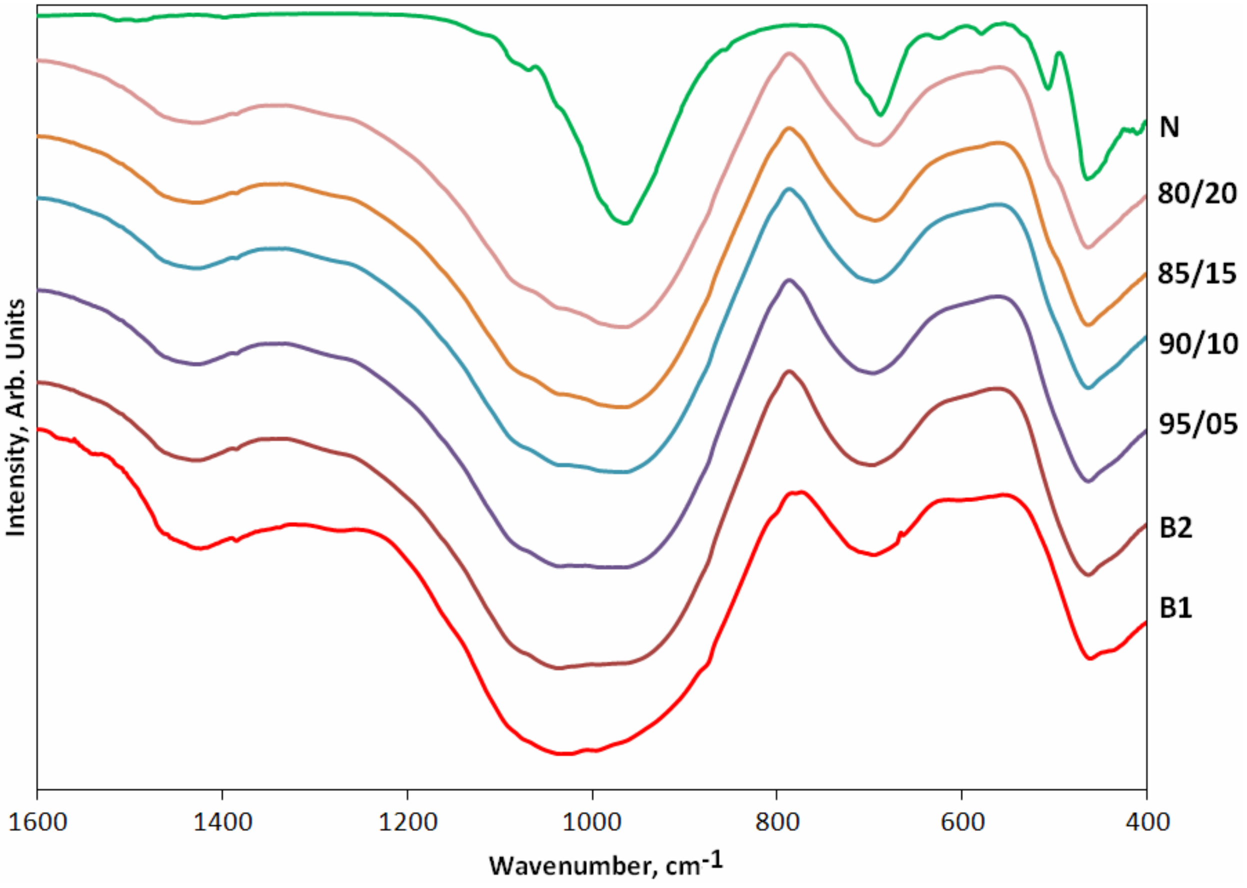

Figure 10. Combination of IR Spectra of Glass B2 and Carnegieite/Nepheline at Various Ratios. N – carnegieite/nepheline, the rest spectra are B2/N.

IR spectra of the glasses heat-treated at 500 °C for 10 hrs were also recorded (Figures 11 and 12). Major difference in spectra of heat-treated glasses is splitting of the bands due to vibrations in SiO_4 terahedra. This normally occurs at structural ordering in the glass network due to formation of pre-crystallization areas following by devitrification. Glasses A1, A2 and D2 seem to be structurally ordered in the most extent. The band at 800-1200 cm^{-1} in spectra of glasses B1, B2 and D1 is worse resolved than in the spectra of glasses A1, A2 and D2. In the spectrum of iron-containing glass B1 its components are ~1160 (shoulder), 1045, 1005, 975, ~885, and 808 cm^{-1} (shoulders).Some of them may be assigned to the contribution of nepheline (~1085, 1045, ~1000, ~700, ~520 and ~480 cm^{-1} [18,19]). In the spectrum of iron free glass B2 the band contains components ~1082 (shoulder), 1045, 970, and 885 cm^{-1} (shoulder). The difference in location of the bands may be assigned to the effect of iron.

Shoulders at ~808 and 788 cm^{-1} are probably symmetric stretching modes of Si—O—Al or Si—O—B bridges whereas a weak band at ~600 cm^{-1} in the spectrum of glass B1 is due to contribution of Fe—O bonds in FeO_4 tetrahedra. Weak splitting of the band at 650-750 cm^{-1} is due possibly to formation of AlO_4 tetrahedra with various number of non-bridging oxygen ions.

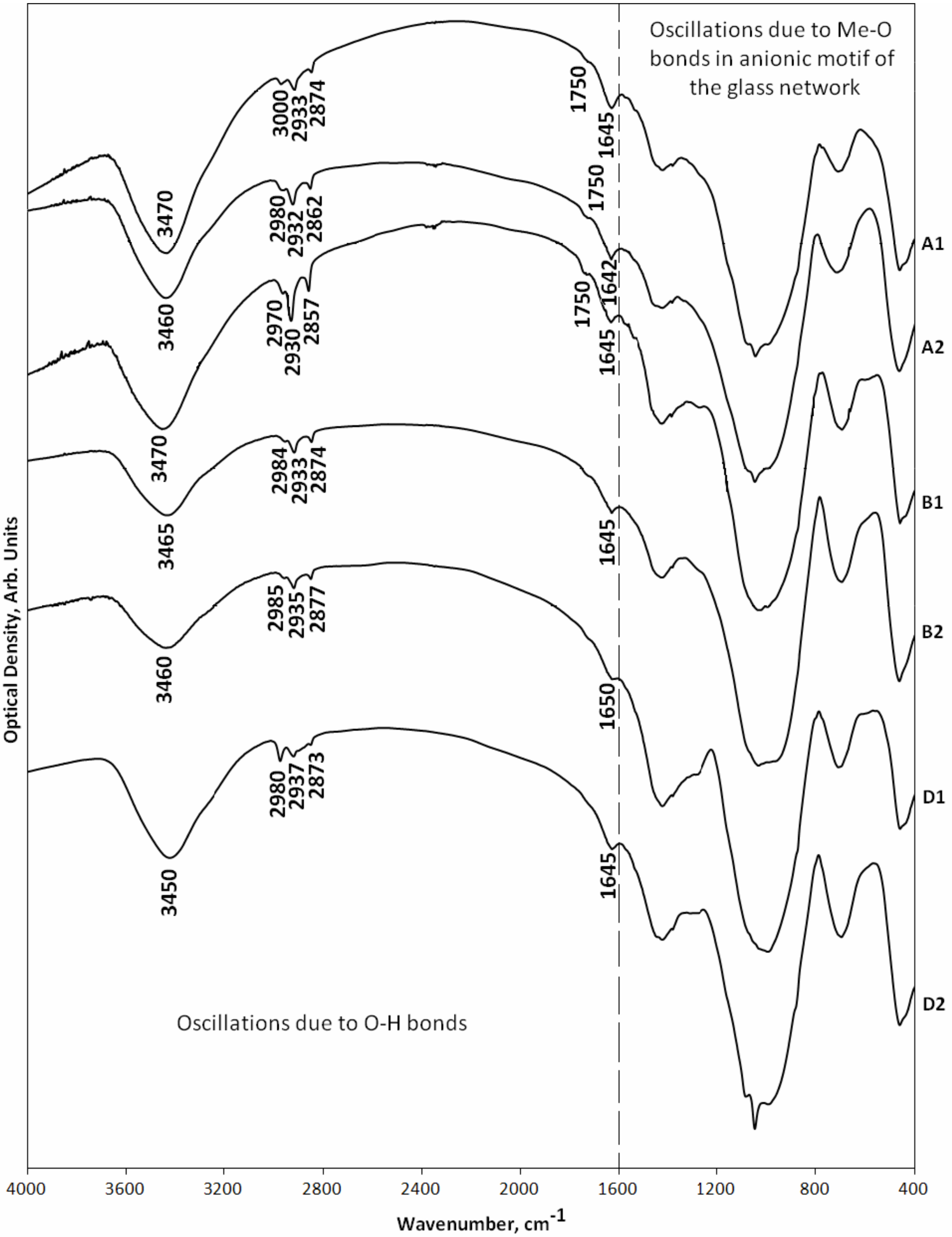

Figure 11. IR Spectra of Glasses Heat-Treated at 500 °C.

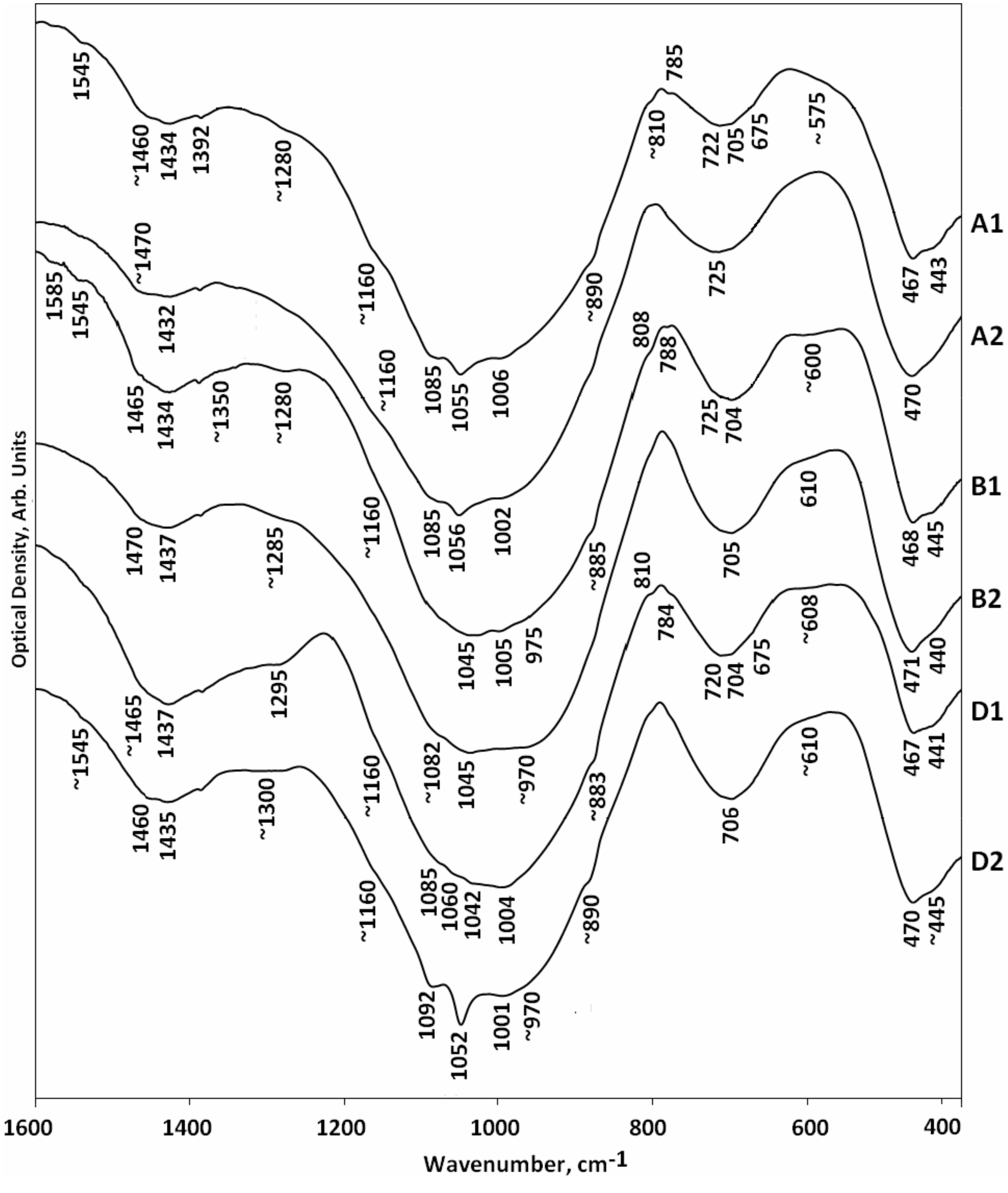

Figure 12. Fragments within the Range of 1600-400 cm^{-1} of IR Spectra of Glasses Heat-Treated at 500 °C.

Raman Spectra of Glasses

Raman spectra of the glasses studied are shown on Figure 13. Like FTIR spectra Raman spectra consist of strong bands within the ranges of 300-600 and 850-1200 cm^{-1} and weaker bands at 700-800 and 1250-1550 cm^{-1} but unlike FTIR spectra in the Raman spectra we may see different location of major bands due to stretching and bending modes in various structural units of glasses. There is a significant difference between Raman spectra of iron-containing and iron-free glasses especially within the range of 850-1200 cm^{-1}. The band at 850-1200 cm^{-1} consists of two major components at lower (850-1000 cm^{-1}) and higher (1000-1200 cm^{-1}) wavenumber ranges. In the spectra of iron free glasses the second component is stronger than the first one whereas in the spectra of iron-containing glasses – on the contrary. Since these components correspond to stretching modes in Q^0+Q^1+Q^2 units and Q^3+Q^4 SiO_4 units, respectively, it may be concluded that Fe^{3+} (and Fe^{2+} ions if present) offer destructive effect on structural network of these glasses.

Within the range of 300-600 cm^{-1} bending modes in SiO_4 and AlO_4 tetrahedra are observed. In iron free glasses this band is multicomponent. Incorporation of Fe_2O_3 in glasses results in broadening of this band and collapse of weak narrow bands in this range due to gaining of absorption at superimposing of the modes due to Fe—O bonds.

For understanding of the structure of glasses in more details computer simulation is required. Glasses A1 and A2 are similar in chemical composition but unlike glass A2 glass A1 contains 5 mol.% Fe_2O_3. Raman spectrum of iron free glass A2 may be represented as a superposition of the bands centered at 449, 511, 578, 631, 695, 771, 941, 1042, 1074, 1333, and 1556 cm^{-1} (Figure 14). Strong bands centered at 449 (broad) and 511 cm^{-1} (narrower) may be attributed to bending modes in the SiO_4 units with various number of non-bridging oxygen ions. Much weaker bands centered at 578, 695 and 771 cm^{-1} are due to stretching modes of Al—O^- bonds in AlO_6 (first of them) and AlO_4 units. The band centered at 631 cm^{-1} is due to symmetric valence oscillations (ν_1 stretching modes) of Si—O—Si(Al) bridges in depolymerized silicate or aluminosilicate anions. Weak bands centered at 941, 1333 and 1556 cm^{-1} may be attributed to oscillations of B—O bonds in BO_4 (first of them) and BO_3 units with various number of non-bridging oxygen ions. The bands centered at 1042 and 1074 cm^{-1} are due to ν_3 stretching modes in SiO_4 teterahedra with two (Q^2) and three (Q^3) bridging oxygen ions. Broad band centered at 1042 cm^{-1} may be also given a contribution due to Q^4(*m*Al) structural units [22].

Raman spectrum of glass A1 is simpler than that of glass A2 (Figure 14). Computer simulation gives the following set of overlapped bands centered at 476, 750, 926, 1031, and 1391 cm^{-1}. It is seen well that the band centered at 476 cm^{-1} is a superposition of narrower lines due to bending modes in SiO_4 units various number of non-bridging oxygen ions (350-550 cm^{-1}) and stretching modes of Fe—O bonds in FeO_4 tetrahedra (550-600 cm^{-1}) as well as ν_1 stretching modes of Si—O—Si(Al) bridges. The band centered at 750 cm^{-1} is due to stretching modes of Al—O^- bonds in AlO_4 tetrahedra. Strong broad asymmetric band within the range of 850-1150 cm^{-1} is a superposition of the bands centered at 926 and 1031 cm^{-1} (ν_3 stretching modes in Q^1 and Q^2 tetrahedra, respectively). Thus, Raman spectra unambiguously demonstrate depolymerizing effect of Fe_2O_3 on glass network resulting in formation of pyro-groups $Si_2O_7^{4-}$ or short chains of SiO_4 tetrahedra. Broad band centered at 1391 cm^{-1} is due to oscillations in BO_3 units.

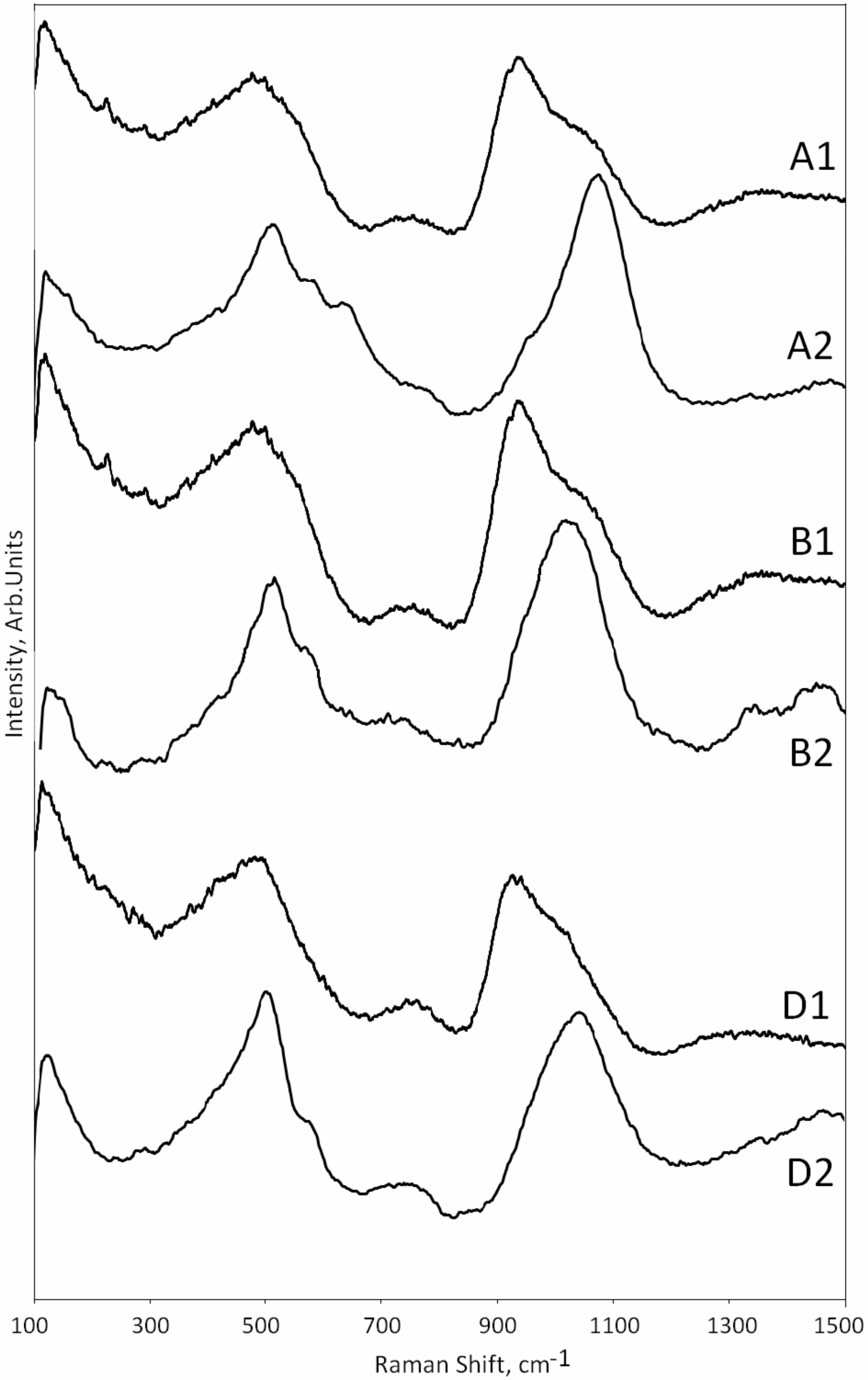

Figure 13. Raman Spectra of Glasses.

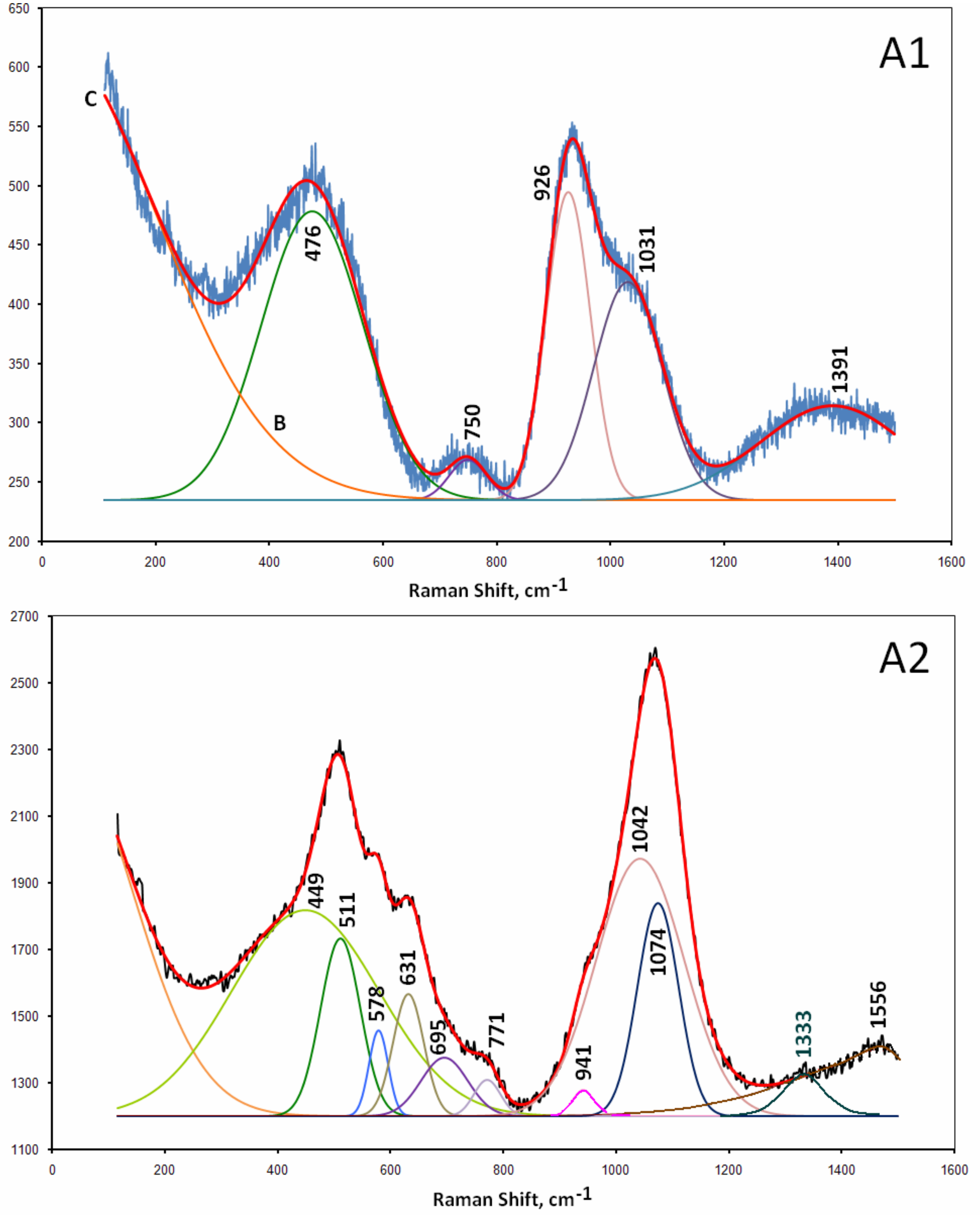

Figure 14. Computer Simulation of Raman Spectra of Glasses A1 and A2.

B – baseline, C – calculated line.

Like previously considered glasses B1 and B2 have similar chemical composition but glass B1 contains 5.3 mol.% Fe_2O_3. These glasses should have B^{III}/B^{IV} ratio similar to glasses A1 and A2 due to close ψ_B values (Table I).

As follows from computer simulation of Raman spectrum of glass B2 its low wavenumber range is similar to that of glass A2 (Figure 15) with the exception of two weak bands centered at 219 and 228 cm^{-1}. The broad band within the range of 300-600 cm^{-1} may be resolved into components 449, 511, 573, 618 and 713 cm^{-1}. As it was discussed above the bands centered at 449 and 511 cm^{-1} are due bending modes of Si—O bonds in SiO_4 tetrahedra. The band centered at 573 cm^{-1} may be identified as the band at 578 cm^{-1} in glass A2 and assigned to stretching modes of Al—O^- bonds on AlO_6 octahedra, whereas the band centered at 713 cm^{-1} is due to stretching modes of Al—O^- bonds on AlO_4 tetrahedra. Unlike Raman spectrum of glass A2 in spectrum of B2 glass the band within the range of 850-1150 cm^{-1} is nearly symmetric Gaussian with a maximum at 1012 cm^{-1} pointing to predominant Q^2 tetrahedra in its structure. Two bands in high wavenumber range centered at 1335 and 1446 cm^{-1} are due to BO_3 triangles predominantly isolated and bound three-dimensionally, respectively.

Incorporation of 5.3 mol.% Fe_2O_3 in glass (over 100 mol.%) yields spectrum very similar to that of glass A1 (Figures 14 and 15). In low wavenumber range of spectrum of glass B2 a strong broad band centered at 488 cm^{-1} due to bending modes of Si—O^- and Si—O—Si bonds occurs. The band centered at 746 cm^{-1} is due to stretching modes of Al—O bonds in AlO_4 tetrahedra. Strong band due to oscillations in SiO_4 tetrahedra becomes asymmetric and is composed of components at 902 and 988 cm^{-1} which may be attributed to ν_3 stretching modes of Si—O bonds in Q^1 and Q^2 units, respectively. In spite of Q^2 units remain major constituent of the structure of glass B2, formation of Q^1 units shows destructing effect of Fe^{3+} ions on glass network. Occurrence of BO_3 triangles is responsible for weak band centered at 1327 cm^{-1}. Minor contribution may be also brought by BO_4 tetrahedra into the edge of major band within the range of 900-1000 cm^{-1}.

For the spectrum of iron free glass D2 the best fit was achieved at a set of lines centered at 354, 480, 503, 577, 658, 744, 943, 1028, 1275, and 1491 cm^{-1} (Figure 16). As discussed above, the bands in low wavenumber range are due to bending modes in SiO_4 tetrahedra and stretching modes in AlO_4 tetrahedra. In the spectrum of iron-containing glass D1 this range is approximated by the only band with a maximum at 474 cm^{-1} due to superposition of several bands including stretching modes of Fe—O bonds. However their contribution is minor due to low Fe_2O_3 content in glass.

Major band in high wavenumber range is resolved into components at 915 and 992 cm^{-1}. They may be attributed to ν_3 stretching modes of Si—O bonds in Q^1 and Q^2 tetrahedra, respectively. Because the band centered at 992 cm^{-1} is broader, it may be suggested that it contains some contribution of stretching modes of B—O bonds in BO_4 tetrahedra. Two weak overlapped bands with maxima at 1246 and 1323 cm^{-1} are due to oscillations in BO_3 triangles.

In the whole, in all the glasses studied incorporation of Fe_2O_3 offers destructive effect on glass network.

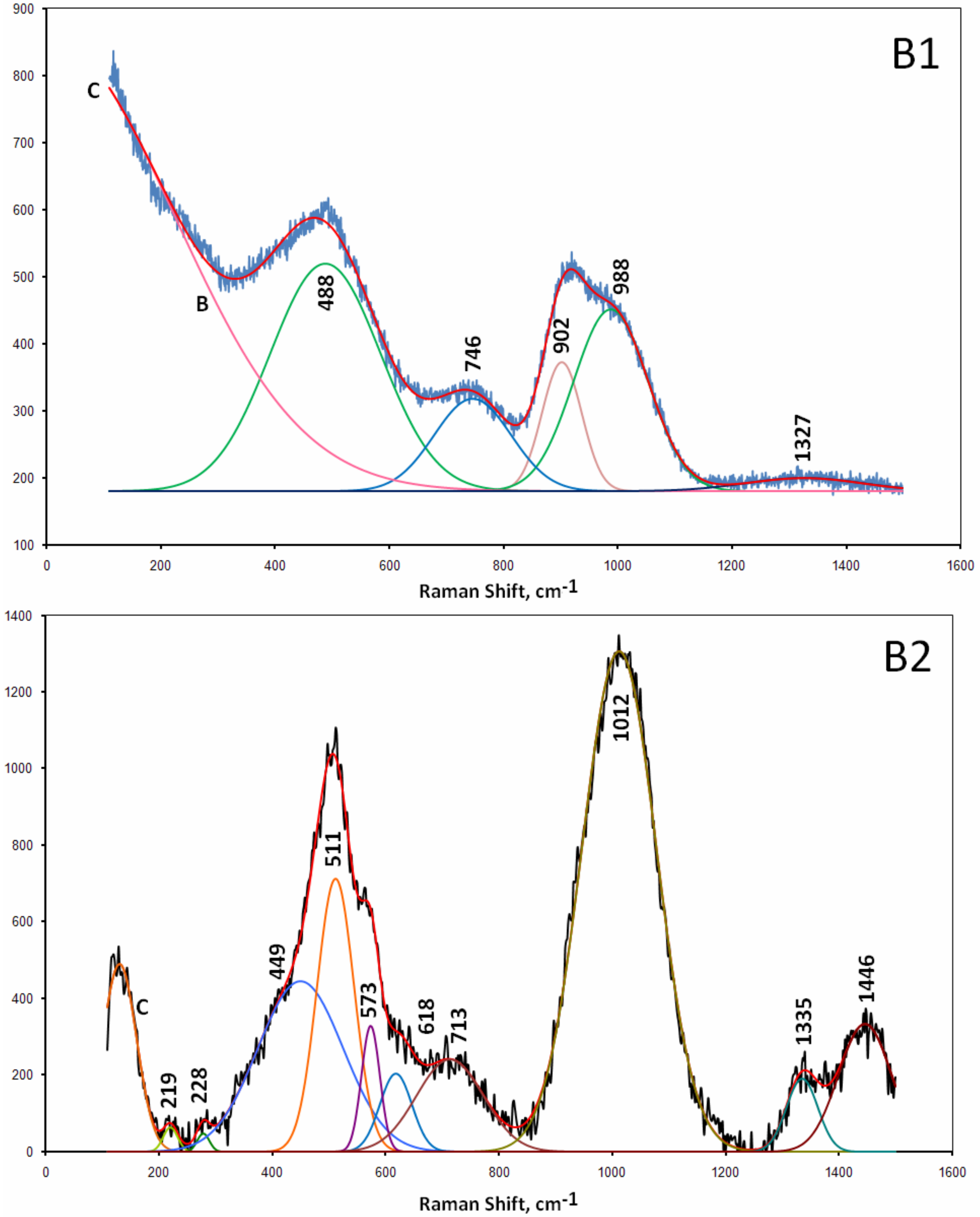

Figure 15. Computer Simulation of Raman Spectra of Glasses B1 and B2.

B – baseline, C – calculated line.

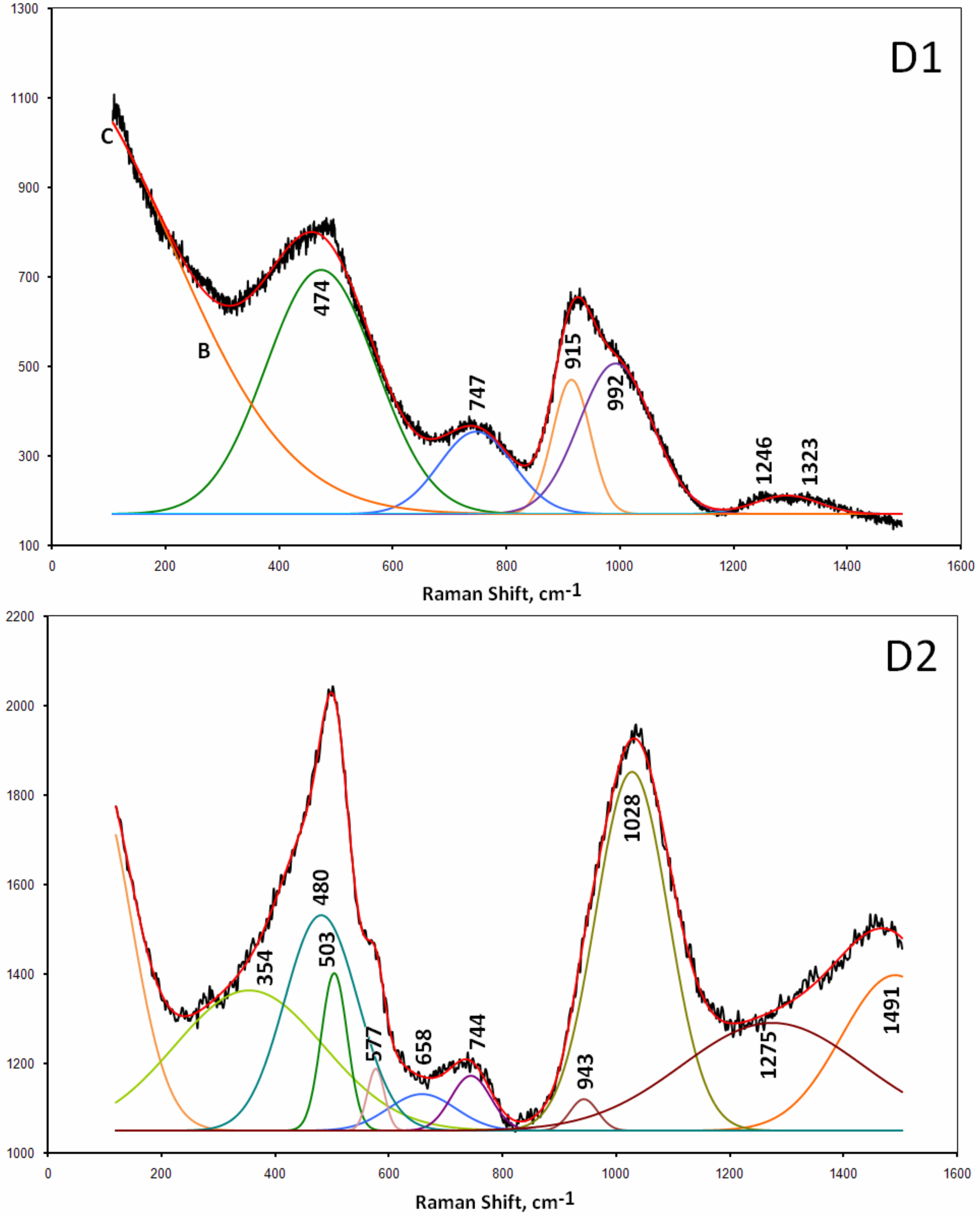

Figure 16. Raman Spectra of Glasses D1 and D2.

B – baseline, C – calculated line.

XAS Study

XANES spectra of Fe K edge in glasses A1, B1 and D1 and their first derivatives are shown on Figures 17 and 18, respectively. Spectrum of Fe K edge in glass D1 is slightly different from spectra of glasses A1 and B1. As follows from comparison with reference data [23] spectra may be attributed to Fe^{3+} ions in mixed tetrahedral and octahedral oxygen environment. Minor Fe^{2+} ions may be also present, especially in glass D1.

Comparison of first derivatives (FD) of XANES spectra (Figure 18) with reference data [24] demonstrates that FD of Fe K XANES spectra of glass A1 is similar to that of glass with $NaFeSi_2O_6$ formulation. FD of spectra of glass B1 is intermediate between those of glasses with $NaFeSi_2O_6$ (Fe^{3+}) and $CaFeSiO_4$ or $CaFeSi_2O_6$ (Fe^{2+}) formulations. FD of spectra of glass D1 demonstrates some higher contribution due to Fe^{2+}.

Fourier transform (FT) EXAFS spectra of Fe K edge in glasses are shown on Figure 19. It is seen well that only first coordination shell is appeared. Therefore, Fe ions are quite homogeneously distributed over glass bulk.

Computer fitting (Table XIII) of the Fe K Edge EXAFS Spectra shows that Fe in glass A1 has average coordination number (CN) 5.5, i.e. ~75% Fe ions have CN = 6 and ~25% Fe – CN = 4. Major Fe ions have distorted octahedral oxygen environment with symmetry close to rhombic. In the structure of glass B1 average Fe CN = 4.6, i.e. ~70% Fe ions occupy tetrahedral sites and ~30% - octahedral sites. In the glass D1 average CN = 3.7 pointing to tetrahedral oxygen environment of Fe ions. At that, in the structure of glass B1 Fe environment is the least distorted.

Second coordination shell actually exists even though is weakly manifested. The nearest neighbor (oxygen or different element) is located at a distance of 3.59-3.66 Å with CN = 1.5-1.9. This neighboring atom is better seen on Morlet-Wavelet transforms (Figure 20).

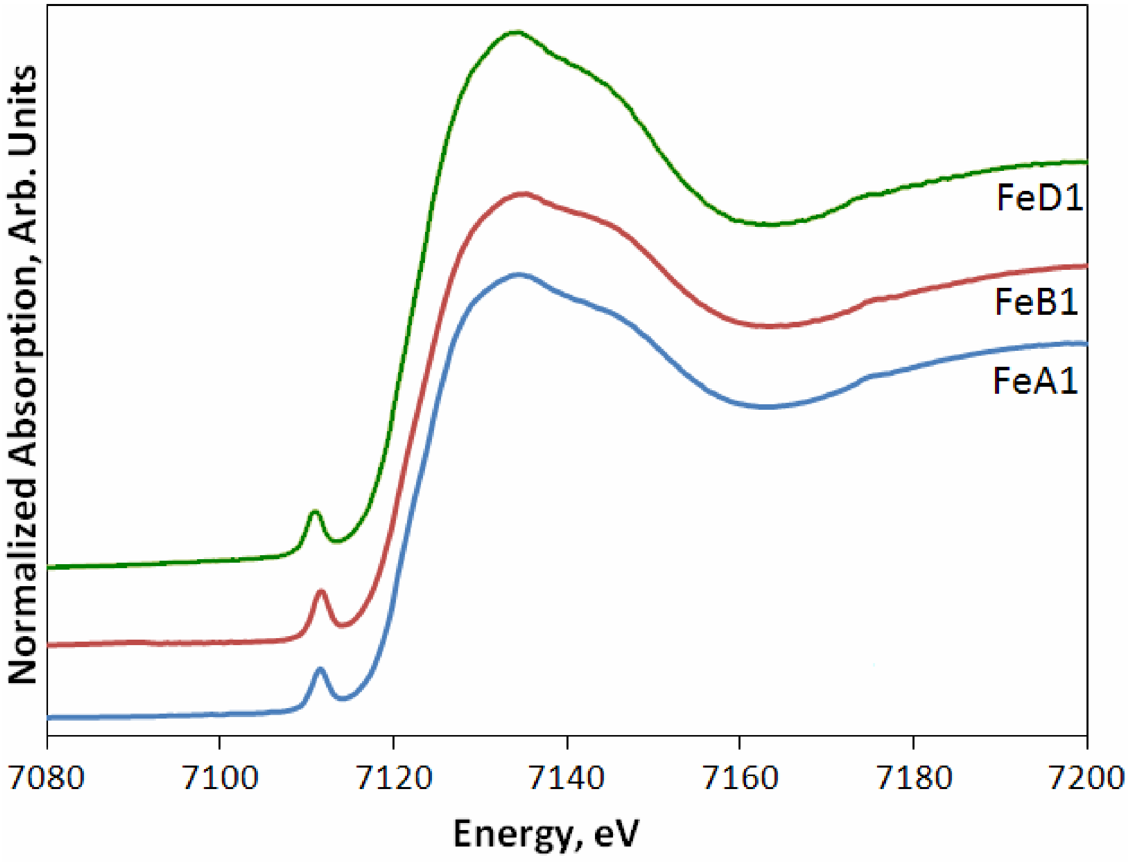

Figure 17. XANES Spectra of Fe K Edge in Glasses.

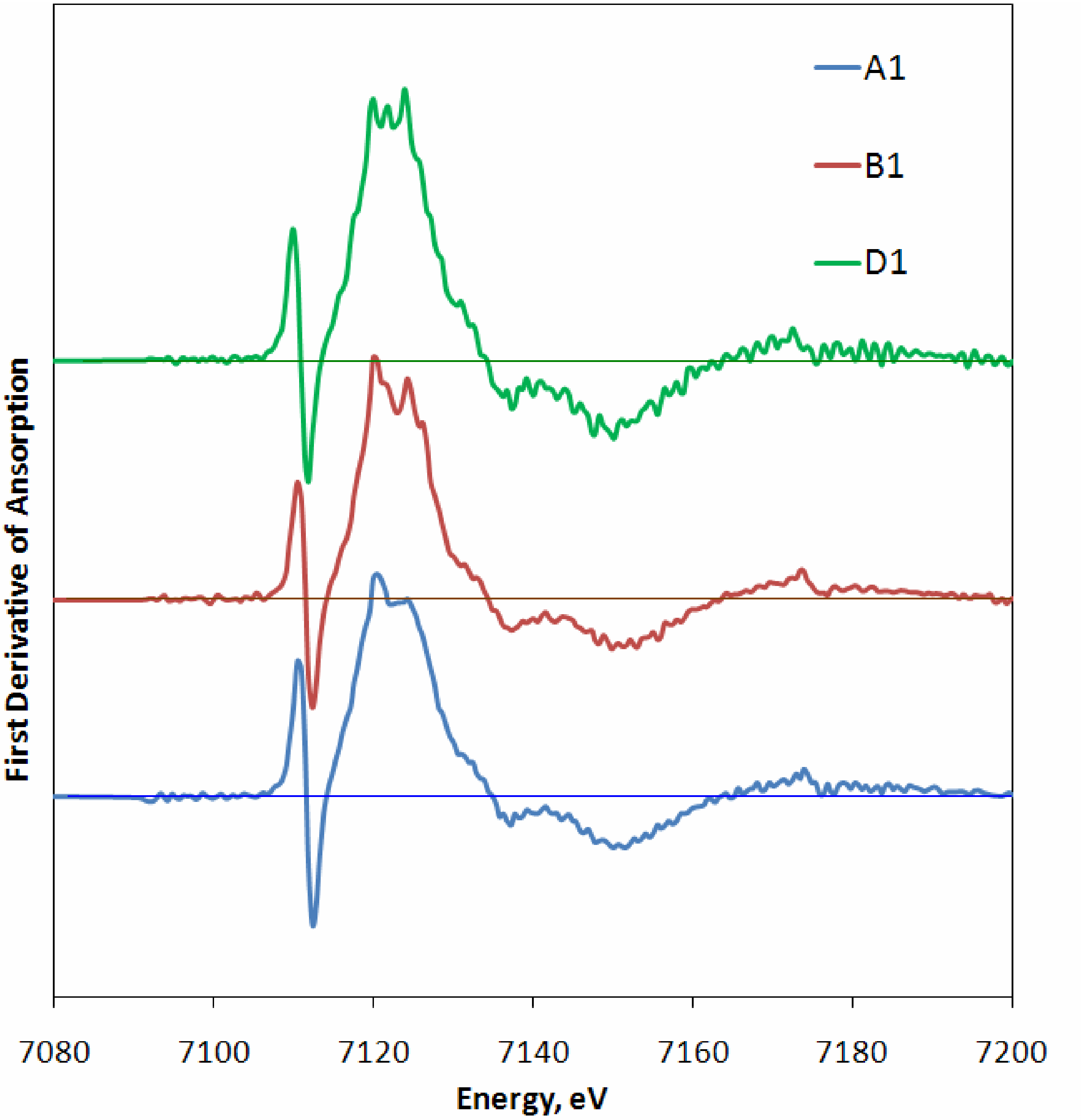

Figure 18. Differential XANES spectra of Fe K edge in glasses.

Table XIII. Fitting of the Fe K Edge EXAFS Spectra of Glasses.*

Glass	A1		B1		D1	
Bond	CN	R—O, Å	CN	R—O, Å	CN	R—O, Å
Fe-O1	2.9±0.2	1.75±0.01	2.7±0.1	1.83±0.01	2.1±0.3	1.81±0.01
Fe-O2	2.6±0.1	1.85±0.01	1.9±0.1	1.85±0.01	1.6±0.2	1.87±0.01
Fe-O3(Me)	1.5±0.2	3.66±0.03	1.9±0.2	3.59±0.03	1.6±0.1	3.6±0.1

* Debye-Waller factor was assumed to be 0.005 Å^{-1}.

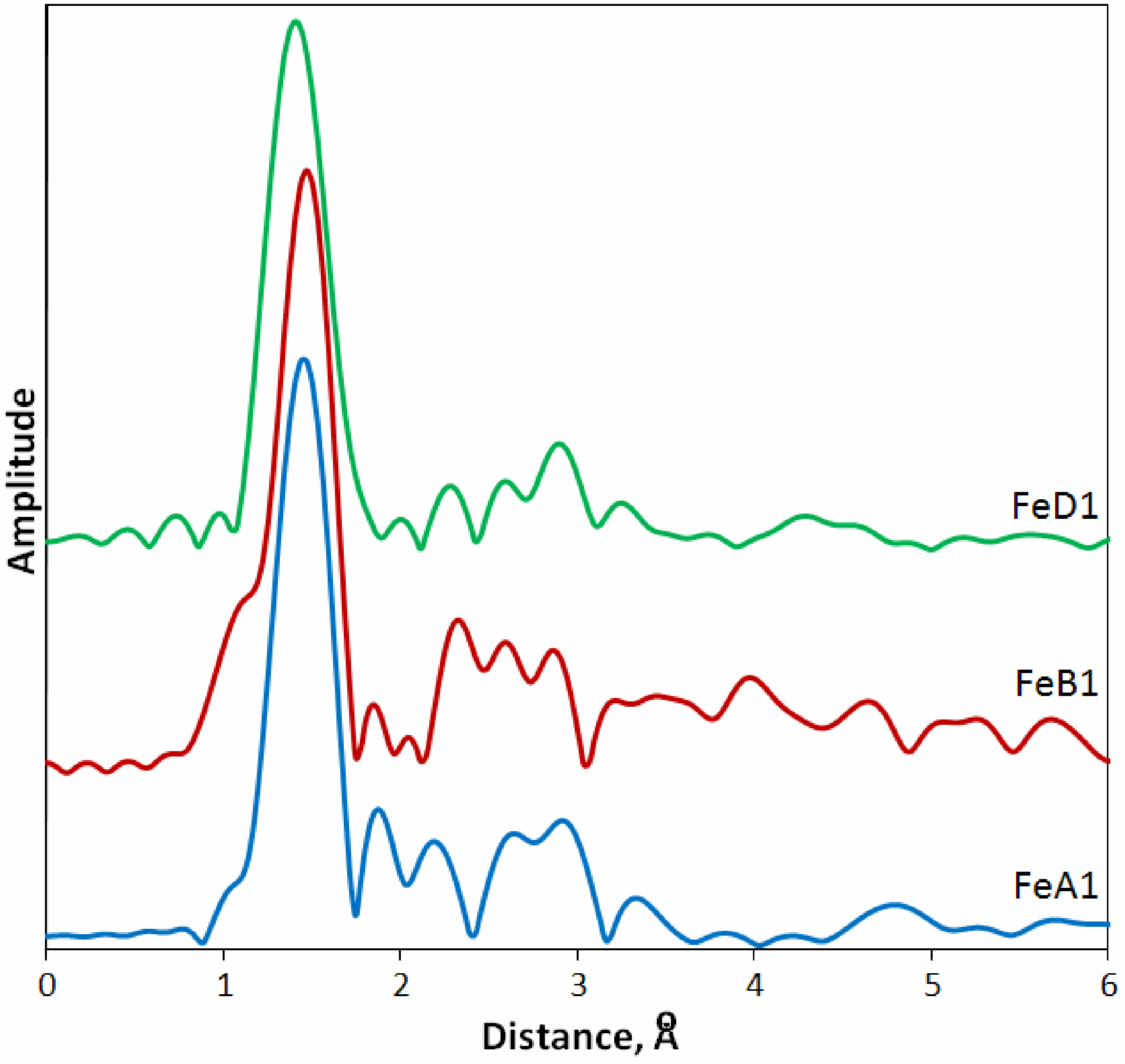

Figure 19. FT EXAFS of Fe K Edge in Glasses.

No phase shift correction.

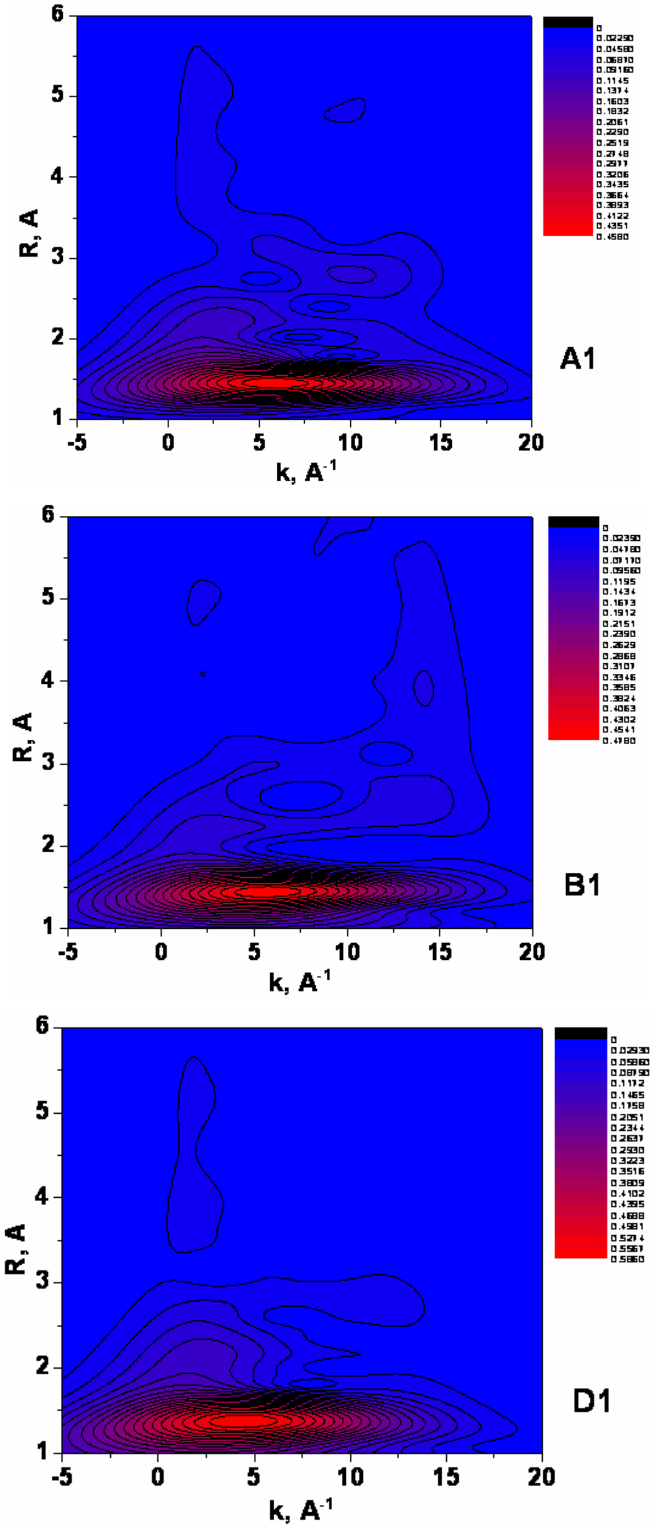

Figure 20. Morlet Wavelet Transform of Fe K Edge EXAFS Spectra of Glasses A1, B1 and D1.

CONCLUSIONS

- Materials A1, A2, B2, D1, D2 are X-ray amorphous (glasses); the material B1 is also amorphous but contains trace of crystalline phases carnegieite/nepheline and spinel;
- No liquid-liquid phase separation in glasses was found;
- FTIR spectra show minor effect of Fe_2O_3 on the structure of the anionic motif of the glasses studied;
- As follows from Raman spectra incorporation of Fe ions offers destructive effect on glass network increasing the number of non-bridging oxygen ions and thus fraction of SiO_4 tetrahedra with lower degree of connectedness;
- Fe occurs predominantly in a trivalent form as Fe^{3+} ions but some minor fraction of Fe^{2+} is also present; the highest fraction of Fe^{2+} ions was found in glass D1;
- In the structure of glass A1 Fe^{3+} ions have CN = 5.5 (75% Fe ions occupy octahedral sites and 25% - tetrahedral), in the glass B1 average CN = 4.6 (70 Fe ions occupy tetrahedral sites and 30% - octahedral), in the glass D1 average CN = 3.7 (Fe^{3+} ions are octahedrally coordinated);
- Both tetrahedral and octahedral Fe sites undergo majorly rhombic distortion with short Fe—O distance 1.75-1.83Å and long distance 1.85-1.87 Å.
- Second coordination shell of Fe ions is not clearly manifested, therefore, Fe ions are quite homogeneously distributed within the glass bulk;
- The nearest to Fe ion neighbor (oxygen or heavier element) is located at a distance of 3.59-3.66 Å with CN = 1.5-1.9.

REFERENCES

1. H. Li, P. Hrma, J.D. Vienna, M. Qian, Y. Su, D.E. Smith, *J. Non-Cryst. Solids*, **331** (2003) 202 – 216.
2. J.C. Marra, D.K. Peeler, T.B. Edwards, A.L. Youchak, J.H. Gillam, Jr., J.D. Vienna, S.V. Stefanovsky, A.S. Aloy, *Mat. Res. Soc. Symp. Proc.* **1107** (2008) 231-238.
3. S.V. Stefanovsky and J.C. Marra, *Waste Management '07. Proc. Int. Conf.* Tucson, AZ, 2007. ID 7132. CD-ROM.
4. J. Wong, C.A. Angell, *Glass Structure by Spectroscopy*, Marcel Dekker, N.Y. (1976).
5. J.G. Darab, J.C. Linehan, B.P. McGrail, *Mat. Res. Soc. Symp. Proc.* 556 (1999) 337-344.
6. D. Holland, B.G. Parkinson, M.M. Islam, A. Duddridge, J.M. Roderick, A.P. Howes, C.R. Scales, *Mater. Res. Soc. Symp. Proc.* 1107 (2008) 199-206.
7. B. Ravel and M. Newville, *J. Synchrotron Radiat.* **12** 537-541 (2005).
8. A.L. Ankudinov and J.J. Rehr, *Phys. Rev.* B **56** 1712-1716 (1997).
9. H. Funke, A.C. Scheinost and M. Chukalina, *Phys. Rev. B*, **71**, 094110 (2005).
10. H. Funke, M. Chukalina and A.C. Scheinost, *J. Synchrotron Radiat.* **14**, 426-432 (2007).
11. www.esrf.fr/exp_facilities/BM20/Software/Wavelets.html.
12. A.A. Appen, *Chemistry of Glass* (Russ.), Khimiya, Leningrad (1974).
13. S.V. Stefanovskii, O.A. Knyazev, T.N. Lashchenova, and S. Merlin, *J. Adv. Mater.* **3** [6] (1996) 479-487.
14. G.B. Bokiy, *Crystal Chemistry*, (Russ., Moscow State University Publ., 1960).
15. R.D. Shannon, *Acta Cryst.* **A32** (1976) 751-767.
16. A.P. Kobelev, S.V. Stefanovsky, V.V. Lebedev, M.A. Polkanov, O.A. Knyazev, J.C. Marra. Cold Crucible Vitrification of the Savannah River Site SB2 HLW Surrogate at High Waste Loading, *Glass Tech.: Eur. J. Glass Sci. Technol. A.* 50 [1] (2009) 47-52.
17. S.V. Stefanovsky, J.C. Marra, A.A. Akatov, Characterization of Vitrified Savannah River Site SB4 Waste Surrogate Produced in Cold Crucible, *Materials Science and Technology '08 Conf.* Pittsburg, PA (2008) 486020.
18. V.A. Kolesova, *Glass Phys. Chem.* (Russ.) **12** [10] 4-13 (1986).
19. V.N. Anfilogov, V.N. Bykov, and A.A. Osipov, Silicate Melts (Russ.), Nauka, Moscow (2005).
20. I.I. Plyusnina, *Infrared Spectra of Minerals* (Russ.), MGU, Moscow (1977).
21. http://rruff.info/nepheline/display=default/R040025
22. P.F. McMillan, B. Piriou, A. Navrotsky, *Geochim Cosmochim. Acta*. 46 (1982) 2021-2037.
23. G.E. Brown, Jr., G.A. Waychunas, C.W. Ponader, W.E. Jackson, and D.A. McKeown, *EXAFS and Near Edge Structure IV – J. de Physique*. 47 C8, suppl. Au n°12, C8-661 – C8-668 (1986).
24. N. Binsted, G.N. Greaves, and C.M.B. Henderson, *EXAFS and Near Edge Structure IV – J. de Physique*. 47 C8, suppl. Au n°12, C8-837 – C8-840 (1986).

Appendix B. Final Report from SIA Radon on Task 2: Electron Microscopy and Spectroscopy Studies of Amorphous Glasses with Poor Durability

FINAL REPORT

Subcontract Number AC69549N

Task 2: Electron Microscopy and Spectroscopy Studies of Amorphous Glasses with Poor Durability

Glass Structural Characterization and Analysis

INTRODUCTION

Vitrtification is one of the most perspective methods of nuclear waste volume reduction providing for production of glass waste form with high chemical durability, good radiation resistance and strong mechanical integrity. Currently two technologies based on Joule heated ceramic and inductively heated metallic melters are implemented at industrial scale. One more perspective technology – cold crucible inductive melting (CCIM) is under consideration and trial testing now. While the CCIM technology is applied for vitrification of low/intermediate waste at SIA Radon in Russia, feasibility study tests with high level waste (HLW) are still being conducted. At that, selection of appropriate glass composition is one of the key elements of the vitrification process. Savannah River National Laboratory (SRNL) has identified a small number of simulated, multi-component waste glass compositions that, while amorphous via XRD, have unusually poor chemical durability. The cause of the reduction in durability is not known, but is suspected to be amorphous phase separation. The objective of this task would be to recreate 4-6 of the previously identified glass compositions and characterize them using SEM in an attempt to screen for amorphous phase separation. If phase separation can be identified using SEM, EDS would be used to approximate the compositions of each phase. Fourier Transform Infra Red (FTIR) and Raman Spectroscopy would also be used in order to identify any changes in the chemistry and structure of these anomalous glasses and possibly each phase.

EXPERIMENTAL

Samples of glasses were delivered by customer (SRNL). Their target and actual chemical compositions are given in Table I.

Actual chemical compositions of the glasses were determined at SRNL using a Perkin-Elmer 403 ICP-AAS spectrometer. Samples were examined by X-ray diffraction (XRD) using a Rigaku D / Max 2200 diffractometer (Cu Kα radiation, 40 keV voltage, 20 mA current, stepwise 0.02 degrees 2θ), scanning electron microscopy with energy dispersive spectrometry using a JSM-5610LV+JED-2300 analytical unit, Fourier-transform infrared spectroscopy using a Perkin-Elmer 2000 Fourier spectrophotometer (compaction of glass powders in pellets with KBr at recording within the range of 4000-350 cm^{-1}, and placement of micron-sized powder between two glass plates at recording within the range of 600-30 cm^{-1}), and Raman spectroscopy using a Jobin Yvon U1000 spectrophotometer operated at an excitation wavelength of 532 nm.

X-ray absorption (XAS) spectra were recorded at the Structural Materials Science (STM) Beamline of the synchrotron source at RRC “Kurchatov Institute”. The glass samples were measured at room temperature either as dispersed powder or as pellets pressed from powder mixed with sucrose in the transmission mode using a Si(220) channel-cut monochromator and two air-filled ionization chambers. Fluorescence spectra were also acquired. Powders of chemically pure Fe oxides Fe_2O_3 and FeO were used as standards and measured under identical conditions. Experimental XAFS spectra were fitted in R-space using an IFEFFIT package [1] and crystal structures of corresponding oxides and silicates. In the fitting, *ab initio* photoelectron backscattering amplitudes and phases calculated self-consistently using FEFF8 [2] were used.

Wavelet transform (WT) is commonly applied to evaluation of complex time-frequency signals. As shown in refs [3,4], WT is easily adapted to EXAFS analysis, and the expression of the WT of the k^n-weighted EXAFS data takes the form:

$$W_\chi^\psi(k,r) = (2r)^{1/2} \int_{-\infty}^{\infty} \chi(k')k'^n\, \psi^*[2r(k'-k)]dk', \tag{1}$$

where $\chi(k)$ is the EXAFS signal and $\psi^*[2r(k'-k)]$ is the complex wavelet function.

The WT is able to resolve the k dependence of the absorption signal, which potentially allows separation of contributing backscattering atoms even situated at the same distances from the core. One of the advantages of the wavelet analysis is the visualization of the WT modulus in a k-R plot, which provides an easy way to interpret the results. Our analysis of EXAFS data for Pu and Hf were performed using the FORTRAN program HAMA employing Morlet wavelet algorithm [5]. The Morlet wavelet is well-suited for EXAFS signal since it consists of a slowly varying amplitude term and a fast oscillating phase term. Its mathematical description is broadly analogous to the Fourier transform. The Morlet wavelet is obtained by taking a complex sine wave with frequency η (as in FT) and by confining it with a Gaussian envelope with the half width σ,

$$\psi(k) = \frac{1}{(2\pi)^{1/2}\sigma} \exp(i\eta k)\exp(-k^2/2\sigma^2). \tag{2}$$

The choice of the η and σ parameters is important for data analysis since, besides other issues, it determines resolution in k-R space. Various combinations of these parameters were used in an attempt to resolve contributions from atoms at close distances from the central atom. As shown in ref.[4] use of higher k-weighting decreases resolution in the k-space, since backscattering amplitudes become flattened and shifted to higher values. Nevertheless, WT modulus plots for different k weights are shown to emphasize contributions of light and heavy backscatterers. Note, that in all plots of the WT modulus the interatomic distances are given without phase shift correction.

Table I. Chemical Compositions of Glasses in Series 21.

Oxides	FY09EM 21-02			FY09EM 21-07			FY09EM 21-21		
	Target		Actual	Target		Actual	Target		Actual
	Mol.%	Wt.%	Wt.%	Mol.%	Wt.%	Wt.%	Mol.%	Wt.%	Wt.%
Al_2O_3	2.71	4.01	4.31	3.25	4.87	5.07	3.21	4.86	4.75
B_2O_3	5.03	5.07	5.30	13.62	13.92	13.75	8.71	9.01	8.78
BaO	0.04	0.08	0.08	-	-	-	0.04	0.08	0.07
CaO	-	-	0.02	4.76	3.92	3.98	-	-	0.02
CdO	0.16	0.30	0.28	-	-	-	0.16	0.30	0.27
Ce_2O_3	0.16	0.36	0.40	-	-	-	0.16	0.36	0.38
Cr_2O_3	-	-	-	-	-	-	0.09	0.20	0.20
CuO	0.11	0.13	0.14	-	-	-	0.11	0.13	0.13
Fe_2O_3	8.92	20.63	22.25	7.67	17.98	17.85	8.41	19.95	23.40
La_2O_3	0.02	0.10	0.09	-	-	-	0.02	0.10	0.08
Li_2O	9.24	4.00	3.99	9.12	4.00	3.89	15.77	7.00	6.63
MgO	2.57	1.50	1.51	2.53	1.50	1.47	-	-	-
MnO	0.29	0.30	0.40	5.28	5.50	5.34	0.95	1.00	1.23
Na_2O	20.03	17.98	18.00	13.97	12.71	12.50	15.94	14.67	13.65
Nb_2O_5	-	-	1.20	-	-	1.16	-	-	1.12
NiO	2.31	2.50	-	-	-	-	-	-	-
PbO	0.07	0.22	0.22	-	-	-	0.07	0.22	0.21
SO_4	0.41	0.48	0.55	-	-	0.07	0.40	0.48	0.53
SiO_2	45.97	40.02	38.70	38.09	33.60	32.20	44.05	39.31	36.20
TiO_2	1.73	2.00	1.97	1.71	2.00	1.90	1.69	2.01	1.84
ZnO	0.11	0.13	0.13	-	-	-	0.11	0.13	0.12
ZrO_2	0.12	0.21	0.21	-	-	-	0.11	0.21	0.19
Total	100	100	99.75	100	100	99.18	100	100	99.80
ψ_B	~4			~1			~2		
ψ_B (Fe)	~3.5			~0.8			~1.7		

THEORETICAL REMARKS

There are several structural parameters characterizing some features of the structure of glasses. The most important among them are degree of connectedness of the silica-oxygen network (f_{Si}) for silicate-based and relative fraction of four-coordinated boron (ψ_B) for borate and borosilicate glasses [6]:

$$\psi_B = \{(Na_2O+K_2O+BaO)+[0.7(CaO+SrO)+[0.3(MgO+ZnO+PbO)]-Al_2O_3\}/B_2O_3 \qquad (3)$$

Formally, boron is three-coordinated if $0 \le \psi_B \le 1/3$ and forms boron-oxygen triangles. At $1/3 < \psi_B < 1$ both three- and four-coordinated boron atoms co-exist and are present in complex borate groups. At $\psi_B \ge 1$ all the boron is four-coordinated and forms boron-oxygen tetrahedra associated with alkali and, in less extent, alkali earth cations as, for example, $Me^+[BO_{4/2}]$ units. Actually, significant excess of alkali or/and alkali earth oxides as oxygen donors to form BO_4 tetrahedra and convert all the boron into four-coordinated state is needed. This process depends also on silica content in glass. At relatively high silica content (60-80 wt.%) the ψ_B value is estimated to be 1.5-2. At lower silica contents (44-60 wt.%) this value should be much higher. We have demonstrated using IR and electron paramagnetic resonance (EPR) spectroscopy that in borosilicate glasses for high-sodium intermediate level waste immobilization containing 40-50 wt.% SiO_2 minor fraction of trigonally coordinated boron is present even at $\psi_B \cong 4\div5$ [7].

Aluminum offers negative effect on transformation of trigonally coordinated boron into tetragonally coordinated one. Due to higher strength of Al—O bond as compared to B—O bond oxygen delivered by alkali oxides is firstly spent for formation of AlO_4 tetrahedra and at relatively high Al_2O_3 concentrations major boron remains three-coordinated [6]. Nevertheless this does not offer negative effect on chemical durability of glasses, because aluminosilicate glass network built from SiO_4 and AlO_4 tetrahedra with associated alkali ions is leach resistant [8,9].

Effect of iron oxides on boron coordination in borosilicate glasses is more complicated. Fe^{3+} ions being network-formers act similarly to Al^{3+} ions forming FeO_4 tetrahedra and suppressing $B^{III} \rightarrow B^{IV}$ conversion. However, since strength of Fe^{3+}—O bond is lower then that of Al—O bond, the effect of Fe_2O_3 on $B^{III} \rightarrow B^{IV}$ conversion is weaker. Molar concentration of Fe_2O_3 should be subtracted like Al_2O_3 in eq. (3) but with coefficient less than 1. Taking into account that energy of Fe^{3+}—O bond is lower than that of Al—O bond by ~3 times, this coefficient may be suggested to be ~3 as well. Therefore, in the numerator of the eq. (3) we have to subtract additionally $\sim0.3\times[Fe_2O_3]$. Thus in the presence of Fe_2O_3 the ψ_B values for the glasses studied are somewhat lower (Table I). At high concentrations in glasses Fe^{3+} ions may become network-modifiers with higher coordination number (CN=6) or form separate crystalline phase – hematite (Fe_2O_3) or spinel, especially in the presence of Fe^{2+} ions or different transition metal ions (Mn^{2+}, Ni^{2+}, Co^{2+}, Cu^{2+}, Zn^{2+}) as well as Mg^{2+} and Al^{3+} ions. Fe^{2+} ions, if present, are network-modifiers, but often form spinel type phase.

RESULTS AND DISCUSSION

Chemical composition and XRD patterns

All three glasses have similar Al_2O_3 target and actual contents. The glass 21-02 has the lowest B_2O_3 and highest Na_2O and SiO_2 contents. The glass 21-07 is high-B_2O_3 and low-Na_2O and SiO_2. The glass 21-21 has similar Na_2O and Li_2O molar concentrations and therefore appearance of mixed alkali effect may be expected in the most extent. All the glasses have comparable both weight and molar Fe_2O_3 concentrations. Although weight concentrations of Fe_2O_3 are rather high, their molar concentrations are not too high and XRD patterns of all three glasses demonstrate typical amorphous scattering with strong background at low angular range and "humps" in the vicinity of 30-32 degrees 2θ pointing to minor chemical ordering in glasses (Figure 1).

Optical Microscopy Images banded texture of the samples. Thee are different in quantitative ratios between transparent and opaque glasses. It should be noted occurrence of clear borders between differently colored glasses that may be due to different viscosity of melt layers with various content of iron oxides. No devitrification was observed.

As follows from optical microscopy image the sample 21-02 is predominantly composed of light transparent glass with a layer and small oval red-brown-colored area (Figure 2, left). The colored glass has layered texture appeared as the bands with red-brown and light-brown colorings. Light glass contains a lot of randomly distributed small gas bubbles up to 40 μm in diameter.

Thin section of the glass 21-07 is composed of non-uniformly, predominantly brown, colored glass with spots of light-brown and clear transparent glass. It was revealed at high magnifications that the coloring is du to the finest red-brown colored particles and the intensity of coloring is directly proportional to particles concentration.

Thin section of the glass 21-21 (Figure 2, right) is composed of banded glass with variable coloring of the bands. Major area is taken with the bands of transparent and red-brown colored glasses. Minor area of the thin section is filled with glasses with different coloring. The banded (layered) texture was probably formed during pouring of molten glasses onto a metal plate.

SEM photomicrographs demonstrate homogeneity of glasses at least at a level of ~50-100 nm (Figure 3). No phase separation has been found. Elemental concentrations by EDS data were obtained by scanning over areas 100 μm × 100 μm followed by recalculation to oxide concentrations (Tables II, III, and IV).

In the whole, there is a satisfactory agreement between the data obtained by ICP-AES and SEM/EDS taking into account that light elements (lighter than F) are not determined by EDS. Major elements are uniformly distributed over glass bulk whereas concentrations of some minor elements (S, Mn, Ni, Cu, Zn, Zr, Cd, Ba, La, Ce, Pb) vary markedly. Most of these elements are present in amounts not influencing on the structure of glass.

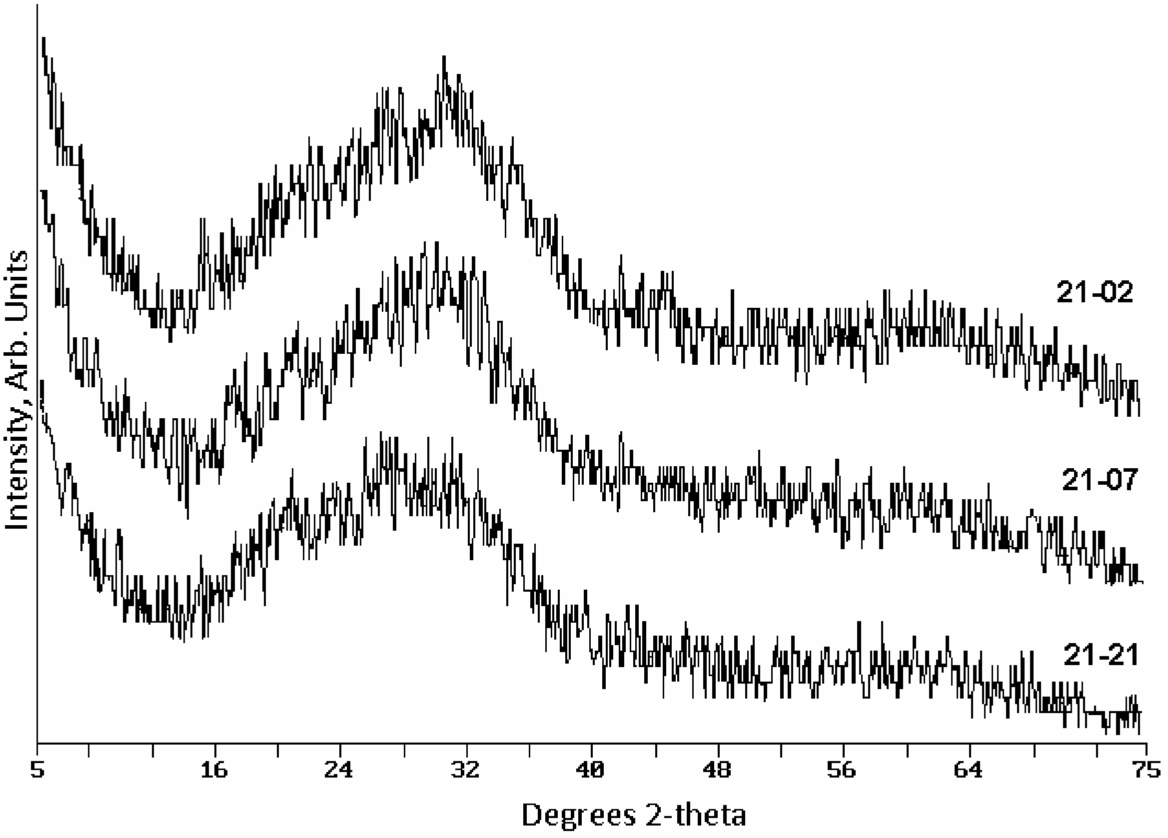

Figure 1. XRD Patterns of Samples in Series 21.

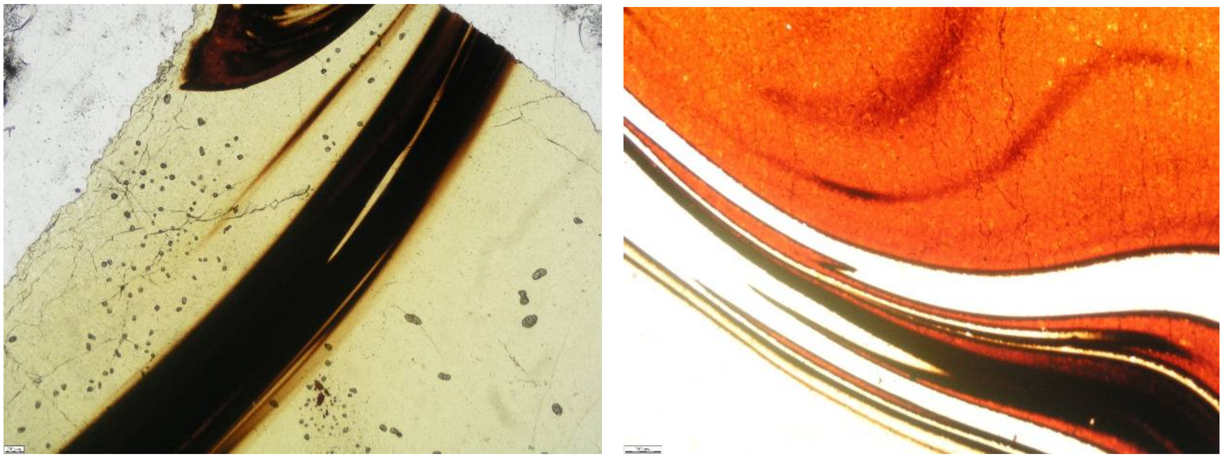

Figure 2. Optical Microscopy Images of Glasses 21-02 (left) and 21-21 (right).

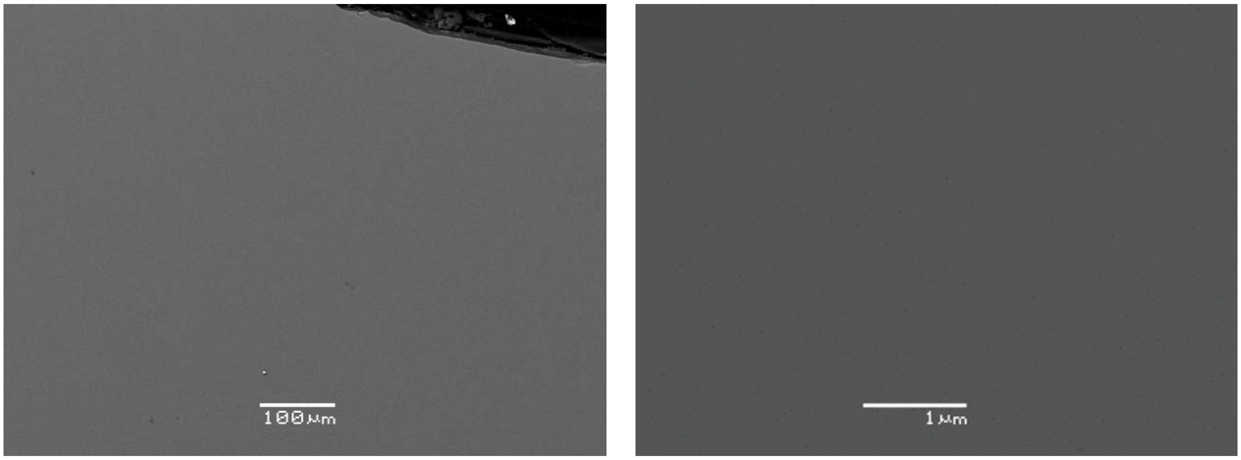

21-02

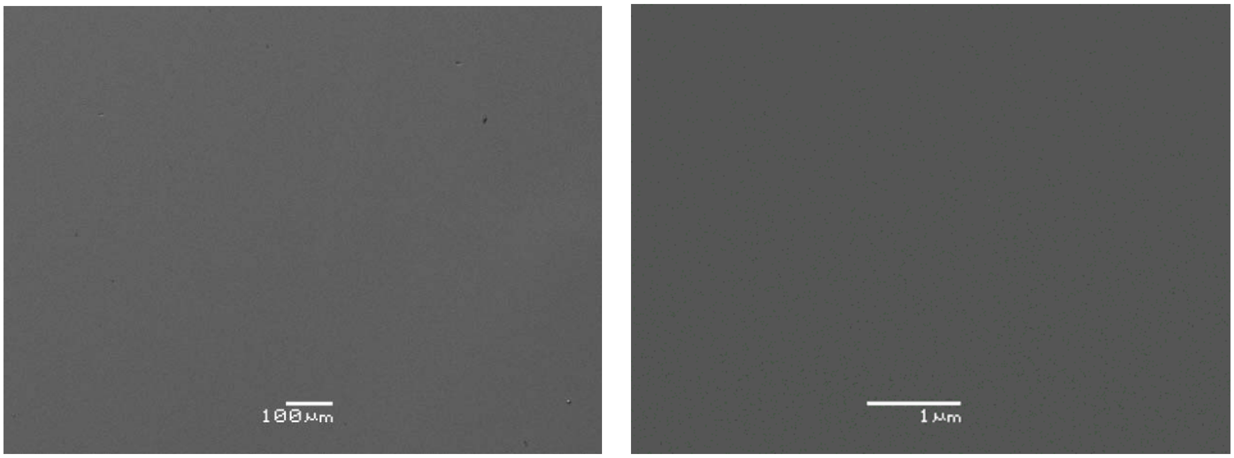

21-07

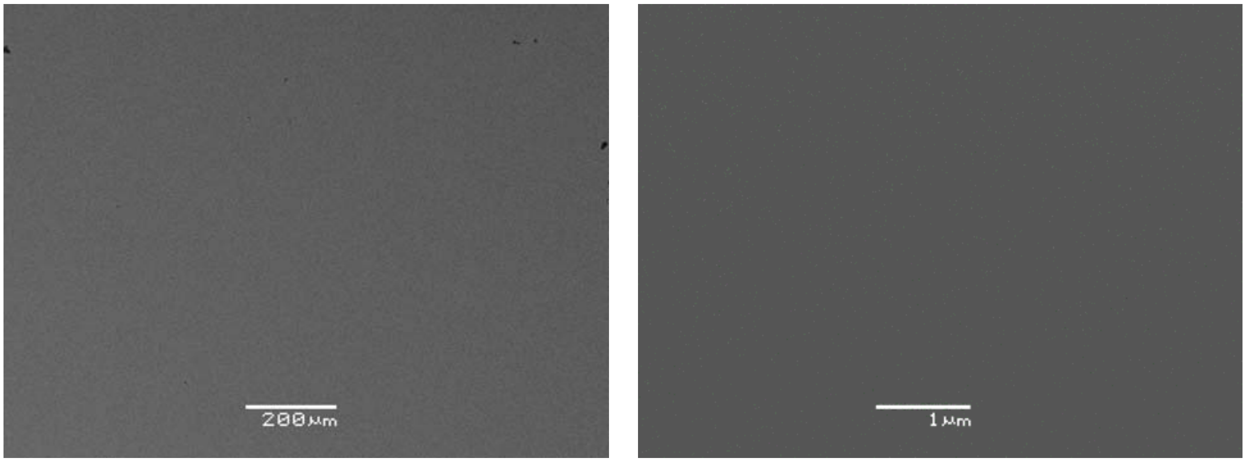

21-21

Figure 3. SEM Images of Samples in Series 21.

Table II. Chemical Composition of Sample 21-02.

Oxides	SEM/EDS data						Target comp.	ICP-AES
	Sigma %	Scan 1	Scan 2	Scan 3	Scan 4	Average		Actual
Na_2O	*0.40*	19.03	20.00	19.01	18.44	19.12	17.98	18.00
MgO	*0.13*	1.81	1.73	1.76	1.80	1.78	1.50	1.51
Al_2O_3	*0.13*	5.16	4.99	5.04	5.09	5.07	4.01	4.31
SiO_2	*0.23*	43.43	43.98	43.04	43.89	43.59	40.02	38.70
SO_3	*0.06*	0.58	0.38	0.50	0.27	0.43	0.48	0.55
TiO_2	*0.10*	2.33	2.10	1.98	2.13	2.14	2.00	1.97
MnO	*0.07*	0.31	0.31	0.17	0.39	0.30	0.30	0.40
Fe_2O_3	*0.21*	19.91	20.19	19.56	19.91	19.89	20.63	22.25
NiO	*0.07*	0.13	0.00	0.00	0.00	0.03	2.50	0.00
CuO	*0.09*	0.10	0.16	0.07	0.07	0.10	0.13	0.14
ZnO	*0.11*	0.18	0.29	0.00	0.18	0.16	0.13	0.13
ZrO_2	*0.19*	0.23	0.16	0.00	0.00	0.10	0.21	0.21
CdO	*0.12*	0.40	0.42	0.27	0.38	0.37	0.30	0.28
BaO	*0.21*	0.36	0.00	0.29	0.00	0.16	0.08	0.08
La_2O_3	*0.20*	0.00	0.00	0.13	0.23	0.09	0.10	0.09
Ce_2O_3	*0.16*	0.19	0.47	0.33	0.38	0.34	0.36	0.40
PbO	*0.24*	0.38	0.00	0.4	0.38	0.29	0.22	0.22
B_2O_3	ND	ND	ND	ND	ND	ND	5.07	5.30
Li_2O	ND	ND	ND	ND	ND	ND	4.00	3.99
Total	-	94.53	95.18	92.55	93.54	93.95	100.00	99.75

Table III. Chemical Composition of Sample 21-07.

Oxides	SEM/EDS				Target comp.	ICP-AES
	Scan 1	Scan 2	Scan 3	Average		Actual
Al_2O_3	5.80	6.14	5.61	5.85	4.87	5.07
B_2O_3	ND	ND	ND	ND	13.92	13.75
CaO	4.31	4.12	4.15	4.19	3.92	3.98
Fe_2O_3	16.44	16.33	16.59	16.45	17.98	17.85
Li_2O	ND	ND	ND	ND	4.00	3.89
MgO	1.37	1.77	1.89	1.68	1.50	1.47
MnO	5.49	5.71	5.45	5.56	5.50	5.34
Na_2O	13.51	13.62	12.99	13.37	12.71	12.50
SiO_2	36.15	36.05	35.65	35.95	33.60	32.20
TiO_2	2.14	2.05	2.30	2.16	2.00	1.90
Total	85.21	85.79	84.63	85.21	100.00	99.18

Table IV. Chemical Composition of Sample 21-21.

Oxides	SEM/EDS					Target comp.	ICP-AES
	Sigma %	Scan 1	Scan 2	Scan 3	Average		Actual
Na_2O	*0.37*	15.54	15.31	15.85	15.57	14.67	13.65
Al_2O_3	*0.14*	6.33	6.21	6.35	6.30	4.86	4.75
SiO_2	*0.23*	43.73	42.66	43.07	43.15	39.31	36.20
SO_3 /SO_4	*0.06*	0.37	0.57	0.40	0.45	0.48	0.53
TiO_2	*0.09*	1.90	2.00	1.82	1.91	2.01	1.84
MnO	*0.08*	1.03	0.89	1.04	0.99	1.00	1.23
Fe_2O_3	*0.20*	18.45	18.85	18.69	18.66	19.95	23.40
CuO	*0.09*	0.00	0.00	0.12	0.04	0.13	0.13
ZnO	*0.11*	0.24	0.18	0.26	0.23	0.13	0.12
ZrO_2	*0.20*	0.26	0.20	0.35	0.27	0.21	0.19
CdO	*0.12*	0.09	0.18	0.31	0.19	0.30	0.27
BaO	*0.20*	0.31	0.14	0.30	0.25	0.01	0.07
La_2O_3	*0.19*	0.6	0.24	0.00	0.28	0.10	0.08
Ce_2O_3	*0.15*	0.48	0.15	0.00	0.21	0.36	0.38
PbO	*0.24*	0.35	0.18	0.00	0.18	0.22	0.21
B_2O_3	ND	ND	ND	ND	ND	9.01	8.78
Li_2O	ND	ND	ND	ND	ND	7.00	6.63
Total	-	89.68	87.76	88.56	88.67	100.00	99.80

Effect of etching on the structure of the surface of glasses

The polished surfaces of the samples 21-02, 21-07 and 21-21 were etched with 0.1M HCl for 1 day and studied by SEM/EDS. General view of the samples is shown on Figure 4.

Surface of the glasses after etching is coated with a mesh of micron-sized cracks (Figures 5-7). As follows from SEM/EDS data (Table V), the rim is strongly depleted with Na_2O and enriched with SiO_2 i.e. this is a typical surface layer remaining on the surface of glass after leaching. Chemical composition of the core is similar to that of the bulk of unaltered glass. No phase separation was found.

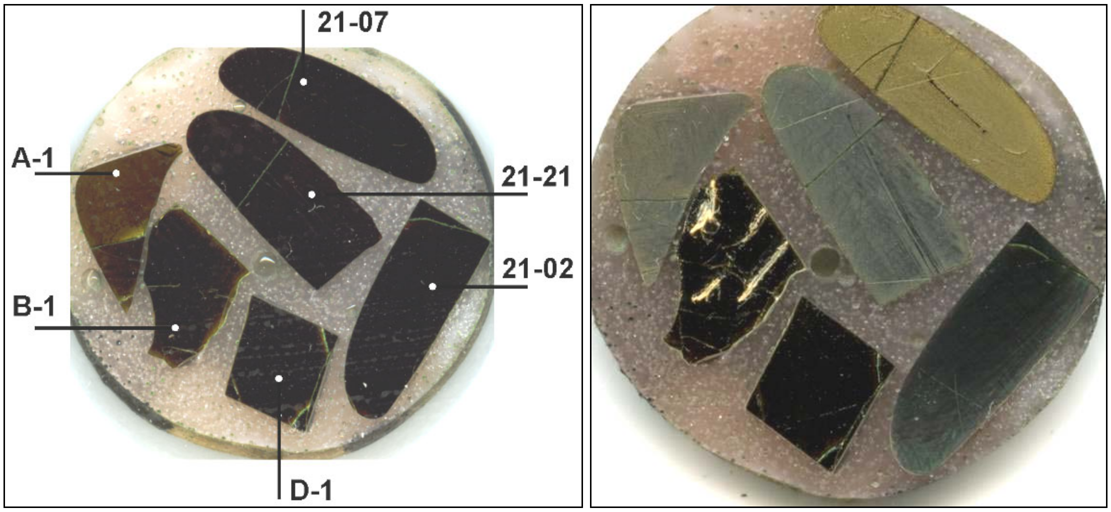

Figure 4. View of the samples before (left) and after etching (right).
Glasses A1, B1 and D1 will be described in a separate report.

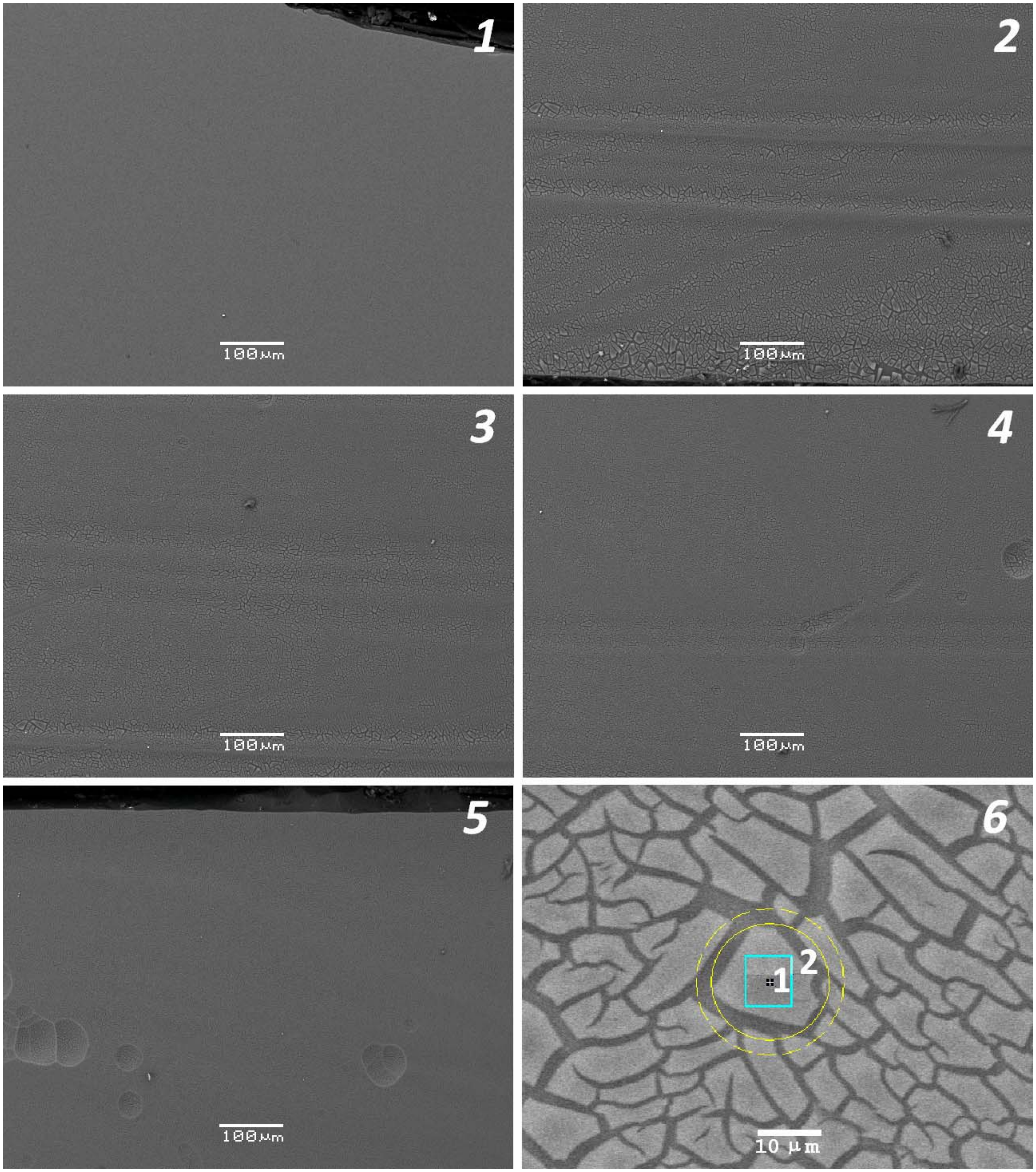

Figure 5. BSE SEM images of the surface of the glass 21-02 before (1) and after (2-5) etching in 0.1 M HCl.

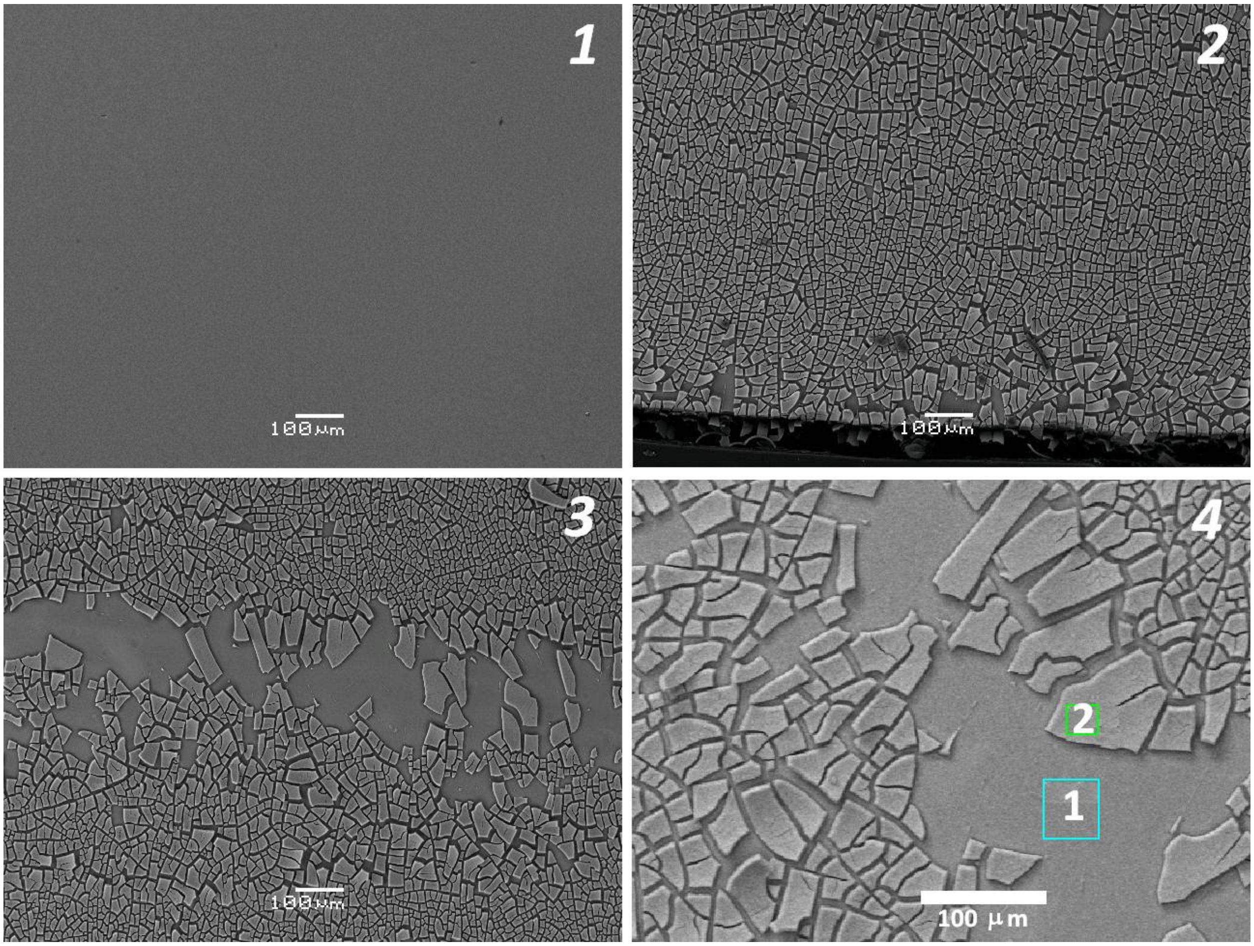

Figure 6. BSE SEM Image of the surface of the glass 21-07 before (1) and after (2-4) etching in 0.1 M HCl.

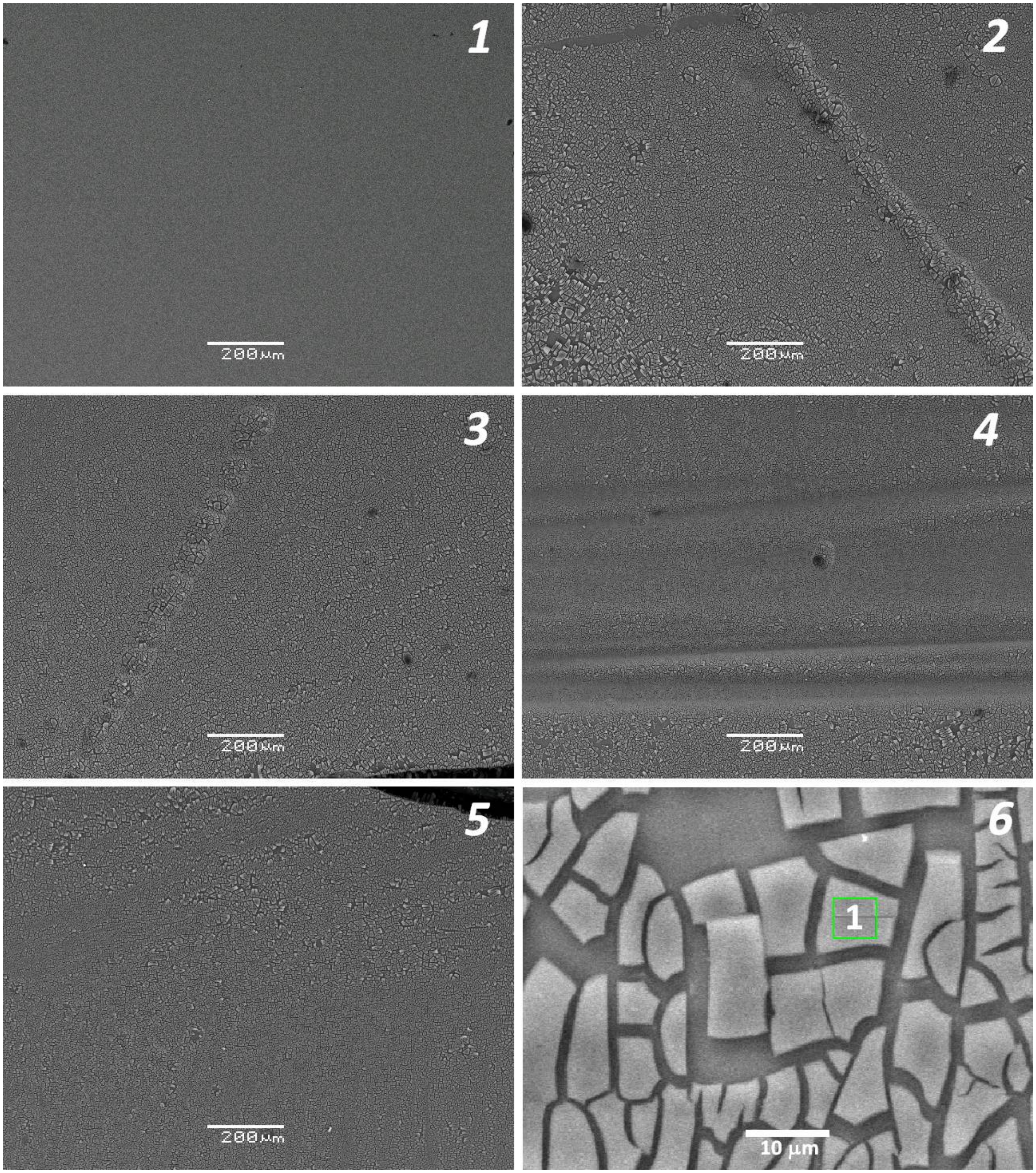

Figure 7. BSE SEM Image of the surface of the glass 21-21 before (1) and after (2-6) etching in 0.1 M HCl.

Table V. Chemical composition by EDS of various areas on the surfaces of etched glasses.

Oxides	21-02			21-07			21-21	
	1 (rim)	2 (rim+core)	Glass*	1 (core)	2 (rim)	Glass*	1 (rim)	Glass*
Na_2O	7.93	6.56	18.00	11.35	0.47	12.50	2.43	13.65
MgO	1.23	1.26	1.51	1.63	0.34	1.47	-	-
Al_2O_3	3.34	3.47	4.31	5.09	0.54	5.07	2.52	4.75
SiO_2	40.71	40.39	38.70	32.93	35.78	32.20	36.29	36.20
CaO	0.74	0.92	0.02	3.8	3.64	3.98	-	0.02
TiO_2	3.96	3.81	1.97	1.95	5.61	1.90	4.14	1.84
MnO	0.33	0.36	0.40	5.06	0.15	5.34	0.69	1.23
Fe_2O_3	18.62	19.64	22.25	19.72	32.56	17.85	18.69	23.40
NiO	0.10	-	-	-	-	-	-	
ZnO	1.24	1.64	0.13	-	1.98	-	2.29	0.12
ZrO_2	0.23	0.24	0.21	-	-	-	-	0.19
BaO	0.20	0.39	0.08	-	-	-	0.65	0.07
PbO	0.75	0.48	0.22	-	-	-	0.32	0.21
Sum	79.38	79.16	87.80	81.53	81.07	80.31	68.02	81.68
Li_2O	nd	nd	3.99	nd	nd	3.89	nd	6.63
B_2O_3	nd	nd	5.30	nd	nd	13.75	nd	8.78
Total			97.09			97.95		97.09

* actual concentration in glass measured by ICP-OES.

FTIR and Raman spectra

IR spectra within the range of 4000-400 cm^{-1} (Figure 8) are composed of bands within the range of 3600-3200 cm^{-1} and 1650-1600 cm^{-1} due to stretching and bending modes in molecules of absorbed and structurally bound water and hydroxyl groups [10], weak bands at 2950-2800 cm^{-1} due to oscillations of hydrogen bonds and bonds located lower than 1600 cm^{-1} due to oscillations of bonds forming anionic motif of the structure of glasses. This range is considered in more details (Figure 9). The spectra within the range of 600-30 cm^{-1} were recorded separately (Figure 9).

As follows from chemical composition of glasses (Table I) the glass 21-07 has the lowest concentrations of SiO_2 and Na_2O and the highest fraction of trigonally coordinated boron among all three glasses studied. IR spectrum of this sample has strong absorption at 1350-1500 cm^{-1} whereas absorption within the same range in the spectra of sample 21-21 and 21-02 is weaker. The wavenumber ranges of 1500-1300 cm^{-1} and ~1260-1270 cm^{-1} are typical of oscillations in the boron-oxygen groups with trigonally coordinated boron (boron-oxygen triangles BO_3) [11]. In Raman spectra (Figure 6) a weak band is observed at 1250-1450 cm^{-1}. Its intensity decreases with the increase of the ψ_B value and becomes negligible in the spectrum of glass 21-02 with the highest ψ_B value. These bands were attributed as components of twice degenerated asymmetric valence ν_3 O−B−O vibrations (stretching modes). The band with components ~710-730 and 650-670 cm^{-1} may be associated with twice degenerated asymmetric deformation δ (ν_4) O−B−O vibration (bending modes) [11]. Valence ν_1 O−B−O vibrations at ~805-810 cm^{-1} are inactive in IR spectra [10] but may be observable if symmetry decreases. In our spectrum this band is very weak but clearly appeared. The shoulder at ~520 cm^{-1} and the band with a maximum at ~470-475 cm^{-1} are components of symmetric deformation δ (ν_2) O−B−O vibration. Their appearance exhibits distortion of BO_3 units linked in network.

Strong absorption in both IR and Raman spectra within the range of 1150-850 cm^{-1} is caused by asymmetric ν_3 vibrations in silicon-oxygen units bonded to zero (850-900 cm^{-1}), one (~900-950 cm^{-1}), two (~950-1050 cm^{-1}), three (~1050-1130 cm^{-1}) and four (~1130-1200 cm^{-1}) neighboring SiO_4 tetrahedra (Q^0, Q^1, Q^2, Q^3, Q^4, respectively) [12] and, in less extent, BO_4 tetrahedra (1000-1100 cm^{-1}) [11]. In IR spectra of all the glasses the broad band within the range of ~800-1200 cm^{-1} is multicomponent due to superposition of oscillations in SiO_4 and BO_4 tetrahedra. The strongest absorption takes place within the range of 980-1150 cm^{-1}. Absorption within the range of ~800-980 cm^{-1} is the strongest in the spectrum of glass 21-07 and the lowest – in the spectrum of glass 21-02 that is consistent with variation of silica content in glass and ψ_B value, i.e. relation of intensities of these two bands is changed in favor of higher wavenumber band with increasing of ψ_B value. This may be accounted for increase of fraction of four-coordinated boron (absorption at 1000-1100 cm^{-1}), in particular, increase of the number of bridging Si—O—B bonds linking SiO_4 and BO_4 tetrahedra in common network. At that, the number of Q^0 and Q^1 tetrahedra decreases and glass network renders higher degree of connectedness (polymerization).

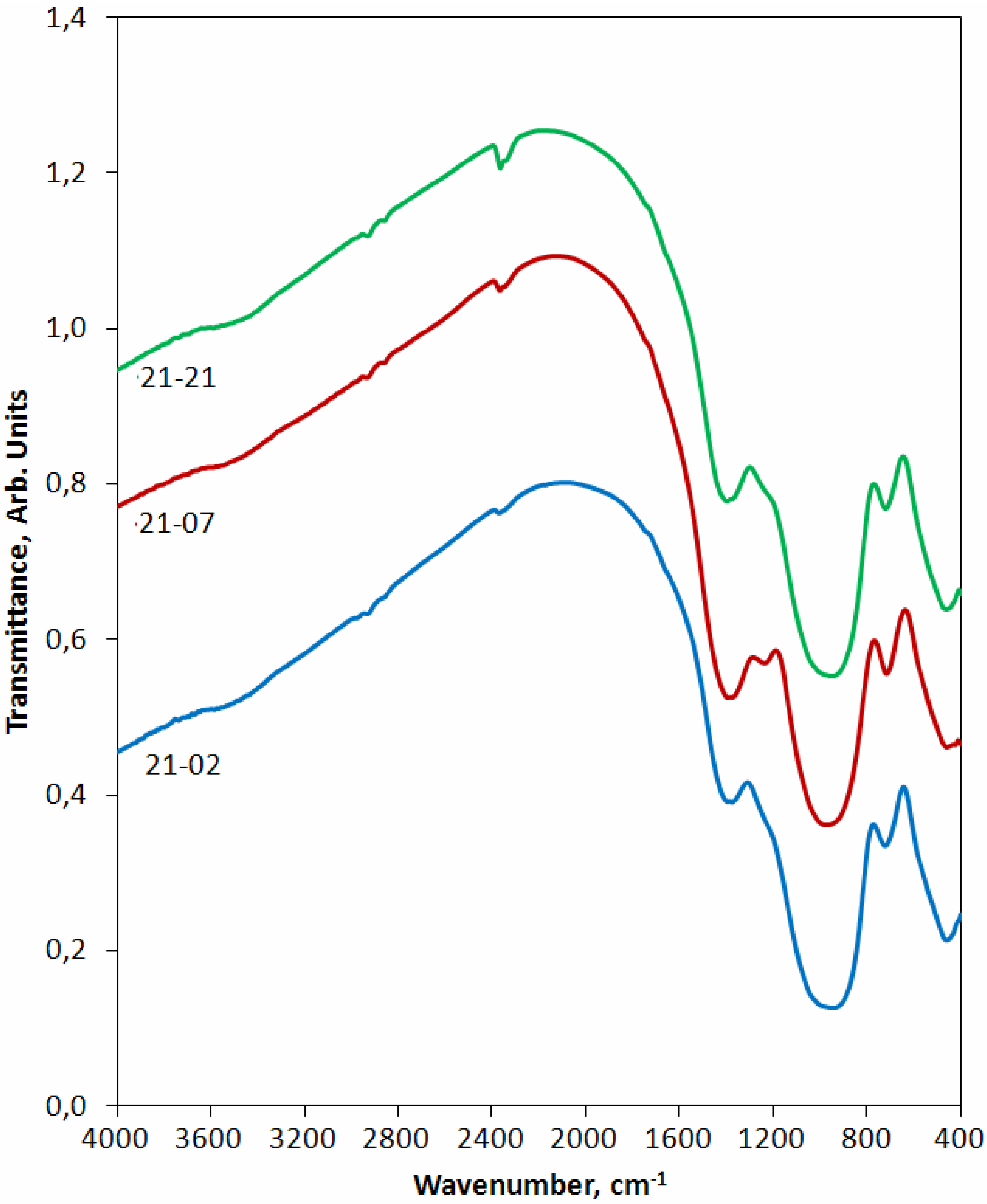

Figure 8. IR spectra of Glasses in Series 21.

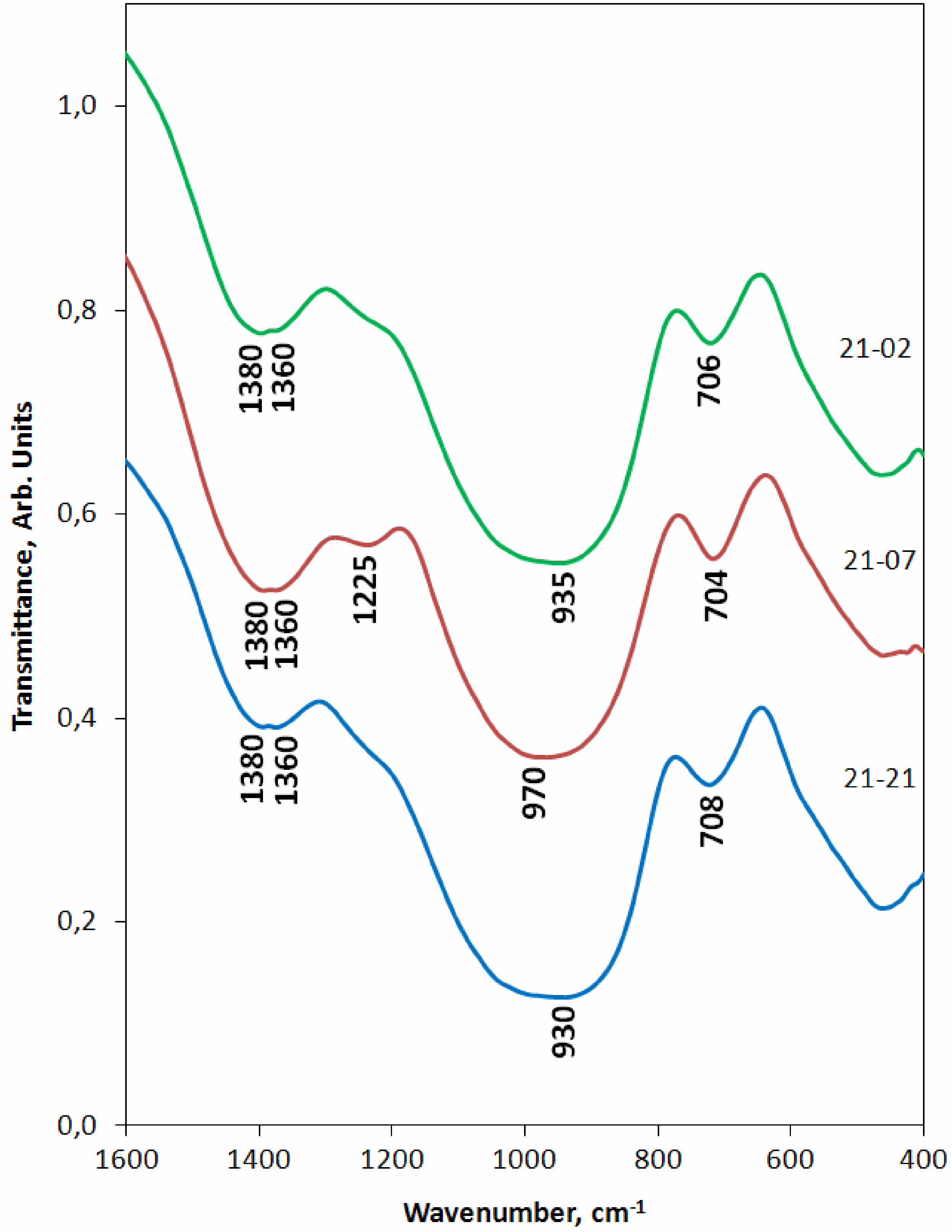

Figure 9. Fragments of IR Spectra of glasses in series 21 within the range of 400-1600 cm^{-1}.

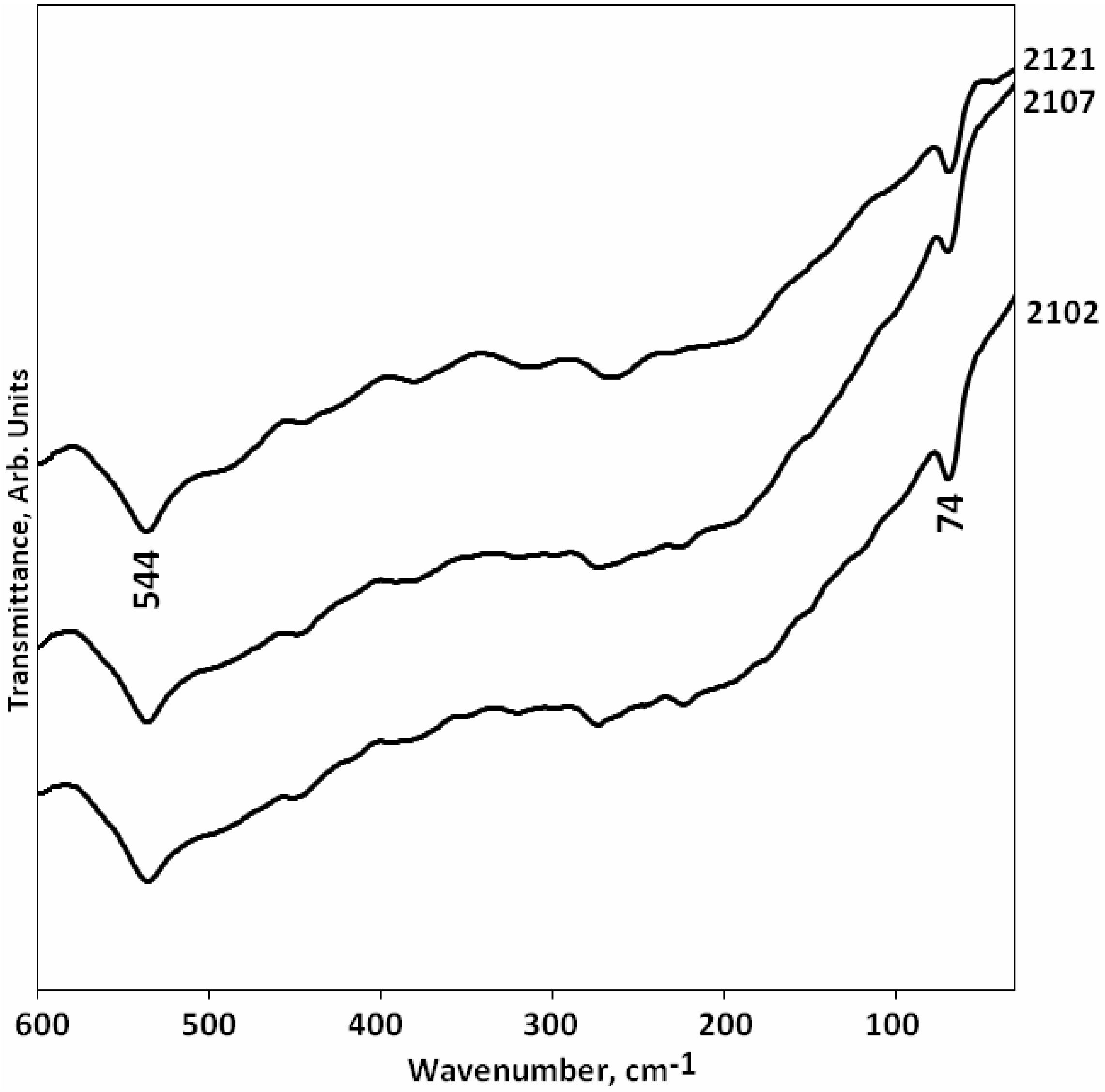

Figure 10. IR spectra of glasses in series 21 within the range of 30-600 cm^{-1}.

IR spectra of the glasses heat-treated at 500 °C for 10 hrs were also recorded (Figures 11 and 12). They consist of the bands in same ranges as spectra of initial glasses but most of the bands are split due to structural ordering in the glass network pointing to chemical differentiating and running of pre-crystallization processes.

As follows from comparison of Figures 8 and 11, heat-treatment decrease markedly chemical durability of glasses. Such conclusion may be done on the basis of much higher intensity in the spectra of heat-treated glasses of the bands within high-wavenumber range due to vibrations in molecules of structurally bound or/and absorbed water or in hydroxyl groups (3600-3200 cm^{-1} and 1700-1600 cm^{-1}) and hydrogen bonds (3000-2800 cm^{-1}).

In Raman spectra (Figure 13) a strong asymmetric band within the range of 850-1150 cm^{-1} is a superposition of the bands due to stretching modes in BO_4 and SiO_4 tetrahedra with various number of bridging oxygen ions and Si—O—B bridges linking SiO_4 and BO_4 tetrahedra. The band at 400-550 cm^{-1} in both Raman and IR spectra is due to bending modes in SiO_4 tetrahedra [10,11]. Major changes in Raman spectra of glasses with increase of the ψ_B value are separation and growth in intensity of the band with a maximum at ~980 cm^{-1}, shift of maximum of the band due to stretching modes from ~935 to ~900 cm^{-1} and growth in intensity the band within the range of 700-800 cm^{-1}.

Computer simulation of Raman spectra (Figure 14) shows differences in the structure of the glasses. The strongest responses within the ranges of 300-600 and 800-1200 cm^{-1} due to bending and stretching modes of Si—O—Si bonds are normally superpositions of at least two bands due to SiO_4 units with various number of bridging oxygen ions. The glass 21-02 has the highest alkali oxides content among all the glasses studied (Table I). Positions of major peaks at 894 and 989 cm^{-1} demonstrate that the glass network is built from pyro-groups [Si_2O_7] and short chains of metasilicate [SiO_3] groups. The component with a maximum at ~748 cm^{-1} is stronger than it can be expected for so low alumina content (~3 mol.%). This band can be suggested to have minor contribution due to response of BO_4 tetrahedra. Weak band with a maximum at ~1320 cm^{-1} is due to BO_3 triangles.

Similar simulation was made for the Raman spectrum of the glass 21-07 (Figure 14). Positions of the maxima at 924 and 1028 cm^{-1} point to higher degree of connectedness of the silicon-oxygen network in the structure of this glass as compared to that in the structure of previous glass 21-02. This is some surprisingly because silica content in this glass is lower (~38 mol.%) than in the glass 21-02. At the same time sum of alkali oxides is also lower. One more explanation may be given in suggestion that this glass has a tendency to phase separation and its structure is composed of high-silica and high-alkali/boron areas of chemical differentiation being anteceding liquid-liquid phase separation. This suggestion is supported by a shift of the maximum of the band due to trigonally coordinated boron to 1362 cm^{-1} that points to higher degree of polymerization of BO_3 units.

A set of simulated lines is similar to those in the Raman spectra of the glasses 21-02 and 21-07 and is intermediate between them. Values of maxima of the components at 893 and 975 cm^{-1} are close to those in the spectrum of the glass 21-02 but the intensity of the higher wavenumber component in the spectrum of the glass 21-21 is much higher than in the spectrum of the glass 21-02. This shows higher degree of connectedness of the silica-oxygen network in the structure of the glass 21-21 than that in the glass 21-02. Thus, the network of the glass 21-21 is mainly built from metasilicate chains and/or circular structures of SiO_4 tetrahedra with preferably two bridging oxygen ions. Position of maximum of the band due to BO_3 units is also intermediate between those in the spectra of glasses 21-02 and 21-07.

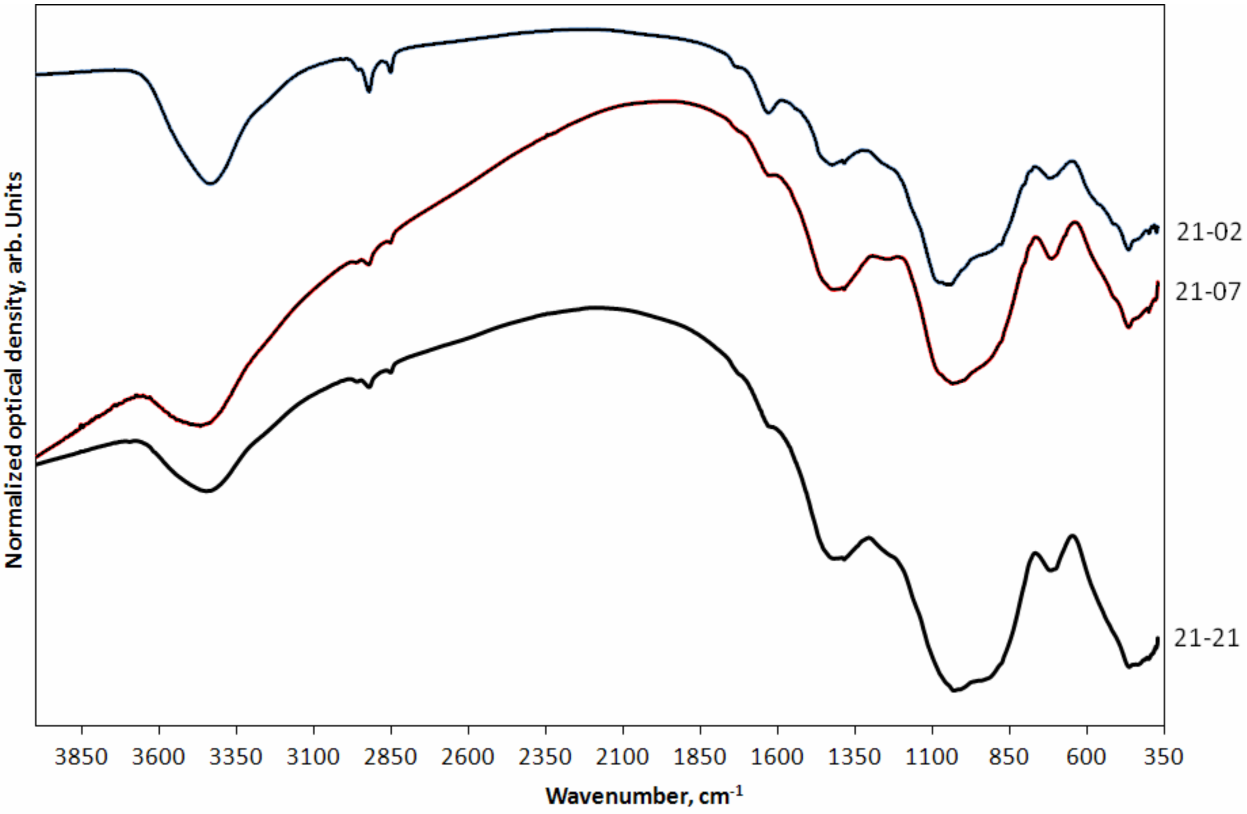

Figure 11. IR spectra of Glasses in Series 21 Heat-Treated at 500 °C.

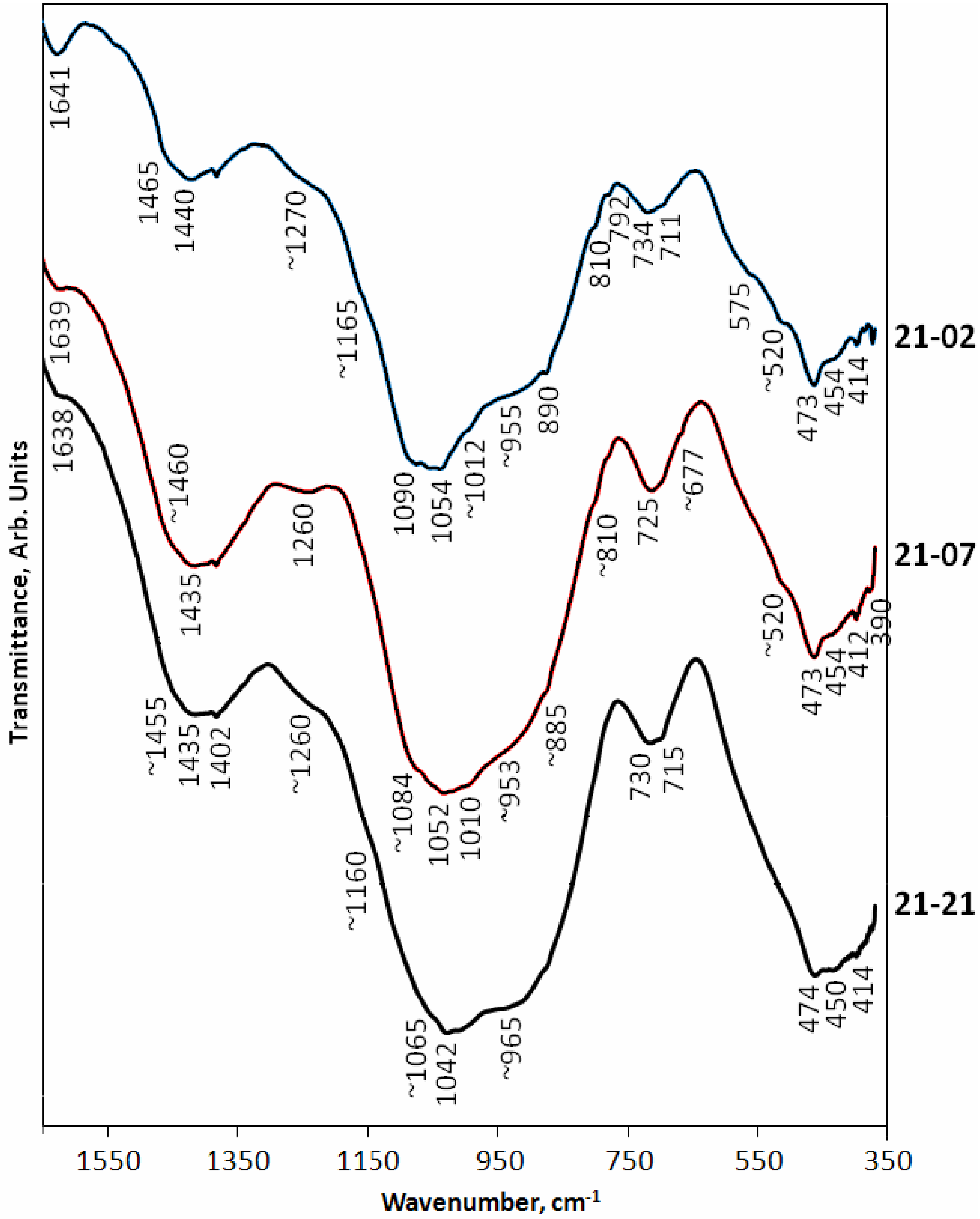

Figure 12. Fragments of IR spectra within the Range of 1600-350 cm^{-1} of Glasses in Series 21 Heat-Treated at 500 °C.

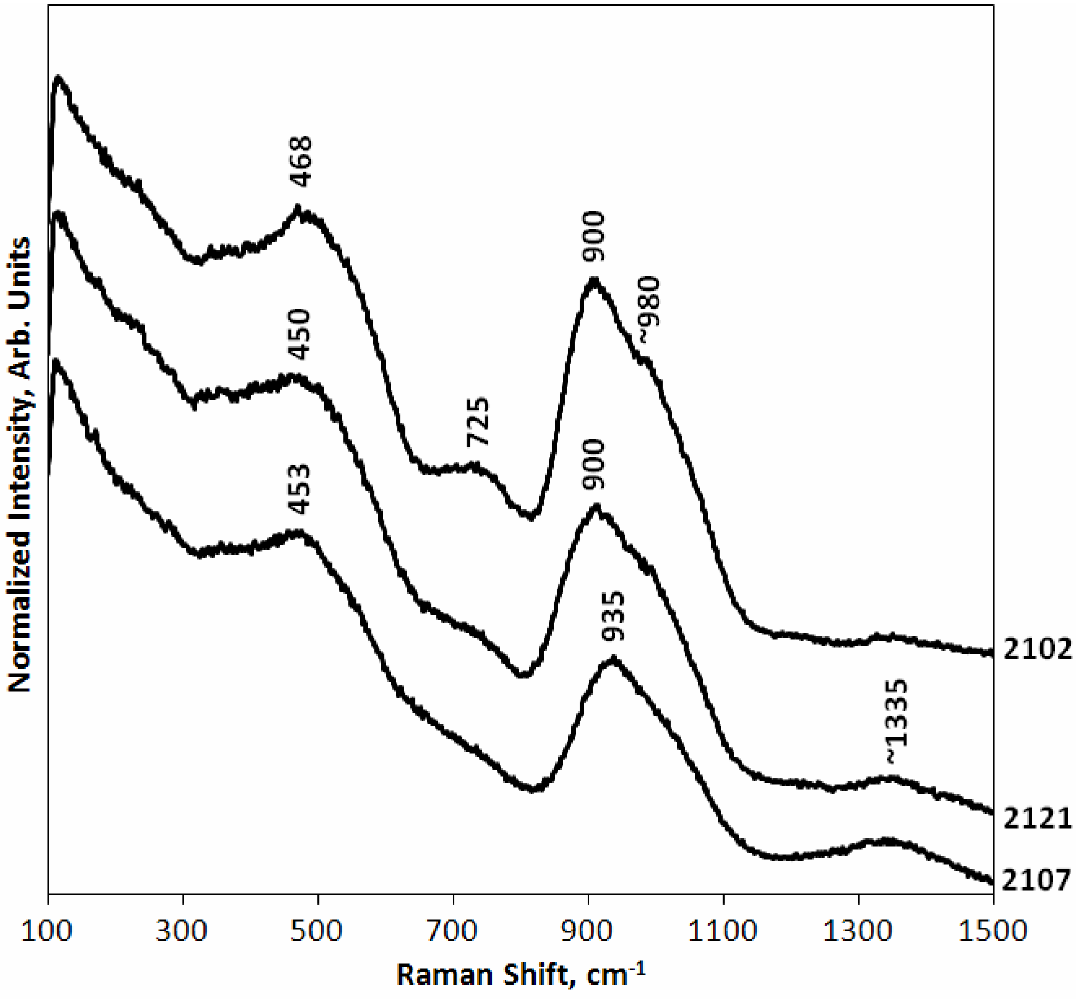

Figure 13. Raman spectra of glasses in series 21.

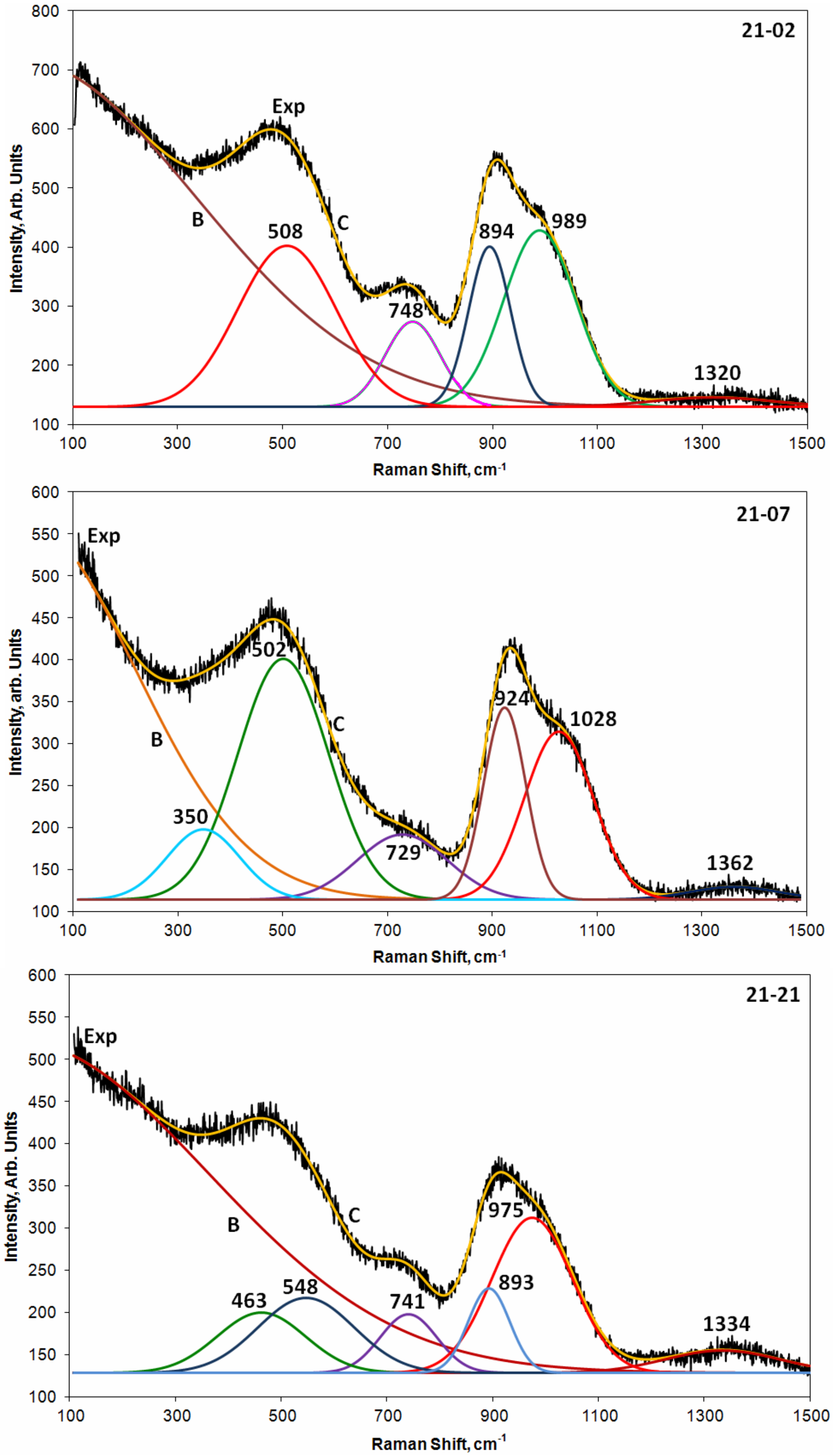

Figure 14. Computer simulation of Raman spectra of the glasses 21-02, 21-07 and 21-21. B – baseline, C – calculated, Exp – experimental.

Similar behavior of the bands with a maximum at ~980 and ~725 cm^{-1} allows to assigning them respectively to asymmetric (ν_3) and symmetric (ν_1) stretching modes in SiO_4 tetrahedra with two bridging oxygen ions (C_{2v} symmetry). In the whole the band with a maximum at ~935 cm^{-1} is split into two components with maxima at ~900 and ~980 cm^{-1} due to overall decrease in symmetry of SiO_4 units probably because of formation of Si—O—B bridges linking SiO_4 and BO_4 tetrahedra in common network. However relatively low B_2O_3 concentration in glass 21-21 and particularly 21-02 suggests that the effect of these bonds is rather minor because amount of BO_4 tetrahedra is insufficient to fix all the alkali ions at these tetrahedral for suppression of their leaching.

Absorption within the range of 600-800 cm^{-1} may contain contribution due to Al—O stretching modes in the AlO_4 tetrahedra [10]. Taking into account low Al_2O_3 content in glasses, it may be expected that major Al is four-coordinated. However due to this reason the contribution due to Al—O oscillating modes in this band should be minor.

The wavenumber range lower 600 cm^{-1} is of interest due to possible appearance of Fe—O stretching modes in this range [10,13]. Figure 4 demonstrates strong absorption within the range of 350-600 cm^{-1}. Major contribution to this band is made by bending modes in the SiO_4 tetrahedra because SiO_2 concentration in glasses is much higher than concentrations of different oxides. This band has a number of components mainly due to de-degeneration of bending modes at lowering the symmetry of SiO_4 tetrahedra. Nevertheless, there are some additional bands (575, 520 cm^{-1} and at lower wavenumbers) which may be assigned to Fe^{IV}—O stretching modes in FeO_4 tetrahedral units which are normally appeared within this wavenumber range [14]. Fe^{VI}—O stretching modes in FeO_6 octahedra are positioned at lower wavenumber range (300-500 cm^{-1}) [13].

Low wavenumber IR (Figure 10) and Raman (Figure 13) spectra involve strong bands with maxima at 544 and 450-470 cm^{-1} and numerous weaker bands due to bending modes in distorted SiO_4 tetrahedra and possibly stretching modes in FeO_4 tetrahedra. Some weak lines within the range of 200-400 cm^{-1} may be attributed as stretching modes in FeO_6 octahedra, but as follows from very low intensity of these bands the number of such octahedra is negligible.

Iron valence and environment in glasses

Fe K edge X-ray absorption spectra are shown on Figure 15. Fe K edge XANES spectra (Figure 16) are typical of trivalent iron (Fe^{3+} ions) in tetrahedral oxygen environment [14,15] but minor fraction of divalent iron may be also present in samples 21-07 and 21-21. This is also see from the first derivatives of XANES spectra (Figure 17) where positions of components of major peak due to Fe ions in 21-07 and 21-21 glasses are similar but some different from those for 21-02 glass.

FT of Fe K edge EXAFS in glasses demonstrate minor second coordination cell of Fe ions in all the glasses (Figure 18). The second cell is the weakest in glass 21-02. The first coordination cell in all the glasses is split into two components. Computer simulation (Table VI) indicates two Fe—O distances – shorter at ~1.72 Å and longer at ~1.90 Å in the structure of glasses 21-02 and 21-07 and slightly longer distances in the structure of glass 21-21: ~1.76 and ~1.94 Å, respectively. These values are similar to those measured earlier in various silicate and borosilicate glasses including nuclear waste glasses [16-21].

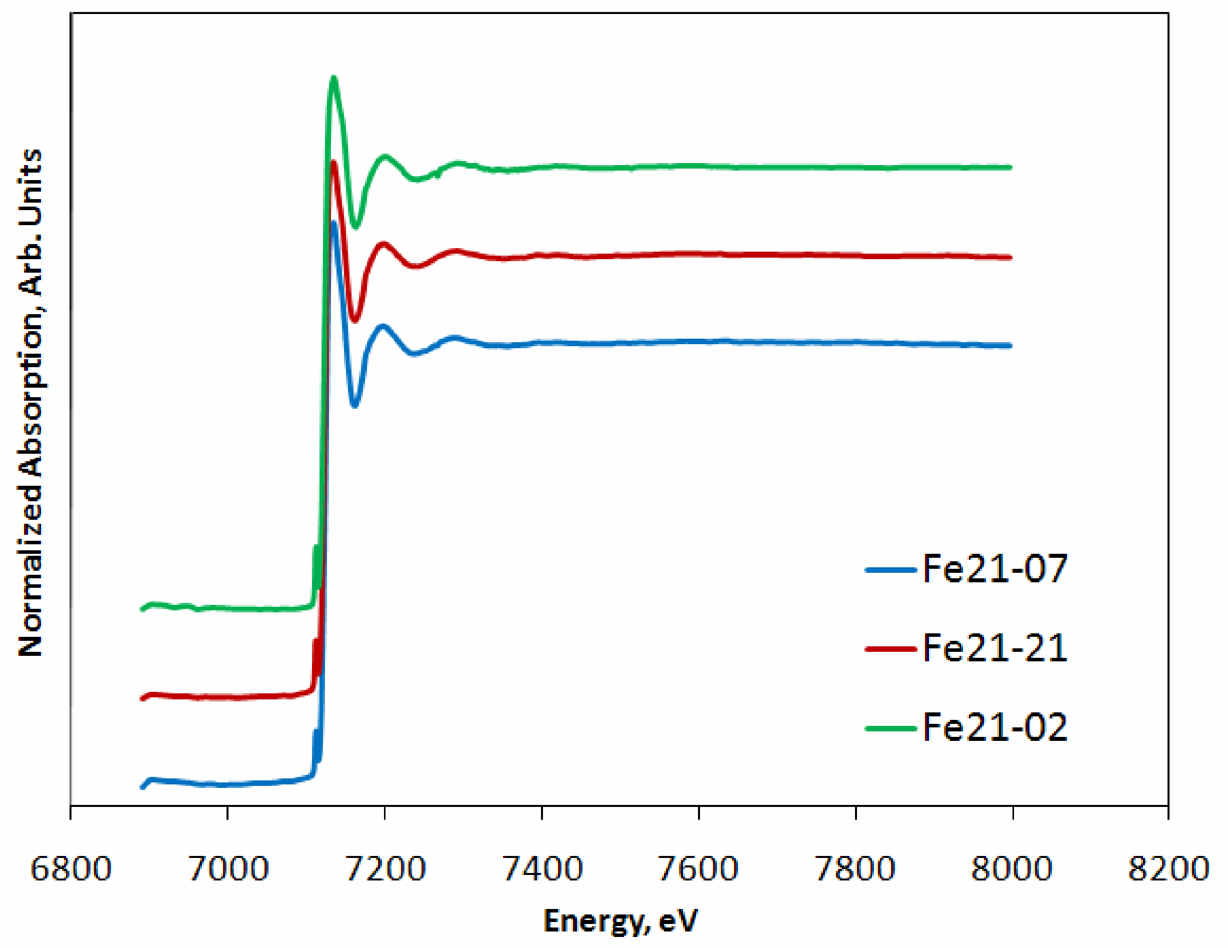

Figure 15. XAFS spectra of Fe K edge of glasses in series 21.

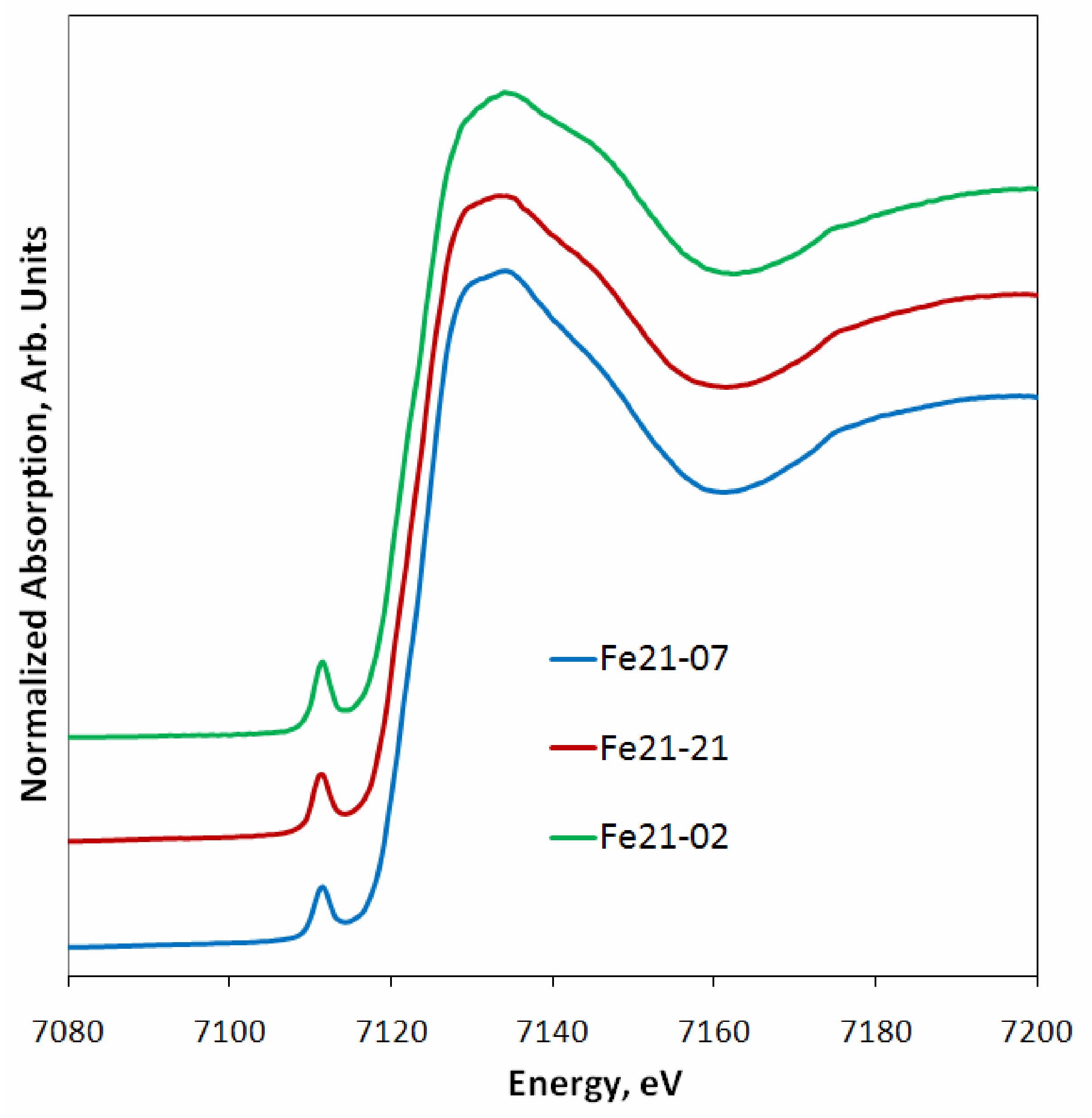

Figure 16. XANES spectra of Fe K edge of glasses in series 21.

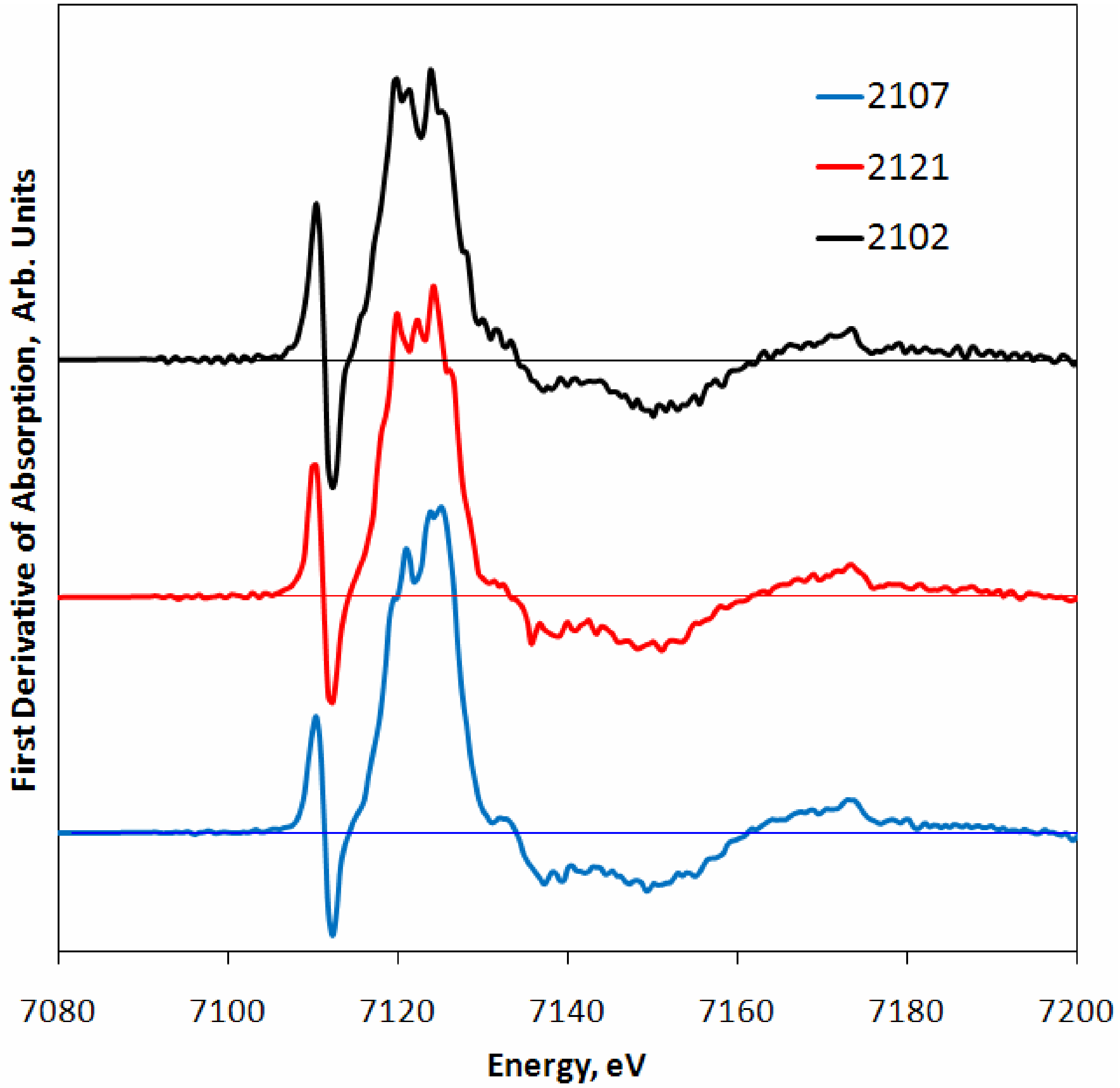

Figure 17. Differential XANES spectra of Fe K edge of glasses in series 21.

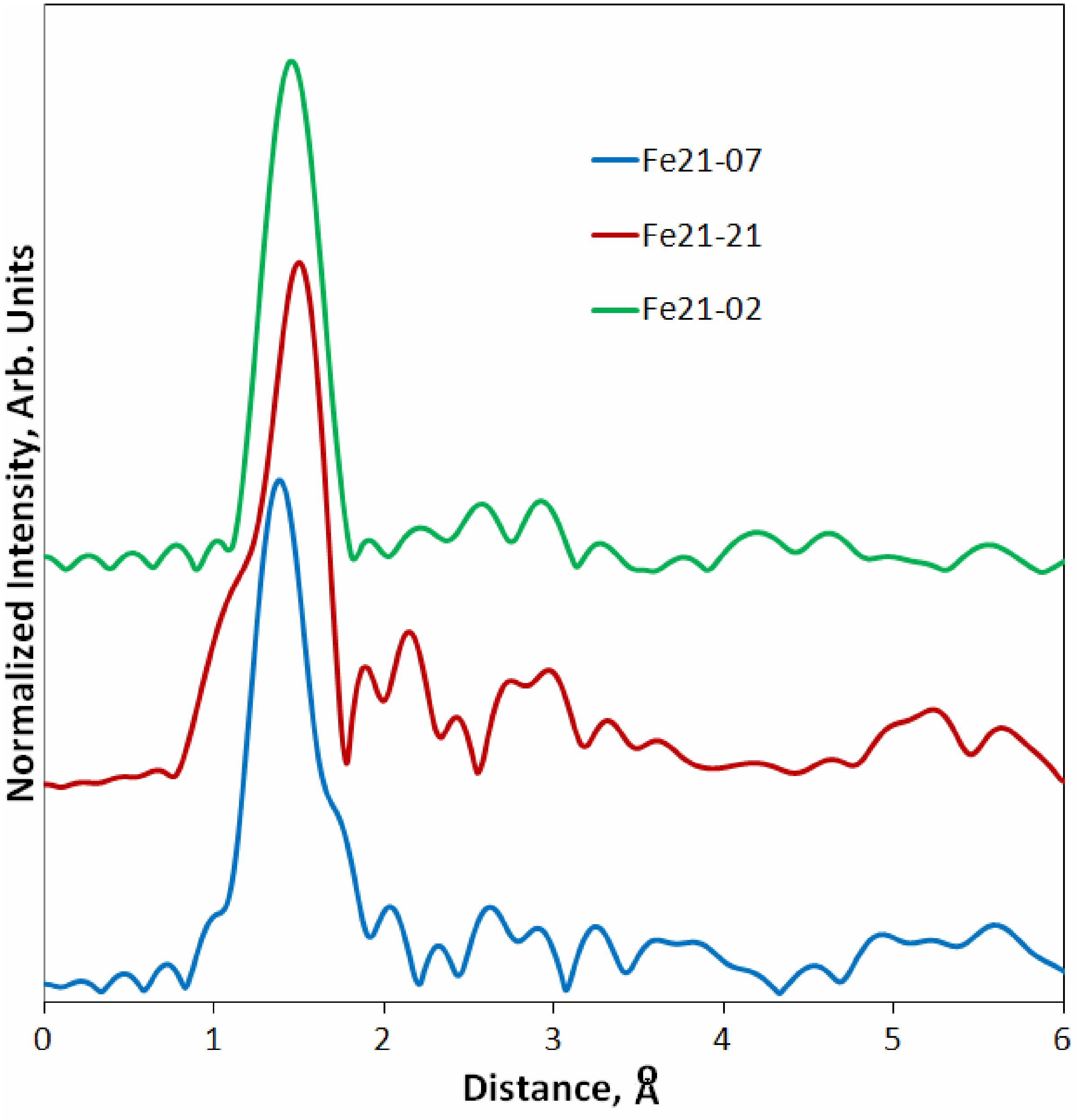

Figure 18. FT EXAFS of Fe K edge of glasses in series 21.

No phase shift correction.

Table VI. Fitting of the Fe K Edge EXAFS Spectra of Glasses in Series 21.

Glass	2102		2107		2121	
Bond	CN	R—O, Å	CN	R—O, Å	CN	R—O, Å
Fe-O1	1.84±0.09	1.72±0.01	1.41	1.72±0.01	1.82	1.76±0.01
Fe-O2	2.13±0.13	1.90±0.01	2.59	1.90±0.01	2.18	1.94±0.01
Fe-O3(Me)	~1	3.64±0.05	~1.3	3.22±0.04	~1.48	3.25±0.04

In the structure of all the glasses coordination number of Fe on oxygen is 4 or nearly 4 and Fe ions are located in distorted tetrahedral environment (Table VI). In the glasses 21-02 and 21-21 FeO_4 tetrahedra experience rhombic distortion (symmetry C_{2v}) whereas distortion of FeO_4 tetrahedra in the structure of glass 21-07 is closer to axial (symmetry C_{3v}).

The second coordination cell of Fe ions is not clearly expressed indicating their rather homogeneous distribution (Figure 19). In the most "disordered" glass 21-02 the nearest neighboring ion of either oxygen or heavier element is positioned at a distance of ~3.64 Å with average CN ≈ 1. In more "ordered" glasses 21-07 and 21-21 the nearest Fe ion neighbor is located at a distance of 3.22-3.25 Å with CN = 1.3÷1.5.

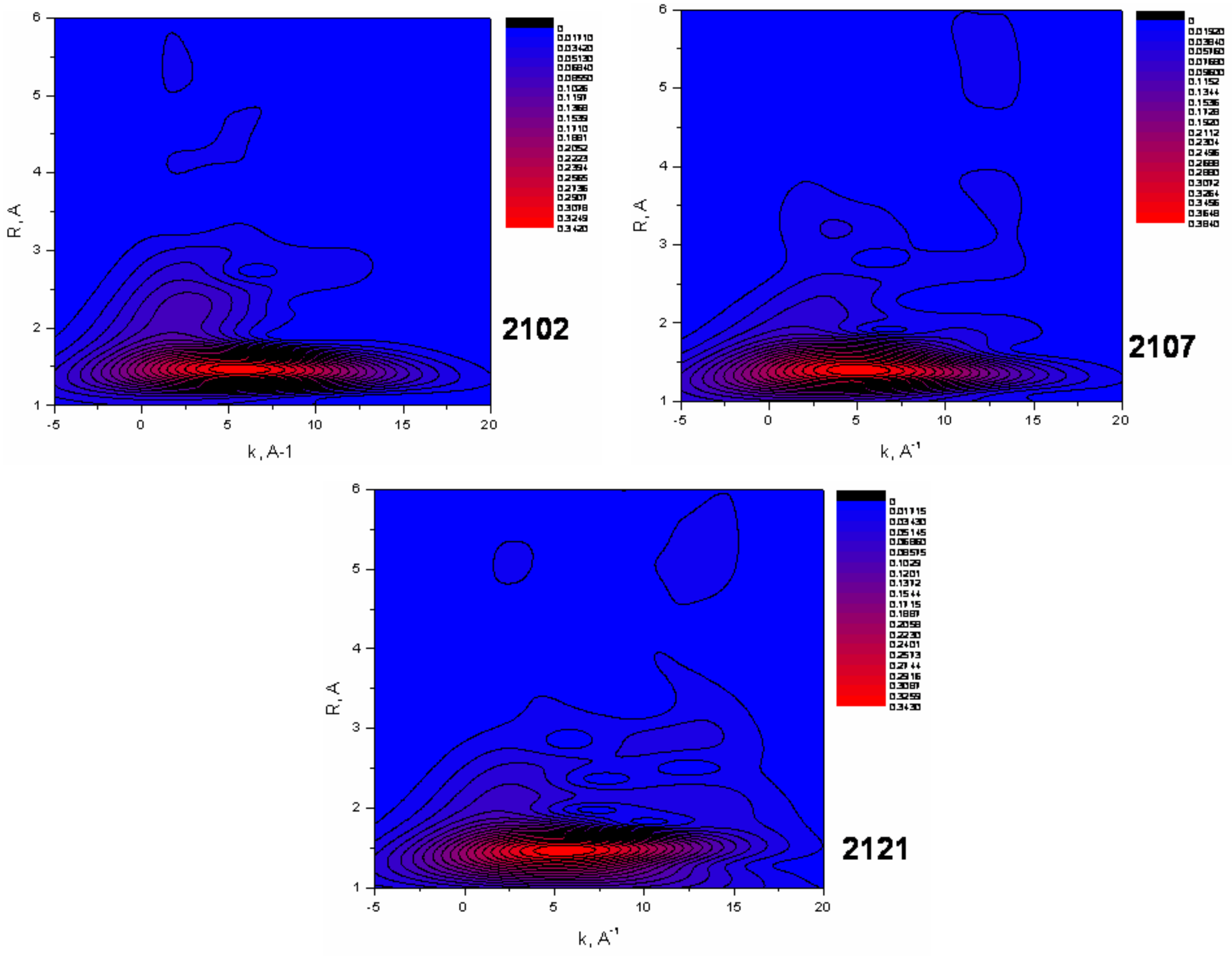

Figure 19. Morlet Wavelet Transform of Fe K Edge EXAFS Spectra of Glasses in Series 21.

CONCLUSION

- actual chemical composition of glasses is close to target one;
- glasses are homogeneous, no crystalline phases or liquid-liquid phase separation were found both in initial and heat-treated and etched glasses;
- the degree of connectedness of the network of coordination polyhedra is the highest for the glass 21-02 and reduces for the glass 21-21 and further 21-07;
- both trigonally and tetrahedrally coordinated boron are present in the structure of glasses;
- fraction of tetrahedrally coordinated boron in the glasses reduces in the row: 21-02 > 21-21 > 21-07;
- aluminum is tetrahedrally coordinated in all glasses and forms AlO_4 units built in silicon-oxygen chains;
- ferrous ions are rather homogeneously distributed in the glass network; the nearest neighbor is positioned at a distance of 3.22-3.25 Å (glasses 21-07, 21-21) or ~3.64 Å (glass 21-02);
- iron in glasses is predominantly trivalent and tetrahedrally coordinated with axial or rhombic distortion of the structural tetrahedron: Fe—O1 = 1.72-1.76 Å and Fe—O2 = 1.90-1.94 Å.
- possible reason of low chemical durability of the glasses is relatively low fraction of tetrahedrally coordinated boron and concentration of Al_2O_3 forming $[BO_{4/2}]^{-}Me^{+}$ and $[AlO_{4/2}]^{-}Me^{+}$ tetrahedral units fixing alkali ions and thus reducing their leaching.

REFERENCES

1. B. Ravel and M. Newville, *J. Synchrotron Radiat*. **12** 537-541 (2005).
2. A.L. Ankudinov and J.J. Rehr, *Phys. Rev*. B **56** 1712-1716 (1997).
3. H. Funke, A.C. Scheinost and M. Chukalina, *Phys. Rev. B*, **71**, 094110 (2005).
4. H. Funke, M. Chukalina and A.C. Scheinost, *J. Synchrotron Radiat*. **14**, 426-432 (2007).
5. www.esrf.fr/exp_facilities/BM20/Software/Wavelets.html.
6. A.A. Appen, *Chemistry of Glass* (Russ.), Khimiya, Leningrad (1974).
7. S.V. Stefanovskii, O.A. Knyazev, T.N. Lashchenova, and S. Merlin, *J. Adv. Mater.* **3** [6] 479-487 (1996).
8. S.V. Stefanovsky and J.C. Marra, *Waste Management '07 Conf.* February 25 – March 1, 2007, Tucson, AZ, ID 7132 (2007).
9. A.P. Kobelev, S.V. Stefanovsky, V.V. Lebedev, D.Y. Suntsov, M.A. Polkanov, O.A. Knyazev, and J.C. Marra, *MS&T 2009 Ceramic Transactions* (in press).
10. K. Nakamoto, *Infrared Spectra of Inorganic and Coordination Compounds*, John Wiley & Sons, Inc. New York – London (2009).
11. V.A. Kolesova, *Glass Phys. Chem.* (Russ.) **12** [10] 4-13 (1986).
12. V.N. Anfilogov, V.N. Bykov, and A.A. Osipov, *Silicate Melts* (Russ.), Nauka, Moscow (2005).
13. I.I. Plyusnina, *Infrared Spectra of Minerals* (Russ.), MGU, Moscow (1977).
14. G.N. Greaves, *J. Non-Cryst. Solids*, 71, 203-217 (1985).
15. G.E. Brown, Jr., G.A. Waychunas, C.W. Ponader, W.E. Jackson, and D.A. McKeown, *EXAFS and Near Edge Structure IV – J. de Physique*. **47** C8, suppl. Au n°12, C8-661 – C8-668 (1986).
16. D.J. Lam, B.W. Veal, H. Chen, and G.S. Knapp, *Scientific Basis for Nuclear Waste Management*, **1**, 97-107 (1979).
17. G.N. Greaves, *EXAFS and Near Edge Structure I*, 248-258 (1982).
18. G. Licheri, G. Paschina, G. Piccaluga, G. Pinna, M. Magini, and G. Cocco, *J. Non-Cryst. Solids*, 72, 211-220 (1985).
19. J. Petiau, G. Calas, T. Dumas, and A.M. Heron, *EXAFS and Near Edge Structure III*, 291-296 (1984).
20. G.A. Waychunas and G.E. Brown, Jr., *EXAFS and Near Edge Structure III*, 336-342 (1983).
21. N. Binsted, G.N. Greaves, and C.M.B. Henderson, *EXAFS and Near Edge Structure IV – J. de Physique*. **47** C8, suppl. Au n°12, C8-837 – C8-840 (1986).

Appendix C. Final Report from SIA Radon on Task 3: Chemistry and Structure of Simulated HLW Glass Systems

Designing-Constructing and Industrial-Inculcating Enterprise

«Daymos, Ltd.»

Office: *#9 Kurchatova Street, Room 340, St.Petersburg, Russia*
Telephone Number: *(812) 550-41-59; (812) 550-41-64* **Facsimile Number:** *(812) 550-41-59*
E-Mail Address: *daymos@mail.wplus.net*

FINAL REPORT

Glass Structural Characterization and Analysis

Subcontract Number AC69549N together with Change Notice Number 1

Task 3: Chemistry and Structure of Simulated HLW Glass Systems

3.2. Provide interim data report on analyses completed on glass samples

3.3. Provide final report describing analytical techniques utilized, measurement results and data interpretation for glass samples studied

St.Petersburg
2010

INTRODUCTION

The partitioning of boron between trigonal and tetrahedral coordination in aluminoborosilicate glass systems can be determined quantitatively using the nuclear magnetic resonance (NMR) technique. However, the presence of iron in HLW glasses at concentrations greater than 5 wt% prevents the use of NMR. The objective of this task is to apply the insight gained from Task 1 in studying the impact of varying levels of boron, alkali, and some additives such as Ca and Mn on the coordination chemistry of simulated HLW glass systems using XPS, XANES, EXAFS, EPR, IR and Raman spectroscopy.

Sample glasses have been made using SB6 simulant (high in both Al and Fe) with 12 different frit compositions at a constant waste loading of 36 wt.% (Tables I and II). The baseline frit composition is Frit 418 and the remaining frit compositions contain 8-16 wt% B_2O_3, 4-8 wt% Na_2O, 0-4 wt% MnO and 0-2 wt% CaO. Glasses were delivered by customer (SRNL).

Table I. Glass compositions, wt.%

Oxides	35	36	37	38	39	40	41	42	43	44	45	46
Li_2O	5.12	5.12	5.12	5.12	5.76	5.12	5.12	5.12	5.12	5.12	5.12	5.12
B_2O_3	5.12	8.96	7.04	7.04	7.04	5.12	5.12	5.12	5.12	5.12	5.12	10.24
Na_2O	12.59	12.59	12.59	11.31	10.67	12.59	11.95	11.31	11.95	11.31	11.31	10.03
MgO	0.27	0.27	0.27	0.27	0.27	0.27	0.27	0.27	0.27	0.27	0.27	0.27
Al_2O_3	10.78	10.78	10.78	10.78	10.78	10.78	10.78	10.78	10.78	10.78	10.78	10.78
SiO_2	48.75	44.91	46.83	46.83	45.55	48.11	48.11	47.47	47.47	47.47	46.19	46.19
SO_3	0.33	0.33	0.33	0.33	0.33	0.33	0.33	0.33	0.33	0.33	0.33	0.33
K_2O	0.03	0.03	0.03	0.03	0.03	0.03	0.03	0.03	0.03	0.03	0.03	0.03
CaO	0.48	0.48	0.48	0.48	0.48	0.48	0.48	0.48	1.76	1.76	1.76	0.48
TiO_2	0.01	0.01	0.01	0.01	0.01	0.01	0.01	0.01	0.01	0.01	0.01	0.01
MnO	2.75	2.75	2.75	4.03	5.31	3.39	4.03	5.31	3.39	4.03	5.31	2.75
Fe_2O_3	9.73	9.73	9.73	9.73	9.73	9.73	9.73	9.73	9.73	9.73	9.73	9.73
NiO	1.16	1.16	1.16	1.16	1.16	1.16	1.16	1.16	1.16	1.16	1.16	1.16
CuO	0.08	0.08	0.08	0.08	0.08	0.08	0.08	0.08	0.08	0.08	0.08	0.08
SrO	0.02	0.02	0.02	0.02	0.02	0.02	0.02	0.02	0.02	0.02	0.02	0.02
ZrO_2	0.11	0.11	0.11	0.11	0.11	0.11	0.11	0.11	0.11	0.11	0.11	0.11
Sum	97.33	97.33	97.33	97.33	97.33	97.33	97.22	97.33	97.33	97.33	97.33	97.33

Table II. Glass compositions, mol.%

Oxides	35	36	37	38	39	40	41	42	43	44	45	46
Li_2O	11.41	11.47	11.44	11.46	12.83	11.42	11.43	11.45	11.41	11.42	11.44	11.49
B_2O_3	4.90	8.62	6.75	6.76	6.73	4.90	4.91	4.91	4.89	4.90	4.91	9.86
Na_2O	13.52	13.60	13.56	12.20	11.45	13.54	12.86	12.20	12.83	12.16	12.18	10.85
MgO	0.45	0.45	0.45	0.45	0.45	0.45	0.45	0.45	0.45	0.45	0.45	0.45
Al_2O_3	7.04	7.08	7.06	7.07	7.03	7.05	7.05	7.07	7.04	7.04	7.06	7.09
SiO_2	54.01	50.05	52.03	52.12	50.43	53.36	53.40	52.80	52.58	52.63	51.32	51.53
SO_3	0.27	0.28	0.28	0.28	0.27	0.27	0.27	0.28	0.27	0.27	0.28	0.28
K_2O	0.02	0.02	0.02	0.02	0.02	0.02	0.02	0.02	0.02	0.02	0.02	0.02
CaO	0.57	0.57	0.57	0.57	0.57	0.57	0.57	0.57	2.09	2.09	2.10	0.57
TiO_2	0.01	0.01	0.01	0.01	0.01	0.01	0.01	0.01	0.01	0.01	0.01	0.01
MnO	2.58	2.60	2.59	3.80	4.98	3.18	3.79	5.00	3.18	3.78	5.00	2.60
Fe_2O_3	4.06	4.08	4.07	4.07	4.05	4.06	4.06	4.07	4.06	4.06	4.07	4.08
NiO	1.03	1.04	1.04	1.04	1.03	1.04	1.04	1.04	1.03	1.03	1.04	1.04
CuO	0.07	0.07	0.07	0.07	0.07	0.07	0.07	0.07	0.07	0.07	0.07	0.07
SrO	0.01	0.01	0.01	0.01	0.01	0.01	0.01	0.01	0.01	0.01	0.01	0.01
ZrO_2	0.06	0.06	0.06	0.06	0.06	0.06	0.06	0.06	0.06	0.06	0.06	0.06
Sum	100.00	100.00	100.00	100.00	100.00	100.00	100.00	100.00	100.00	100.00	100.00	100.00
ψ_B*	2,14	1.22	1.56	1.35	1.25	2.14	2.00	1.86	2.00	1.86	1.86	0.79
ψ_B(Fe)**	1.89	1.08	1.37	1.17	1.07	1.89	1.75	1.61	1.75	1.61	1.61	0.66

* $\psi_B = \{(Na_2O+K_2O+BaO)+[0.7(CaO+SrO+CdO+PbO)+[0.3(Li_2O+ MgO+ZnO)]-Al_2O_3\}/B_2O_3$ [1]

** $\psi_B(Fe) = \{(Na_2O+K_2O+BaO)+[0.7(CaO+SrO+CdO+PbO)+[0.3(Li_2O+ MgO+ZnO)]-Al_2O_3-0.3Fe_2O_3\} / B_2O_3$

The ψ_B and ψ_B(Fe) values range between 0.79 and 2.14 and between 0.66 abd 1.89, respectively at moderate silica contents (50-54 mol.%) that points to significant fraction of trigonally coordinated boron. The glasses #35 and #40 should have th highest fraction of tetrahedrally coordinated boron, whereas the glass #46 – the lowest one.

EXPERIMENTAL

Samples were examined by X-ray diffraction (XRD) using a Rigaku D / Max 2200 diffractometer (Cu Kα radiation, 40 keV voltage, 20 mA current, stepwise 0.02 degrees 2θ). Glasses were studied by optical microscopy using an OLYMPUS BX51 polarizing microscope, infrared spectroscopy using a modernized IKS-29 spectrophotometer (compaction of powdered glasses in pellets with KBr) within the range of 4000–400 cm^{-1} and Raman spectroscopy using a Jobin Yvon U1000 spectrophotometer operated at an excitation wavelength of 532 nm.

X-ray absorption (XAS) spectra were recorded at the Structural Materials Science (STM) Beamline of the synchrotron source at RRC "Kurchatov Institute". The glass samples were measured at room temperature either as dispersed powder or as pellets pressed from powder mixed with sucrose in the transmission mode using a Si(220) channel-cut monochromator and two air-filled ionization chambers. Fluorescence spectra were also acquired. Powders of chemically pure Fe oxides Fe_2O_3 and FeO were used as standards and measured under identical conditions. Experimental XAFS spectra were fitted in R-space using an

IFEFFIT package [2] and crystal structures of corresponding oxides and silicates. In the fitting, *ab initio* photoelectron backscattering amplitudes and phases calculated self-consistently using FEFF8 [3] were used.

Wavelet transform (WT) is commonly applied to evaluation of complex time-frequency signals. As shown in refs [4,5], WT is easily adapted to EXAFS analysis, and the expression of the WT of the k^n-weighted EXAFS data takes the form:

$$W_{\chi}^{\psi}(k,r) = (2r)^{1/2} \int_{-\infty}^{\infty} \chi(k') k'^{n} \, \psi^{*}[2r(k'-k)] dk', \qquad (1)$$

where χ(k) is the EXAFS signal and $\psi^{*}[2r(k'-k)]$ is the complex wavelet function.

The WT is able to resolve the k dependence of the absorption signal, which potentially allows separation of contributing backscattering atoms even situated at the same distances from the core. One of the advantages of the wavelet analysis is the visualization of the WT modulus in a k-R plot, which provides an easy way to interpret the results. Our analysis of EXAFS data for Pu and Hf were performed using the FORTRAN program HAMA employing Morlet wavelet algorithm [6]. The Morlet wavelet is well-suited for EXAFS signal since it consists of a slowly varying amplitude term and a fast oscillating phase term. Its mathematical description is broadly analogous to the Fourier transform. The Morlet wavelet is obtained by taking a complex sine wave with frequency η (as in FT) and by confining it with a Gaussian envelope with the half width σ,

$$\psi(k) = \frac{1}{(2\pi)^{1/2}\sigma} \exp(i\eta k) \exp(-k^{2}/2\sigma^{2}). \qquad (2)$$

The choice of the η and σ parameters is important for data analysis since, besides other issues, it determines resolution in k-R space. Various combinations of these parameters were used in an attempt to resolve contributions from atoms at close distances from the central atom. As shown in ref.[5] use of higher k-weighting decreases resolution in the k-space, since backscattering amplitudes become flattened and shifted to higher values. Nevertheless, WT modulus plots for different k weights are shown to emphasize contributions of light and heavy backscatterers. Note, that in all plots of the WT modulus the interatomic distances are given without phase shift correction.

RESULTS AND DISCUSSION

XRD study

XRD patterns show that all the samples are composed of major glass and minor spinel structure phase (Figure 1). Because lattice parameter of the spinel phase is same in all the samples, it may be suggested that chemical composition of this phase is similar in all the samples as well.

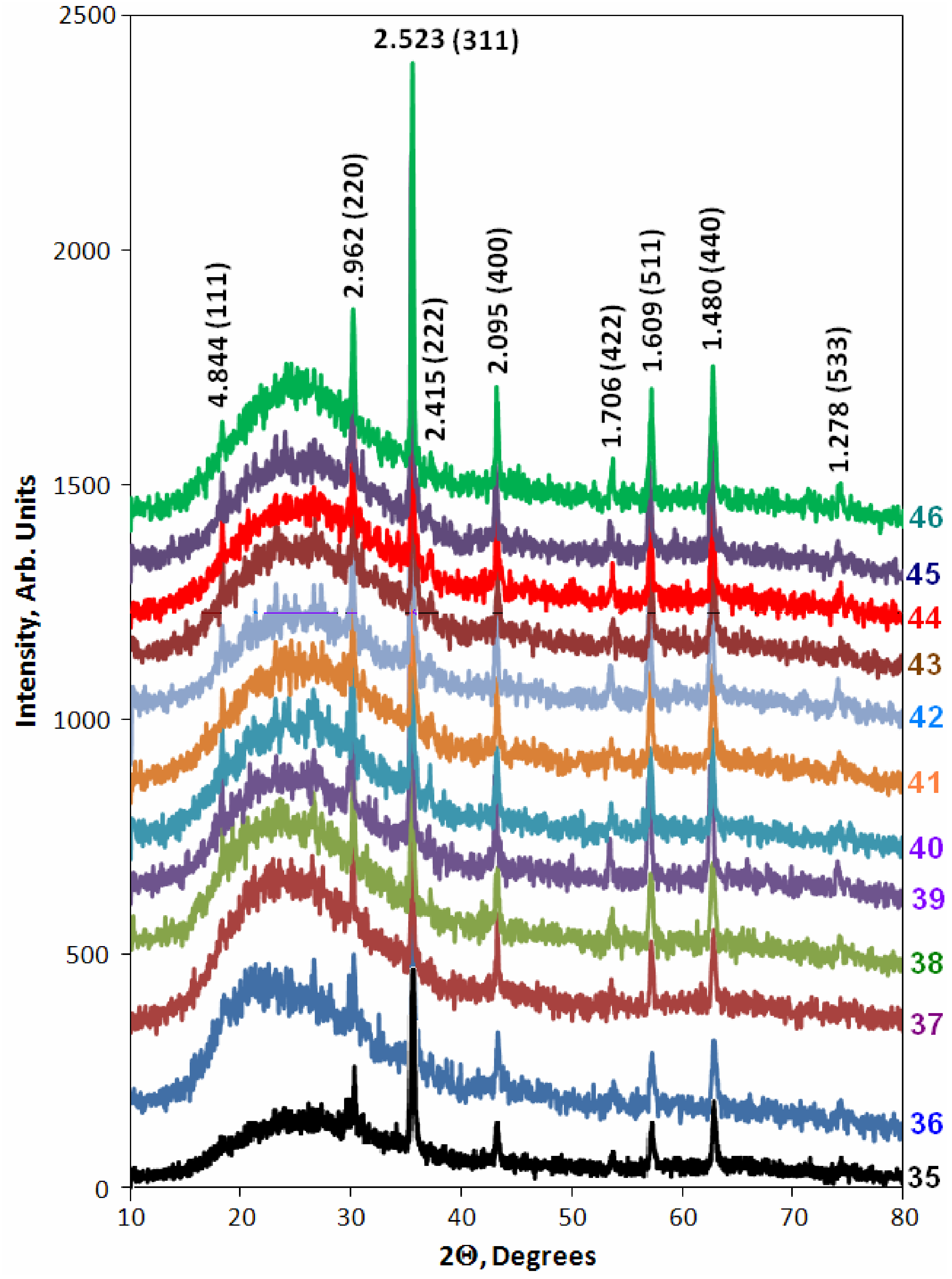

Figure 1. XRD patterns of the samples.

Optical Microscopy Study

Microphotograph of the general view of sample #35 (Figure 2*a*) shows dominance of light transparent glass containing spinel occurred as both isometric grains tens of microns in size and the finest crystals of about 1 μm in size. Glass matrix contains wavy bands displaying features of melt flowing and differing in amount of fine crystals in glass. Wavy-banded distribution of microcrystals causes fluidal texture of the glass which is typical for glassy volcanic rocks. Moreover gas bubbles from tens to hundreds microns in diameter are seen well in the lapping.

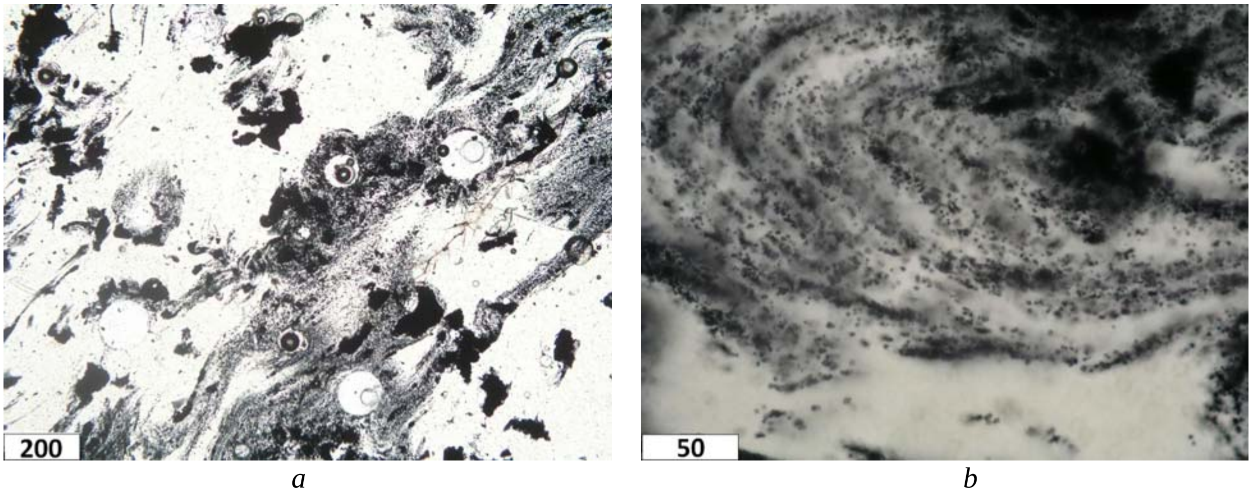

a *b*

Figure 2. Microphotographs at single Nichol of the lapping of the sample #35.

A detail of the lapping on Figure 2*a* at higher magnification demonstrates that microcrystals of the spinel phase are the finest cubic crystals about 1 μm in size. This microphotograph clearly characterizes features of distribution of microcrystals in glass.

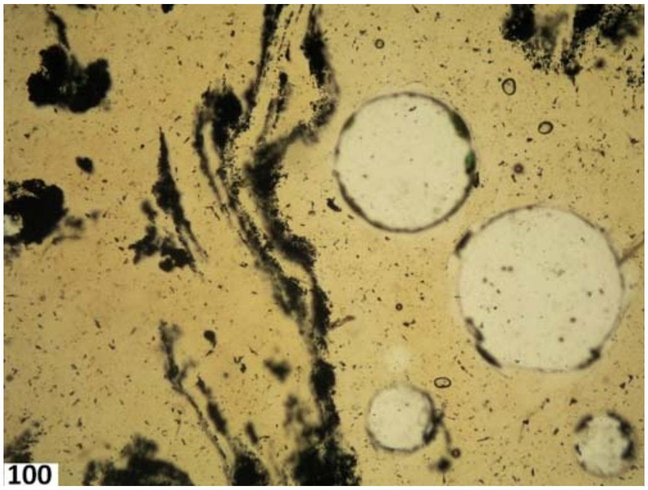

Figure 3. Microphotograph at single Nichol of the lapping of the sample #36.

Specific feature of the glassy matrix in the sample #36 are light-brown coloring of glass and relatively low content of spinel (Figure 3). Spinel forms either irregular grains or elongated wavy-type grains

emphasizing elements of the fluidal texture. Minor cubic microcrystals of spinel are also present. Gas bubbles 50-200 μm in diameter occurred in the vitreous and are non-uniformly distributed.
Figure 4a demonstrates general view of the lapping of sample #37. Glassy matrix is characterized by clearly appeared fluidal texture and light-brown coloring. Spinel is rather non-uniformly distributed over the bulk and occurs predominantly as fine (~1 μm in size) crystals. Glass contains numerous gas bubbles up to 0.5 mm in diameter.

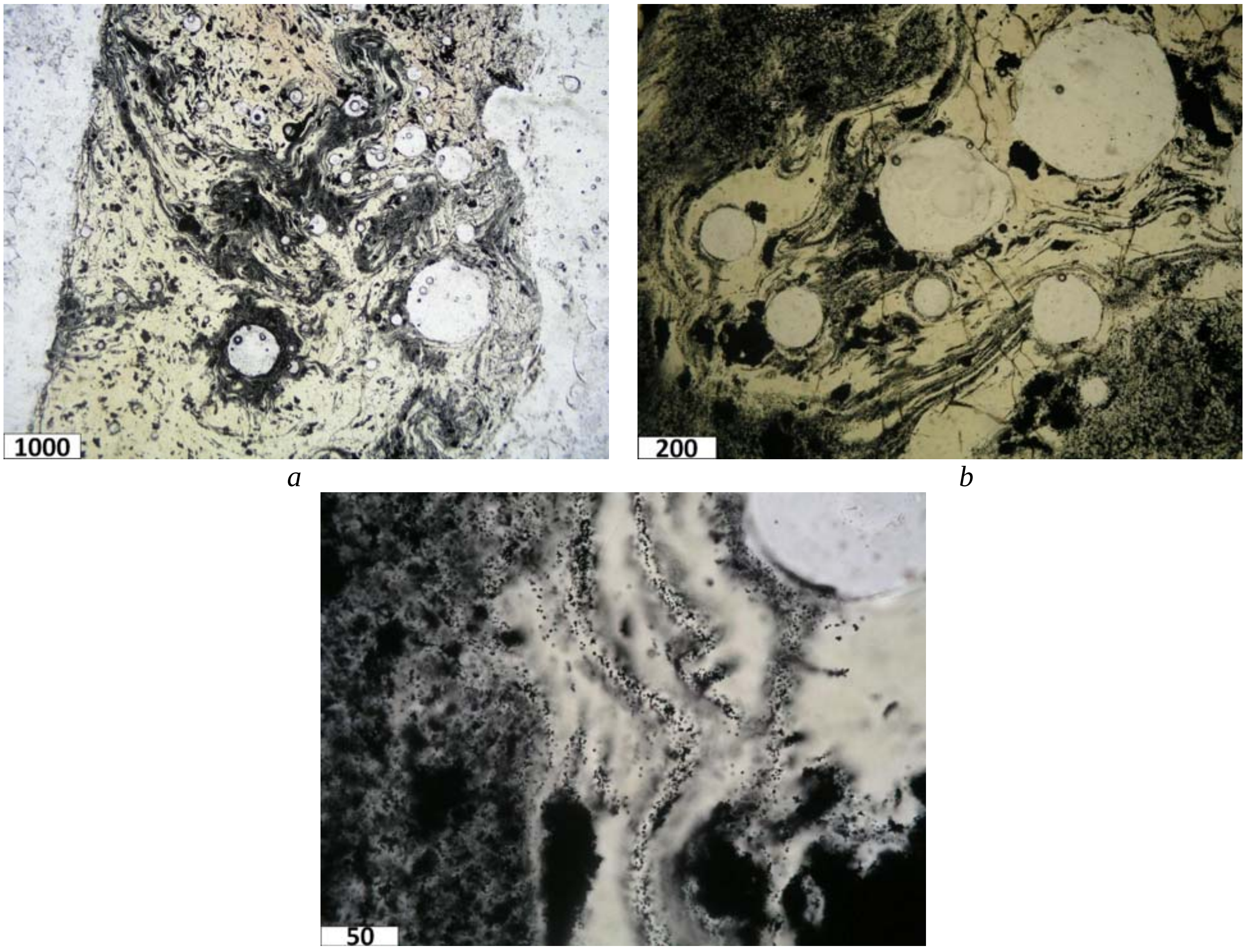

a *b*

c

Figure 4. Microphotographs at single Nichol of the lapping of the sample #37.

Figure 4*b* demonstrates fragment of the same lapping enriched with spinel. It is seen well that fluidity is represented by alternation of wavy bands enriched and depleted with fine cubic spinel crystals. Dense aggregates of cubic spinel crystals are occasionally occur. As seen at higher magnification (Figure 4*c*) spinel occurs as both individual cubic crystals about 1 μm in size and aggregates of fine crystals forming dense opaque areas.

Glass in the lapping of the sample #38 has light-brown coloring and is characterized by strong cracking showing high mechanical stress (Figure 5). Amount of spinel is rather minor. Major fraction of spinel is represented by isometric grains. Fine cubic crystals are concentrated at small area of the lapping. Wavy-banded distribution of cubic microcrystals determines fluidal texture of this area.

The lapping of the sample #39 is a light-brown glass with high contents of spinel and gas bubbles (Figure 6). Spinel is present as both isometric grains and cubic microcrystals. There are areas both enriched with microcrystals and free of crystals. The first of them have clear fluidal texture. Cracking is negligible.

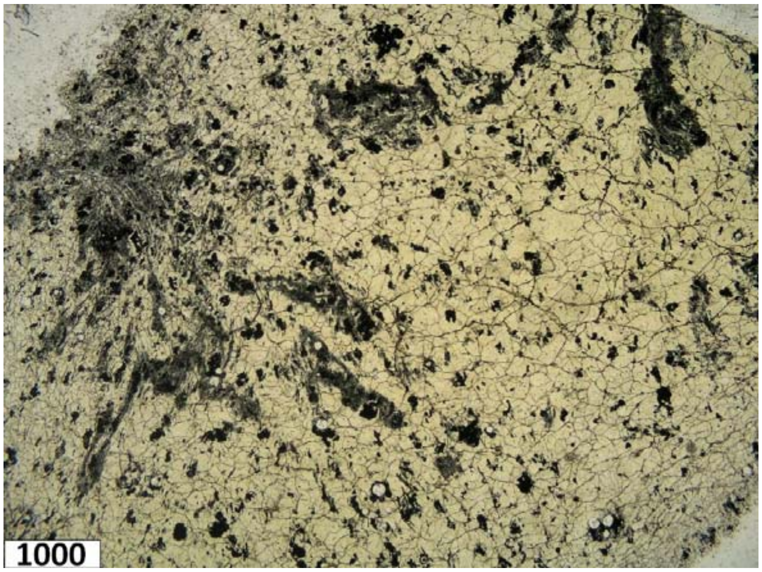

Figure 5. Microphotograph at single Nichol of the lapping of the sample #38.

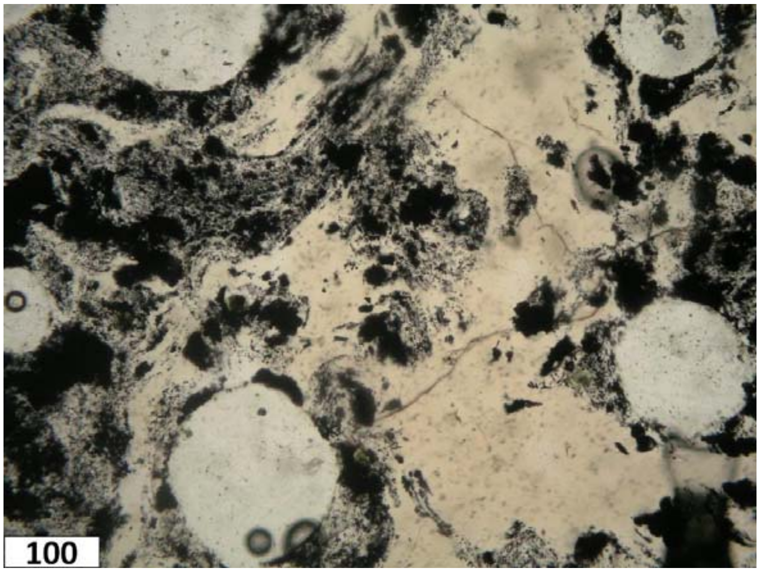

Figure 6. Microphotograph at single Nichol of the lapping of the sample #39.

Glassy matrix in the lapping of the sample #40 is strongly enriched with spinel (Figure 7). Spinel occurs as both isometric grains and cubic microcrystals. Fluidity is appeared locally. Areas not containing spinel are small in size and occur rarely. In spite of high spinel content glass is light and transparent. This demonstrates absence of the dependence between iron oxides content in the glassy matrix and glass coloring. Microcracking of the glass is negligible.

Glassy matrix in the lapping of the sample #41 (Figure 8) has low spinel content (<10 vol.%). Nearly all the spinel forms isometric grains. Amount of microcrystals is negligible. Glass has light brown-green coloring and numerous cracks due to mechanical stresses.

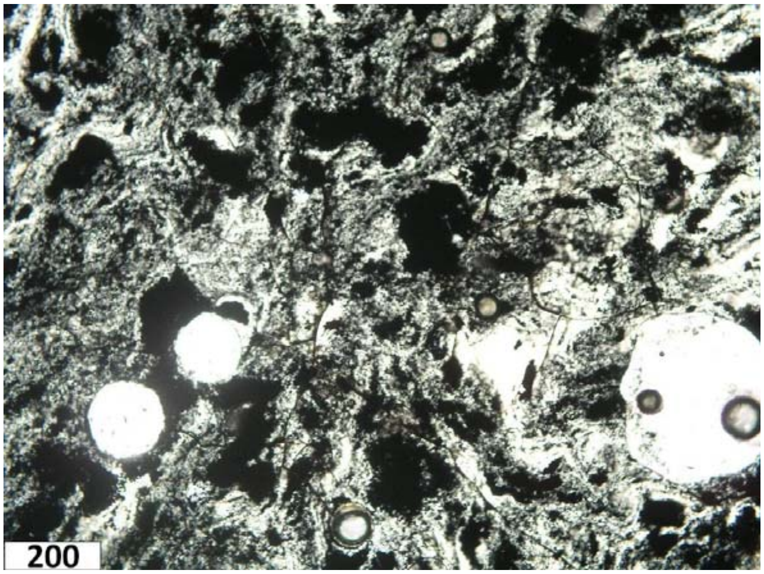

Figure 7. Microphotograph at single Nichol of the lapping of the sample #40.

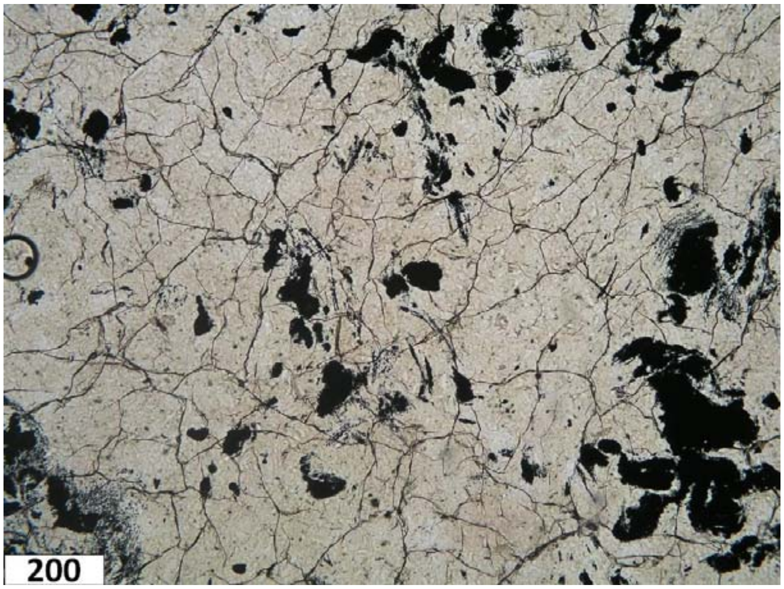

Figure 8. Microphotograph at single Nichol of the lapping of the sample #41.

The lapping of the sample #42 is represented by glass with high content of spinel and gas bubbles (Figure 9). Bubbles are up to 200 μm in size. Glass has brown color, fluidity is poorly appeared. Spinel forms predominantly isomeric grains. Content of cubic microcrystals is negligible.

The lapping of the sample #43 is composed of poorly colored brown-green glass with minor spinel forming isometric grains (Figure 10). Spinel content may be evaluated as 6-8 vol.%. Rare aggregates of microcrystals and gas bubbles up to 200 μm in diameter also occur. Cracking is negligible.

The lapping of the sample #44 is composed of green-brown glass with high spinel content (25-30 vol.%). Major spinel is represented by isometric randomly distributed grains. Minor cubic microcrystals determine fluidal texture of the glassy matrix due to their wavy-banded distribution over the matrix. Large (up to 1.5 mm in diameter) gas bubbles are also present. Microcracking is nearly absent (Figure 11).

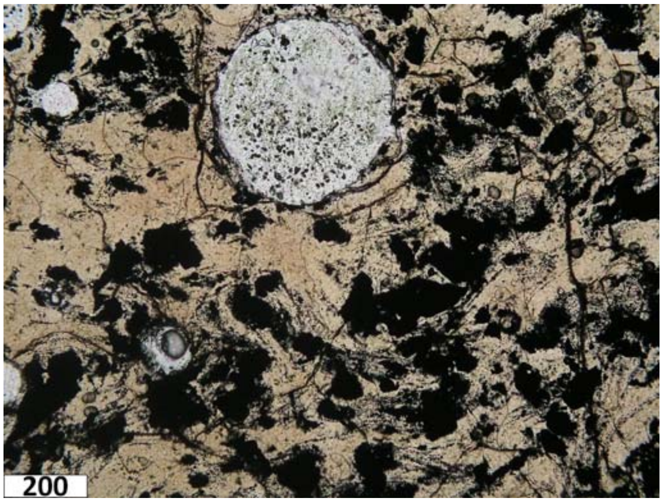

Figure 9. Microphotograph at single Nichol of the lapping of the sample #42.

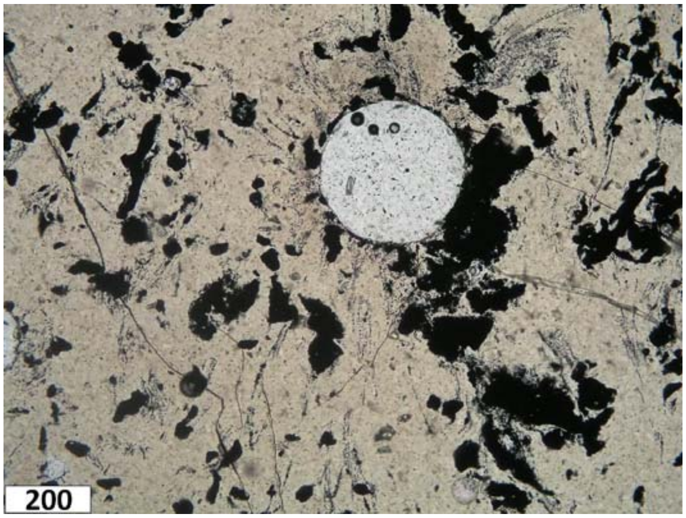

Figure 10. Microphotograph at single Nichol of the lapping of the sample #43.

The lapping of the sample #45 is composed of yellow-green glass with minor spinel content (~10 vol.%) – see Figure 12. Major spinel forms isomeric grains. Cubic microcrystals with wavy-banded distribution are present in local areas. Isolated gas bubbles 10-20 μm in diameter also occur. In crossed Nichols areas with weakly appeared double reflection probably due to initial stage of glass devitrification were found.

The lapping of the sample #46 (Figure 13) is composed of non-uniformly colored (from clear transparent to light-yellow) glass with minor spinel (5-10 vol.%). Major spinel is isometric randomly distributed grains. Minor spinel is is cubic microcrystals occurred in local areas. The latter forms short discontinuous bands. Glass contains numerous small gas bubbles. Most of them are <20 μm in diameter.

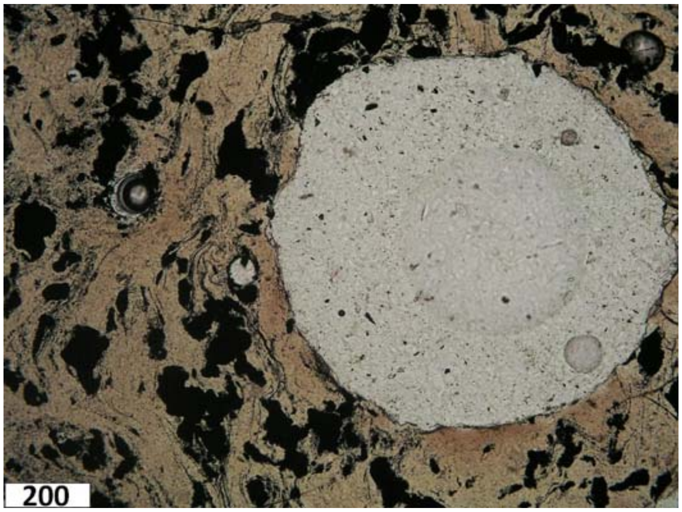

Figure 11. Microphotograph at single Nichol of the lapping of the sample #44.

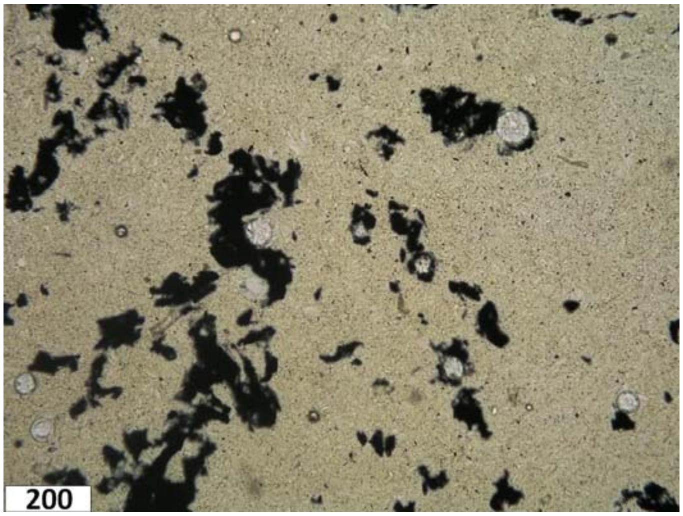

Figure 12. Microphotograph at single Nichol of the lapping of the sample #45.

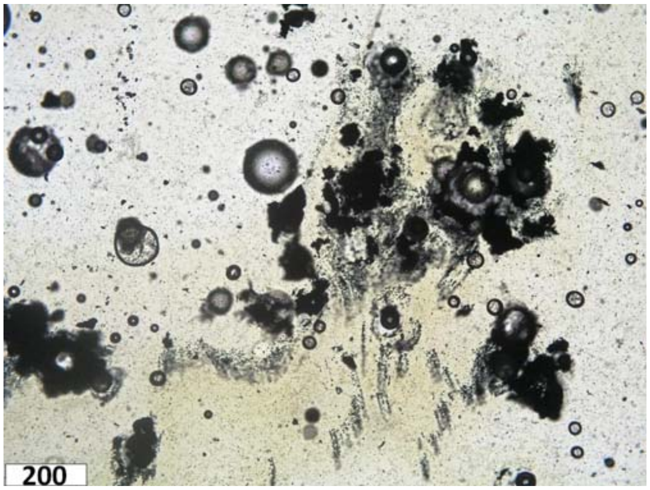

Figure 13. Microphotograph at single Nichol of the lapping of the sample #46.

Major features of all the samples are as follows:

- All the samples are composed of major glass and minor spinel;
- All the samples contain gas bubbles with variable diameter (from <10 μm to >1 mm);
- Coloring of glass varies from nearly clear to brown;
- Spinel forms both isometric grains and cubic microcrystals (~1 μm);
- Microcrystals are aggregated in bands with variable glass and spinel contents;
- Relative location of the bands is caused by flowing of various portion of glassmelt with various viscosity;
- Wavy profile of the bands is similar to that in volcanic glasses with fluidal texture;
- No devitrification of glass was found.

Major differences between the samples are as follows:

- The samples (possibly various parts of the same sample as well) are different in quantitative glass to spinel ratio;
- Significant differences was found in a ratio of isometric grains to cubic microcrystals;
- Fluidal texture is variably appeared; in some samples fluidity takes place only in local areas or absent at all;
- Degree of cracking in the lappings is widely varied.

IR spectroscopic study

IR spectra of all the samples are similar (Figures 14 and 15). IR spectra of glasses (Figure 16) consist of the bands due to stretching (3100-3600 cm^{-1}) and bending modes (1600-1800 cm^{-1}) in the molecules of absorbed and structurally bound water, weak bands due to hydrogen bonds in the structure of glasses and numerous bands lower 1600 cm^{-1} due to stretching and bending modes in the units forming anionic motif of the structure of glasses.

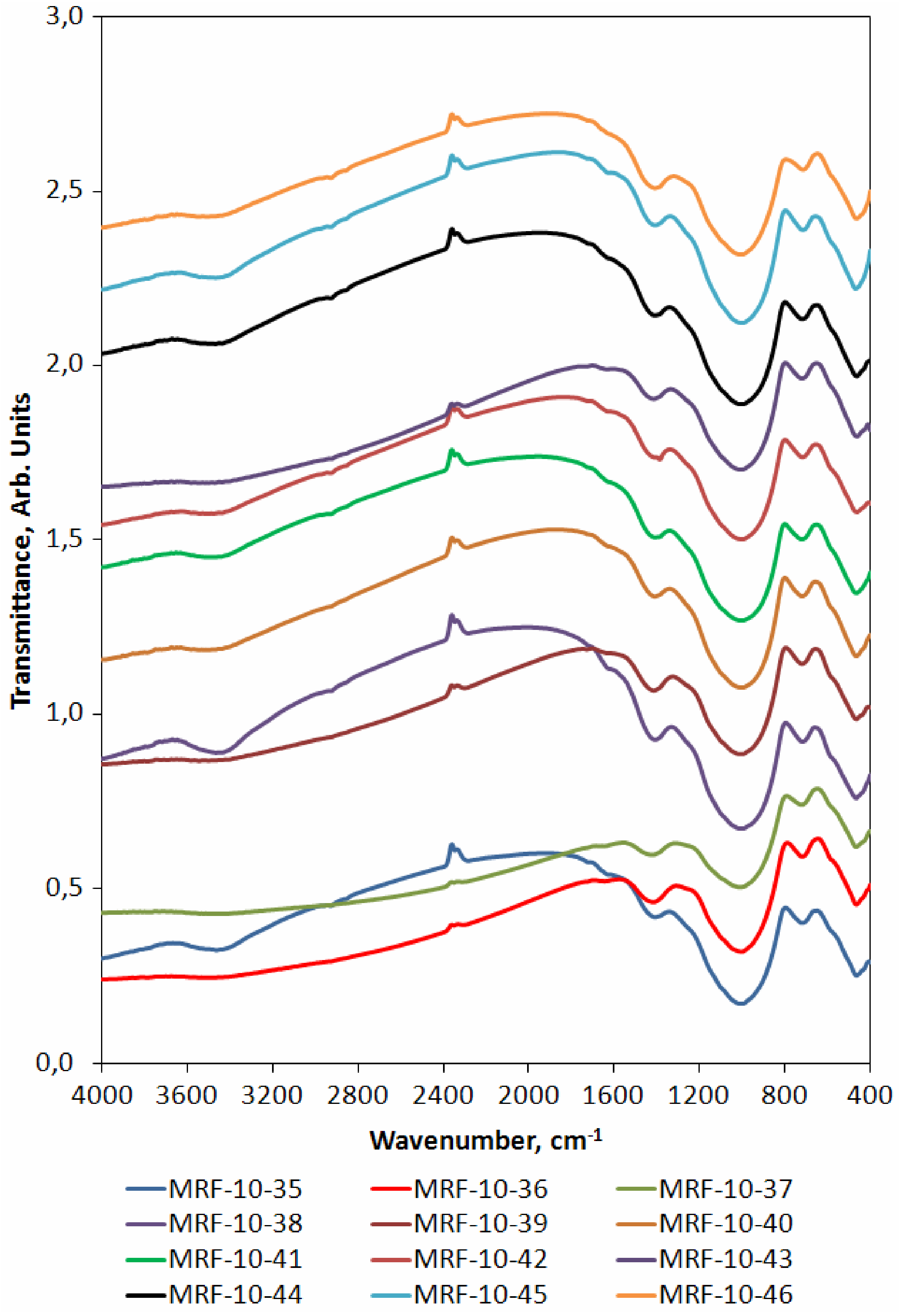

Figure 14. IR spectra of the samples within the range of 4000-400 cm^{-1}.

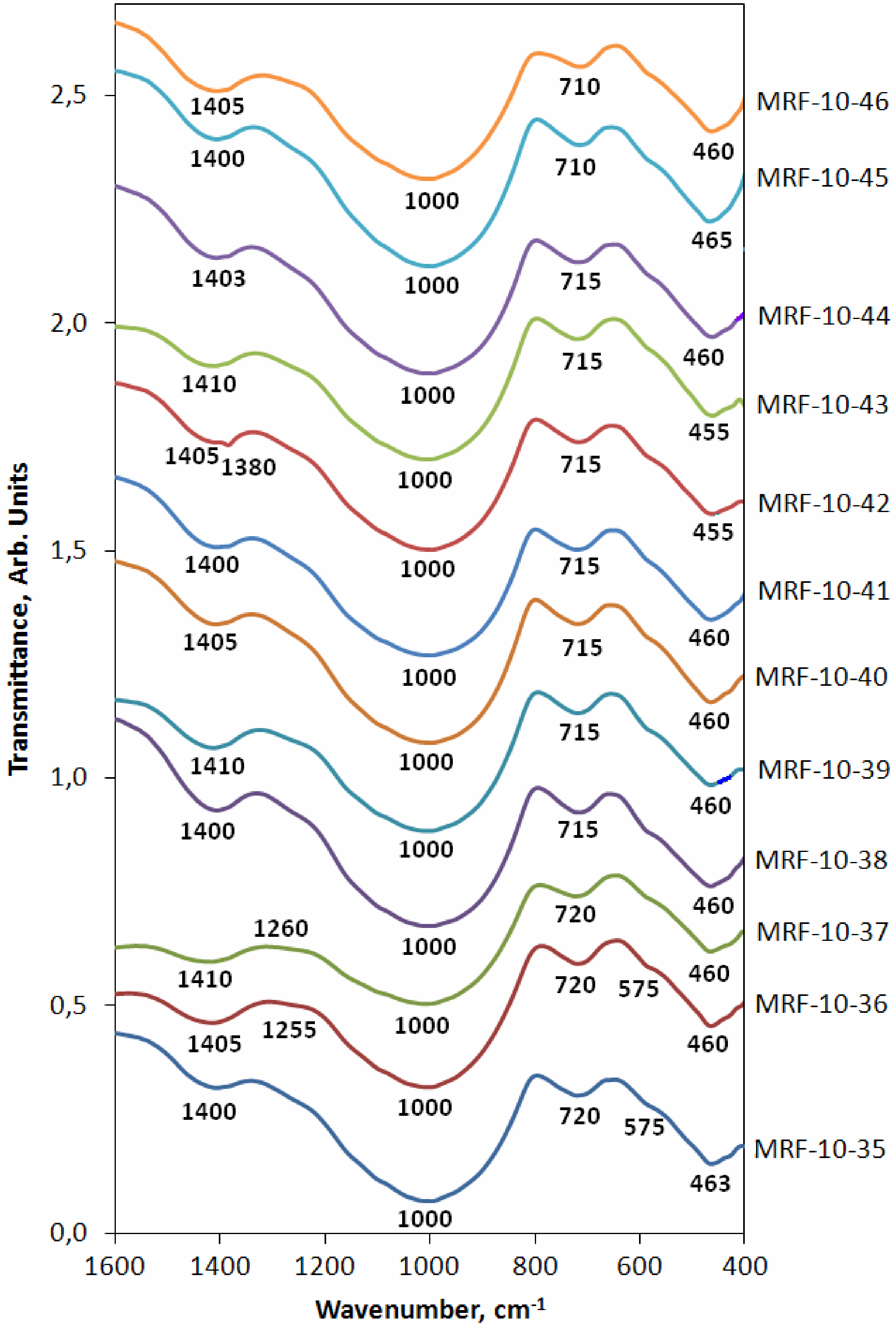

Figure 15. Fragments of IR spectra of the samples within the range of 1600-400 cm^{-1}.

IR spectra of all the glasses within the range of 4000-1600 cm^{-1} (Figure 14) consist of the bands due to stretching and bending modes in silicon-oxygen, boron-oxygen, aluminum-oxygen and iron-oxygen (in spectra of glasses A1, B1 and D1 only) structural groups. The wavenumber ranges of 1550-1300 cm^{-1} and ~1260-1270 cm^{-1} are typical of vibrations in the boron-oxygen groups with trigonally coordinated boron (boron-oxygen triangles BO_3) [7]. These bands were attributed as components of twice degenerated asymmetric valence ν_3 O−B−O vibrations (stretching modes). The band with components ~710-730 and 650-670 cm^{-1} may be associated with twice degenerated asymmetric deformation δ (ν_4) O−B−O vibrations (bending modes) [7]. Strong absorption in both IR and Raman spectra within the range of 1150-850 cm^{-1} is caused by asymmetric ν_3 vibrations (stretching modes) in silicon-oxygen units bound to zero (850-900 cm^{-1}), one (~900-950 cm^{-1}), two (~950-1050 cm^{-1}), three (~1050-1100 cm^{-1}) and four (~1100-1150 cm^{-1}) neighboring SiO_4 tetrahedra (Q^0, Q^1, Q^2, Q^3, Q^4, respectively) [8] and, in less extent, BO_4 tetrahedra (1000-1100 cm^{-1}) [9]. In IR spectra of all the glasses the broad band within the range of ~800-1200 cm^{-1} is multicomponent due to superposition of vibrations (stretching modes) in SiO_4 and BO_4 tetrahedra. Stretching modes of Al—O bonds in AlO_4 tetrahedra and Fe—O bonds in FeO_4 tetrahedra are positioned at 700-800 cm^{-1} and 550-650 cm^{-1}, respectively. Bending modes of Si—O—Si bonds in SiO_4 tetrahedra are positioned within the range of 350-550 cm^{-1}.

As seen from Figure 14, the bands at 3300-3600 cm^{-1} and 1620-1650 cm^{-1} are correlated on intensity and they may be attributed to stretching and bending modes in molecules of absorbed or structurally-bound water [10]. In the spectra of all the glasses the bands due to vibrations in water molecules or Me—O—H bonds have much lower intensity than the bands due to vibration in anionic motif of the glass structure.

The IR spectra of all the glasses within the range of 1600-400 cm^{-1} are similar (Figure 15). This indicates that all the glasses have similar structure of their anionic motif. As follows from position of major maximum of the strongest band 1200-800 cm^{-1} (~1000 cm^{-1}) the base of structural network is metasilicate chains and rings where the Q^2 units are predominant. Bridging bonds Si—O—Fe and Si—O—Al bonding SiO_4 and FeO_4 and AlO_4 tetrahedra and thus increasing the degree of connectedness of the glass network are positioned within the range of 950-880 cm^{-1} and may contribute to lower wavenumber edge of the band 1200-800 cm^{-1}. The bans with a maximum at 455-463 cm^{-1} is due to bending modes in SiO_4 tetrahedra and Si—O—Si bonds (in the most extent) and Si—O—Al and Si—O—Fe bonds (in less extent). The band with a maximum at 710-720 cm^{-1} is due to superposition of symmetric stretching modes in SiO_4 tetrahedra and asymmetric stretching modes in AlO_4 tetrahedra. Weak band observed as a shoulder at ~575 cm^{-1} is due to vibrations in FeO_4 tetrahedra. Boron in these glasses is predominantly threefold-coordinated and occurs as boron-oxygen triangles. Part of them possibly enters complex borate groups bound with boron-oxygen tetrahedra.

Thus, the structural network is primarily composed of metasilicate chains and rings with embedded AlO_4 and FeO_4 tetrahedra. Boron-oxygen constituent exists separately.

Raman spectroscopic study

Raman spectra of the glassy samples are shown on Figure 16. Depolarized spectra are given on Figure 17. Spectra of the samples ##39, 40, 44 and 45 differ markedly from the rest spectra. These glasses seem to be higher structured or contain higher amount of crystalline phase (spinel).

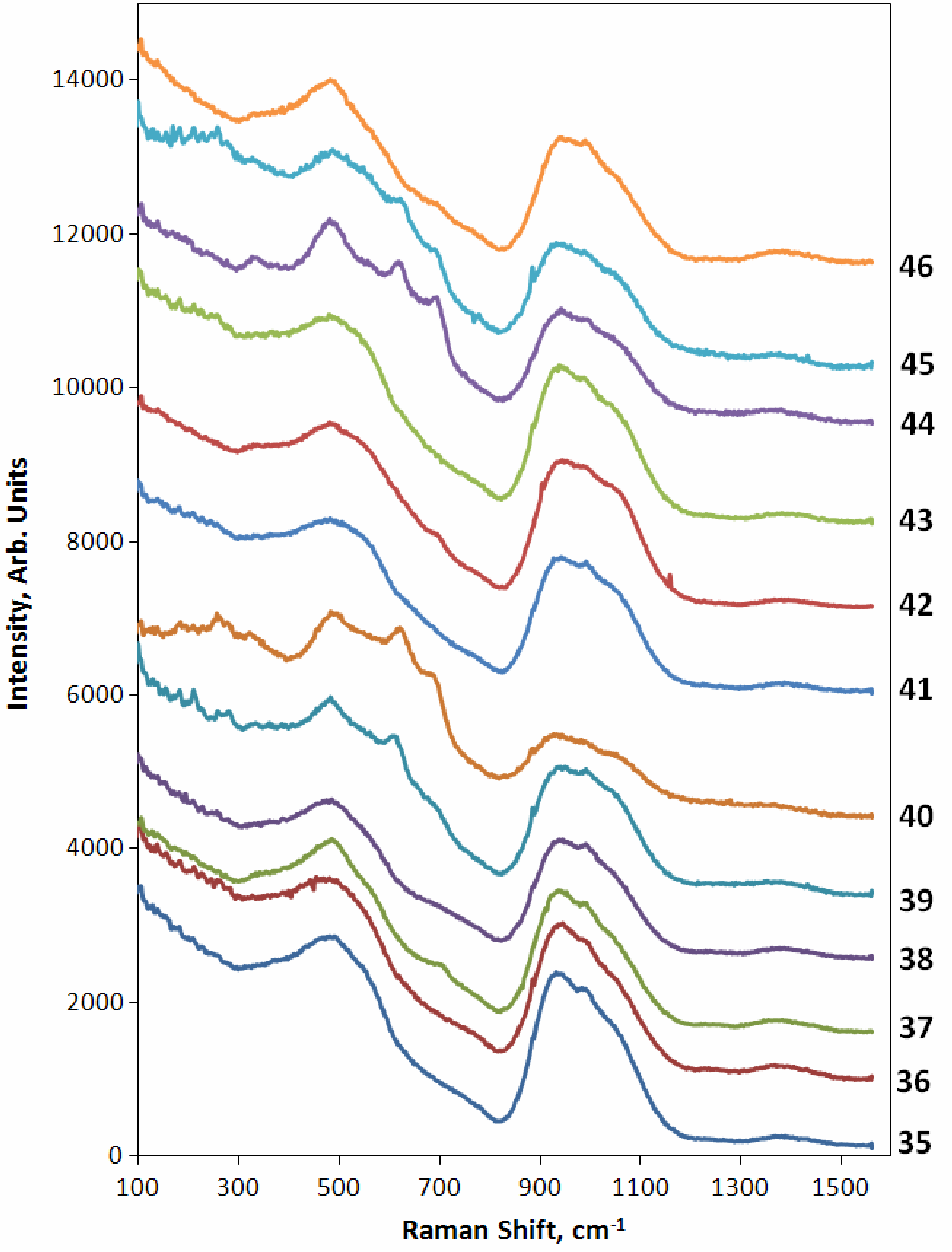

Figure 16. Raman spectra of the samples.

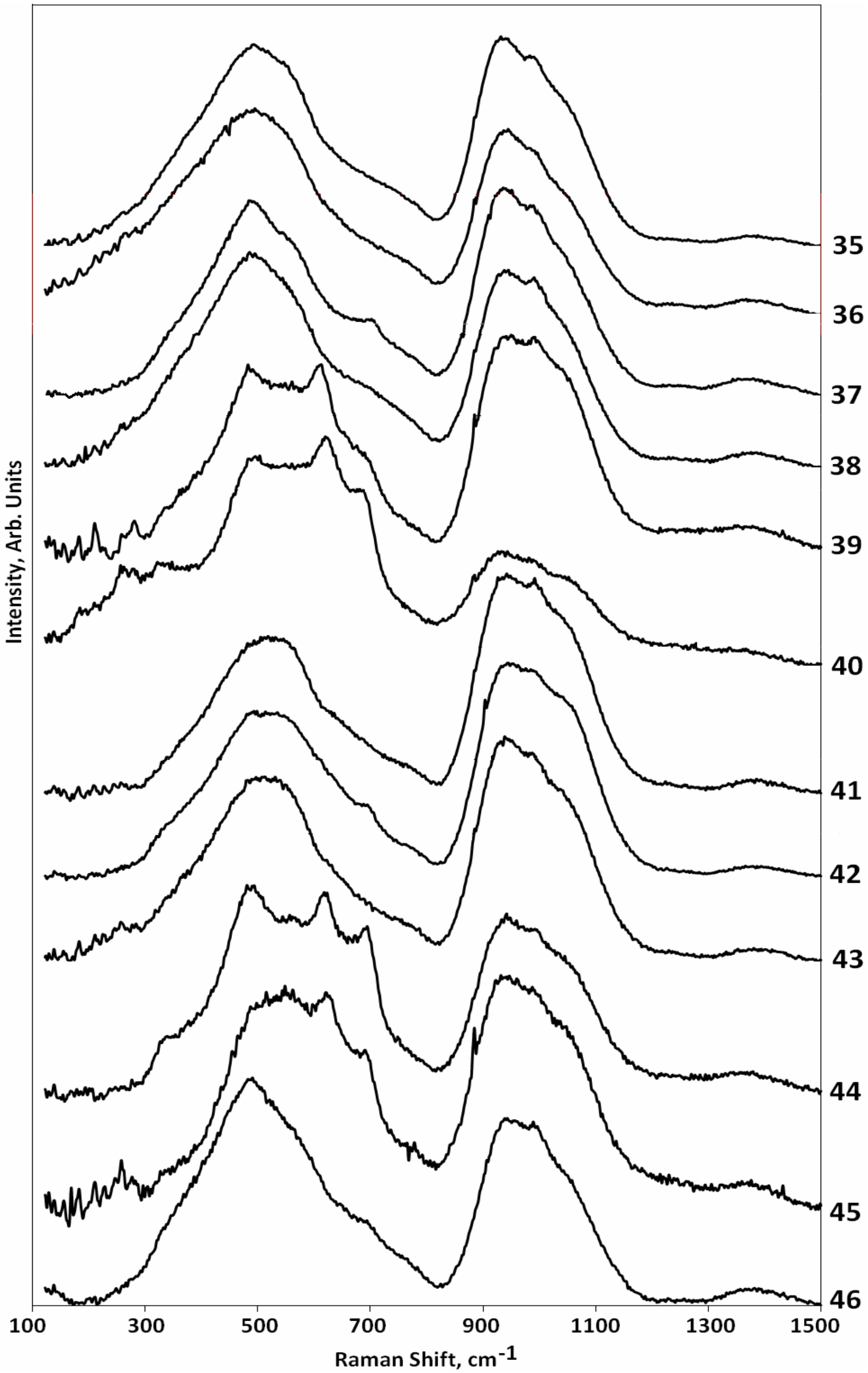

Figure 17. Depolarized Raman spectra of the samples.

All the spectra consist of the bands within the ranges of 300-600 cm^{-1}, 800-1150 cm^{-1} and weak bands at 650-800 cm^{-1} and 1200-1300 cm^{-1} and 1300-1500 cm^{-1}. Like in IR spectra these bands are due to bending and stretching modes in silicon-oxygen network, and vibrations in AlO_4, FeO_4 and BO_3 units. In the whole Raman spectroscopic data are in a good agreement with IR spectroscopic data but computer fitting allows to distinguishing more details (Figures 18-29).

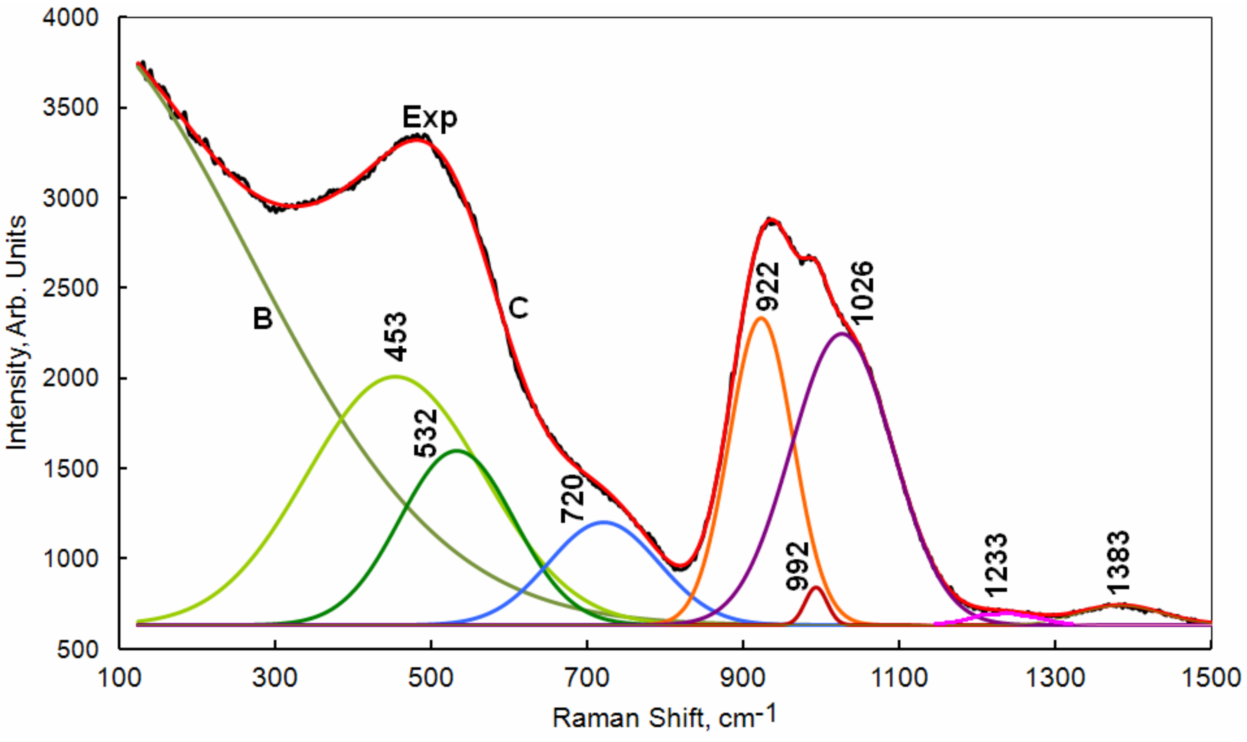

Figure 18. Computer fitting of the Raman spectra of the sample #35.

In the spectrum of the glassy material #35 (Figure 18) strong bands with maxima at 453 cm^{-1}, 922 cm^{-1} and 1026 cm^{-1} are due to bending and stretching modes in SiO_4 tetrahedra and bridging bonds Si—O—Si bonding SiO_4 tetrahedra. Some contribution to the band with maximum at 922 cm^{-1} may be made by vibrations of Si—O—Al and Si—O—Fe bridging bonds. The latter were suggested to be responsible for the band with a maximum at 910 cm^{-1} observed in Raman spectra of Fe-containing silicate glasses [11]. If so, the contribution of such bonds is rather minor because of low Fe_2O_3 content in glass. The band with a maximum at 532 cm^{-1} may be assigned to bending vibrations of Si—O—Si (ν_4) Si—O—Al and Si—O—Fe bridging bonds. The band with a maximum at 720 cm^{-1} is due probably to bending modes in AlO_4 tetrahedra. Weak bands at 1383 cm^{-1} and 1233 cm^{-1} are due to vibrations in BO_3 units with various degree of polymerization. The band at 1233 cm^{-1} may be also attributed to stretching vibrations of B^{III}—O—B^{IV} bridging bonds. Since glass #35 has a value of ψ_B factor equal to approximately 2 weak band with a maximum at 992 cm^{-1} may be assigned to stretching vibrations in BO_4 tetrahedra.

Glass #36 has higher B_2O_3 content (8.62 mol.%) and lower ψ_B value than the glass #35 (Table II). Therefore, fraction of trigonally-coordinated boron in them should be higher. It is seen well that intensities of the bands with maxima at 1241 cm^{-1} and 1376 cm^{-1} are higher than in the spectrum of the glass #35 (Figure 19). In the whole the spectra of both glasses are similar and differ slightly only in maxima of the bands.

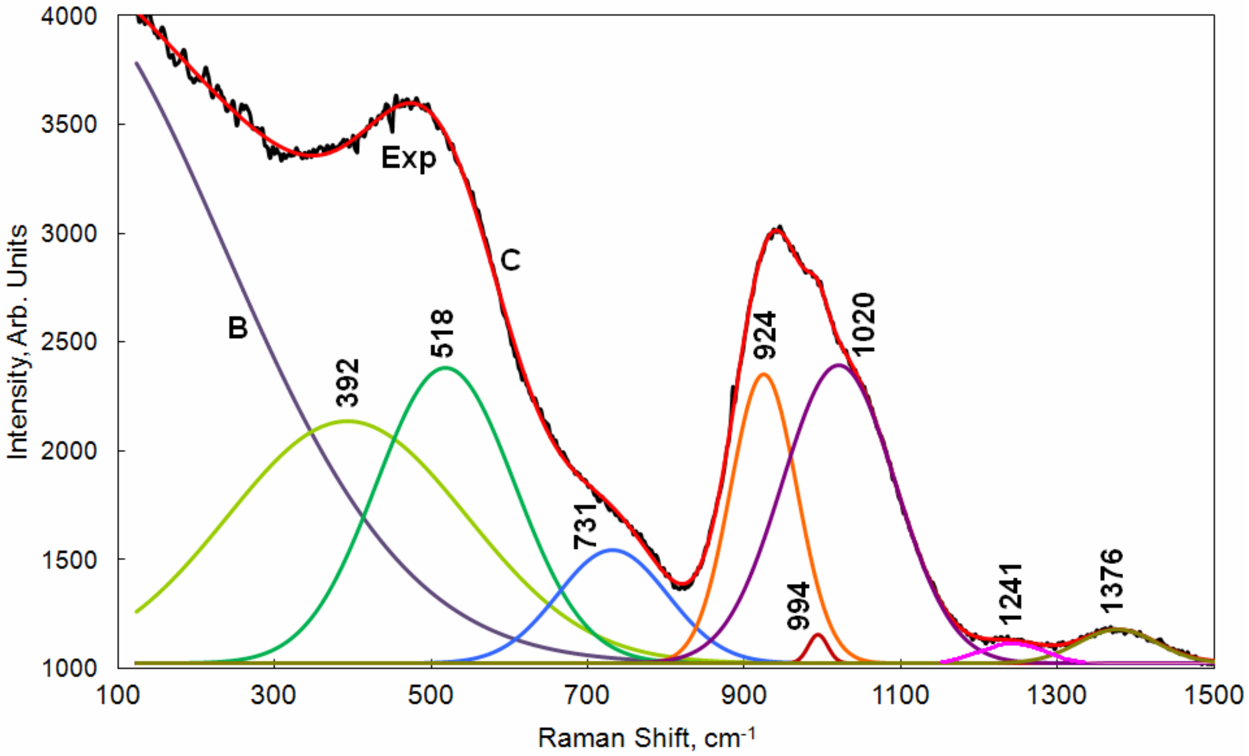

Figure 19. Computer fitting of the Raman spectra of the sample #36.

The spectrum of the glass #37 is some more complicated (Figure 20). Except the bands observed in the spectra of the samples #35 and #36 (maxima at 503 cm^{-1}, 924 cm^{-1}, 994 cm^{-1}, 1020 cm^{-1}, 1241 cm^{-1} and 1376 cm^{-1}) additional bands with maxima 346 cm^{-1}, 486 cm^{-1} were found. The band at 650-800 cm^{-1} is split into two components: 700 cm^{-1} and 771 cm^{-1}. Weak bands at 346 cm^{-1}, 486 cm^{-1} and stronger band with a maximum at 700 cm^{-1} may be attributed to vibrations in AlO_6, AlO_5 and AlO_4 polyhedra. The band with a maximum at 771 cm^{-1} is due probably to symmetric stretching (ν_1) modes in SiO_4 tetrahedra.

The spectrum of the glass #38 (Figure 21) is similar to those of the glasses #35 (Figure 18) and #36 (Figure 19). The difference between them is in positions of maxima of the bands. In the spectrum of the glass #38 they are as follows: 348 cm^{-1}, 507 cm^{-1}, 714 cm^{-1}, 923 cm^{-1}, 995 cm^{-1}, 1022 cm^{-1}, 1235 cm^{-1}, and 1383 cm^{-1}. If attribution of the bands with maxima at 507 cm^{-1}, 714 cm^{-1}, 923 cm^{-1}, 1022 cm^{-1}, 1235 cm^{-1}, and 1383 cm^{-1} is rather unambiguous, then assignment of the bands with maxima at 348 cm^{-1} and 995 cm^{-1} is indefinitive. As in the spectrum of other glasses the band with a maximum at 995 cm^{-1} may be due to stretching vibrations in BO_4 tetrahedra or Si—O—B bridging bonds. This band has low intensity that is consistent well with low B_2O_3 content in glasses.

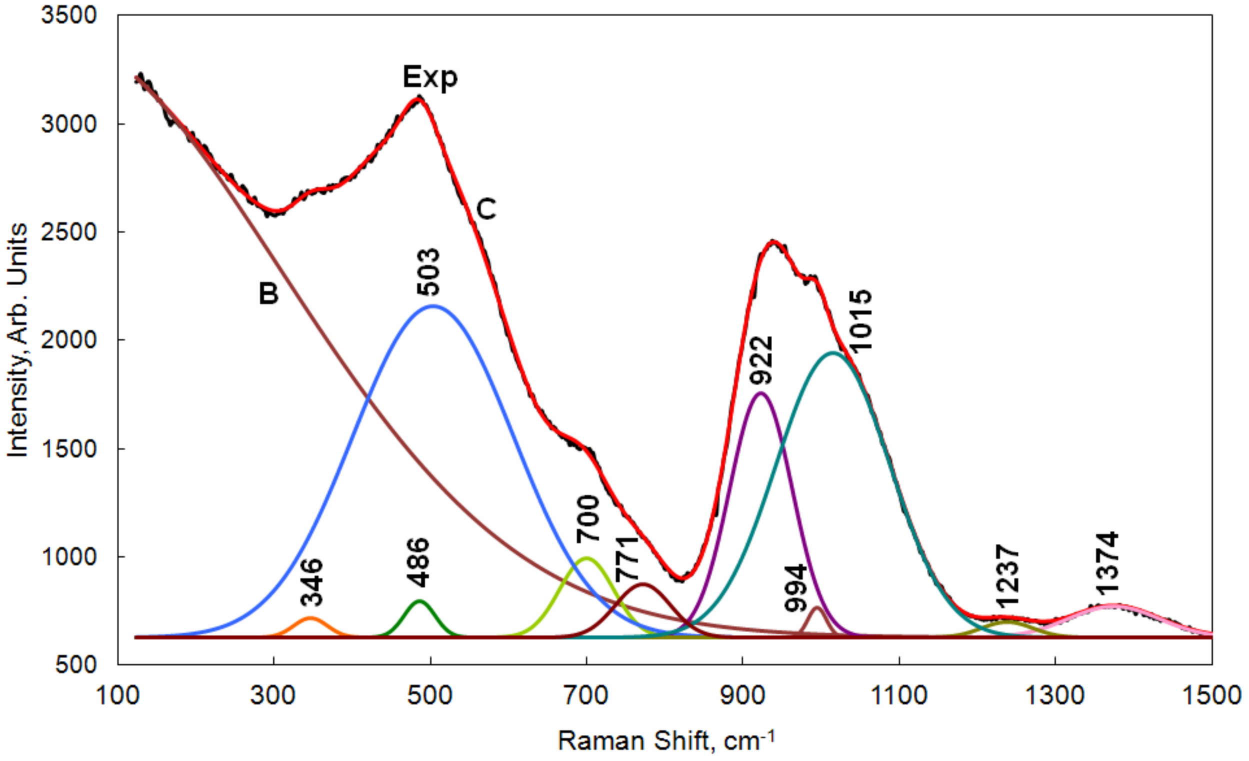

Figure 20. Computer fitting of the Raman spectra of the sample #37.

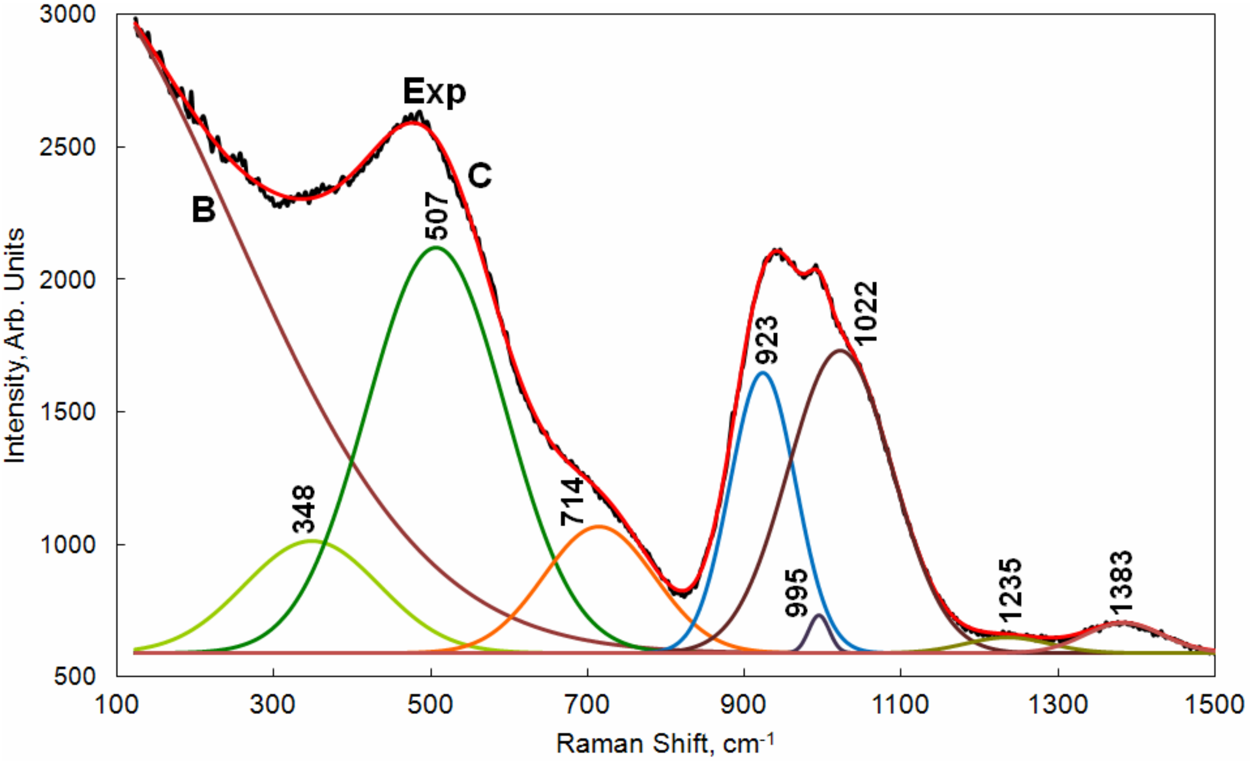

Figure 21. Computer fitting of the Raman spectra of the sample #38.

Raman spectrum of the glass #39 (Figure 22) is markedly different from spectra of previous glasses. Along with the bands observed in spectra of other glasses (539 cm^{-1}, 935 cm^{-1}, 993 cm^{-1}, 1030 cm^{-1}, 1246 cm^{-1}, 1386 cm^{-1}) it contains weak bands with maxima at 480 cm^{-1}, 613 cm^{-1}, 687 cm^{-1}, and 890 cm^{-1}. The first three bands may be assigned to vibrations in AlO_6, AlO_5 and AlO_4 polyhedra, whereas the band with a maximum at 890 cm^{-1} – to stretching vibrations of Si—O—Al bridging bonds.

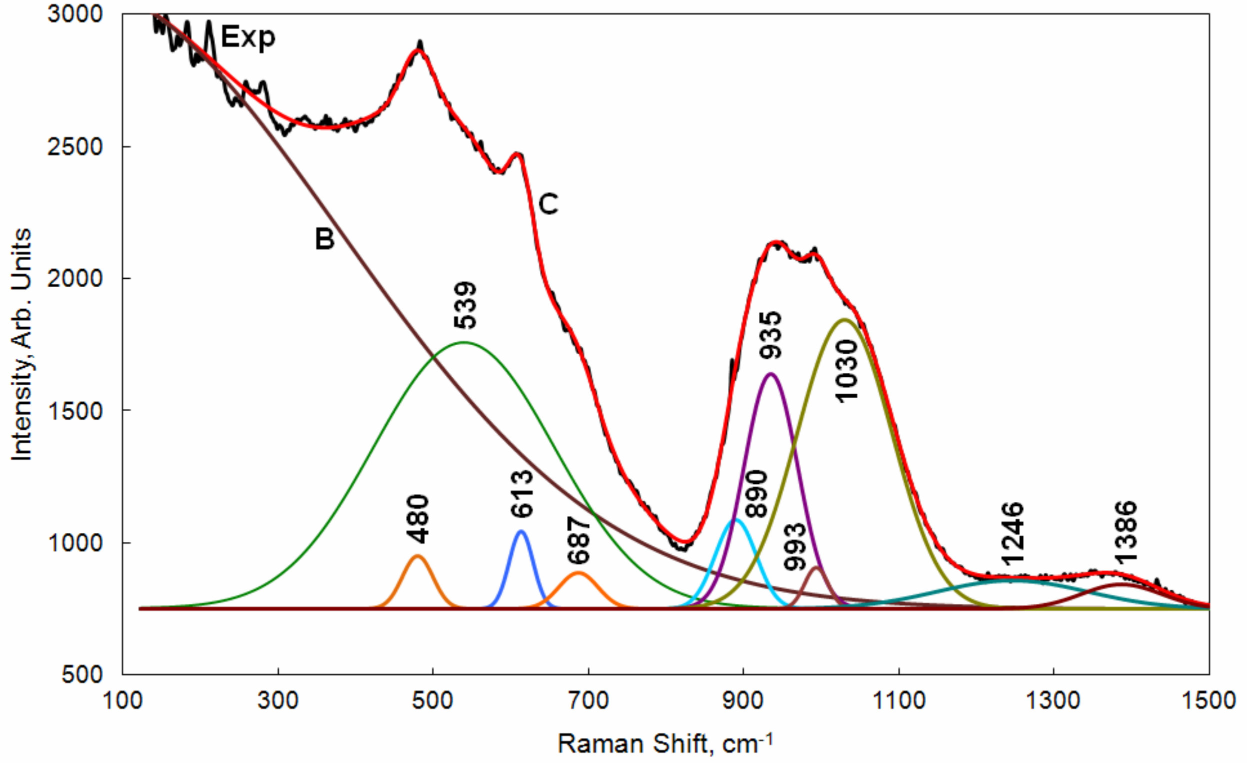

Figure 22. Computer fitting of the Raman spectra of the sample #39.

Raman spectrum of the glass #40 consists of numerous bands: strong broad with maxima at 327 cm^{-1}, 570 cm^{-1}, 751 cm^{-1}, 924 cm^{-1}, 1045 cm^{-1}, moderate narrow with maxima at 479 cm^{-1}, 629 cm^{-1}, 687 cm^{-1}, weak narrow with a maximum at 991 cm^{-1}, and weak broad with maxima at 1202 cm^{-1} and 1378 cm^{-1} (Figure 23).

Similarly to the previous spectra the bands with maxima at 570 cm^{-1}, 751 cm^{-1}, 924 cm^{-1}, and 1045 cm^{-1} are due to bending and stretching modes in SiO_4 tetrahedra and bridging bonds Si—O—Si, Si—O—Al and Si—O—Fe; the bands with maxima at 479 cm^{-1}, 629 cm^{-1} and 687 cm^{-1} are due to vibrations in AlO_6, AlO_5 and AlO_4 polyhedra, and bands with maxima at 991 cm^{-1}, and weak bands with maxima at 991 cm^{-1}, 1202 cm^{-1} and 1378 cm^{-1} are due to vibrations in boron-oxygen constituent of glass network.

The spectrum of the glass #41(Figure 24) within the range of 850-1200 cm^{-1} is similar to that of glass #39 (Figure 22). Therefore attribution of the bands may be same. The range lower 850 cm^{-1} may be interpreted as superposition of strong band due to bending vibrations in SiO_4 tetrahedra and bridging bonds Si—O—Si(Al,Fe) and weak bands due to vibrations in MeO_x polyhedra.

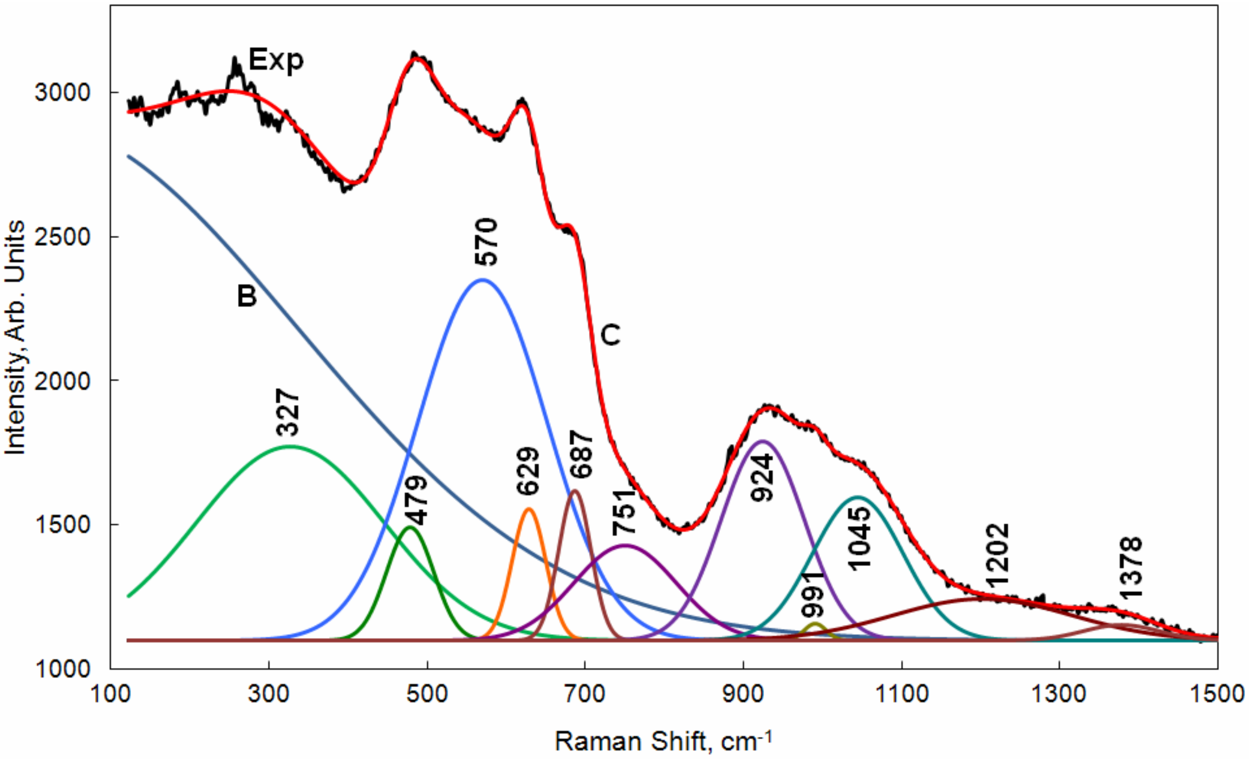

Figure 23. Computer fitting of the Raman spectra of the sample #40.

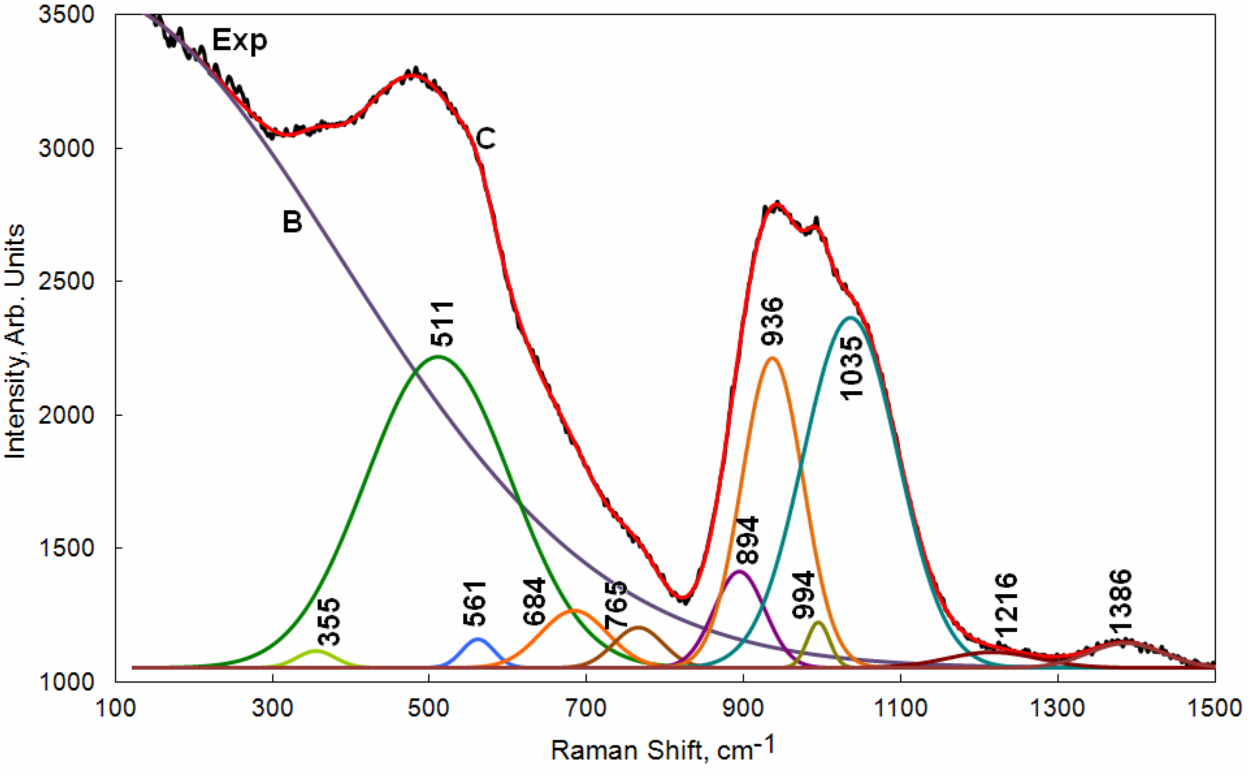

Figure 24. Computer fitting of the Raman spectra of the sample #41.

The spectrum of the glasses #42 (Figure 25), #43 (Figure 26) and #48 (Figure 29) like the spectra of other glasses in the same group may be decomposed into the bands due to stretching and bending vibration in silica-oxygen, aluminum-oxygen, iron-oxygen, and boron-oxygen polyhedra.

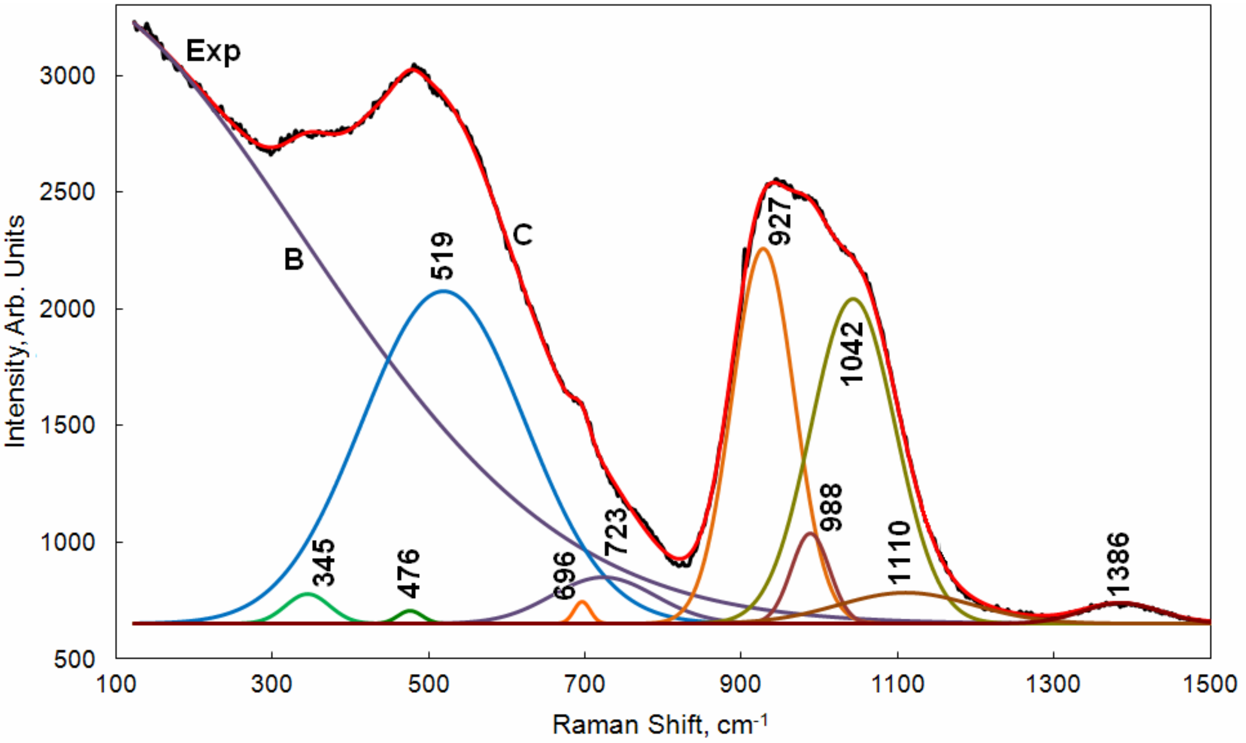

Figure 25. Computer fitting of the Raman spectra of the sample #42.

A set of the bands obtained by resolving the spectra of the glasses #39 (Figure 22), #40 (Figure 23), #44 (Figure 27), and #45 (Figure 28) within th rang of 850-1200 cm^{-1} into components is similar to those obtained from the spectra of glasses belonging to different group. The difference is within the range of 300-850 cm^{-1} where numerous bands are required to achieve good alignment between experimental and fitted spectra.

In the whole, for the spectra of all the glasses within the range of 850-1200 cm^{-1} the best fit is achieved in suggestion of overlapping of three major components with maxima at 911-936 cm^{-1}, 988-996 cm^{-1} and 1020-1045 cm^{-1}. For the best fit of spectra of the glasses #39 and #41 additional line with a maximum at 890-894 was required. So, it can be concluded that the structure of glasses is composed of metasilicate chains and rings containing incorporated AlO_4 and FeO_4 as well as minor BO_4 tetrahedra. Major BO_4 tetrahedra and BO_3 triangles form complex borate units and are present as separate constituent.

Computer fitting of the range of 300-850 cm^{-1} is much more complicated. This range consists of numerous bands due to bending vibrations in silicon-oxygen network with incorporated MeO_4 tetrahedra, symmetric stretching vibrations in silicon-oxygen network and stretching vibrations

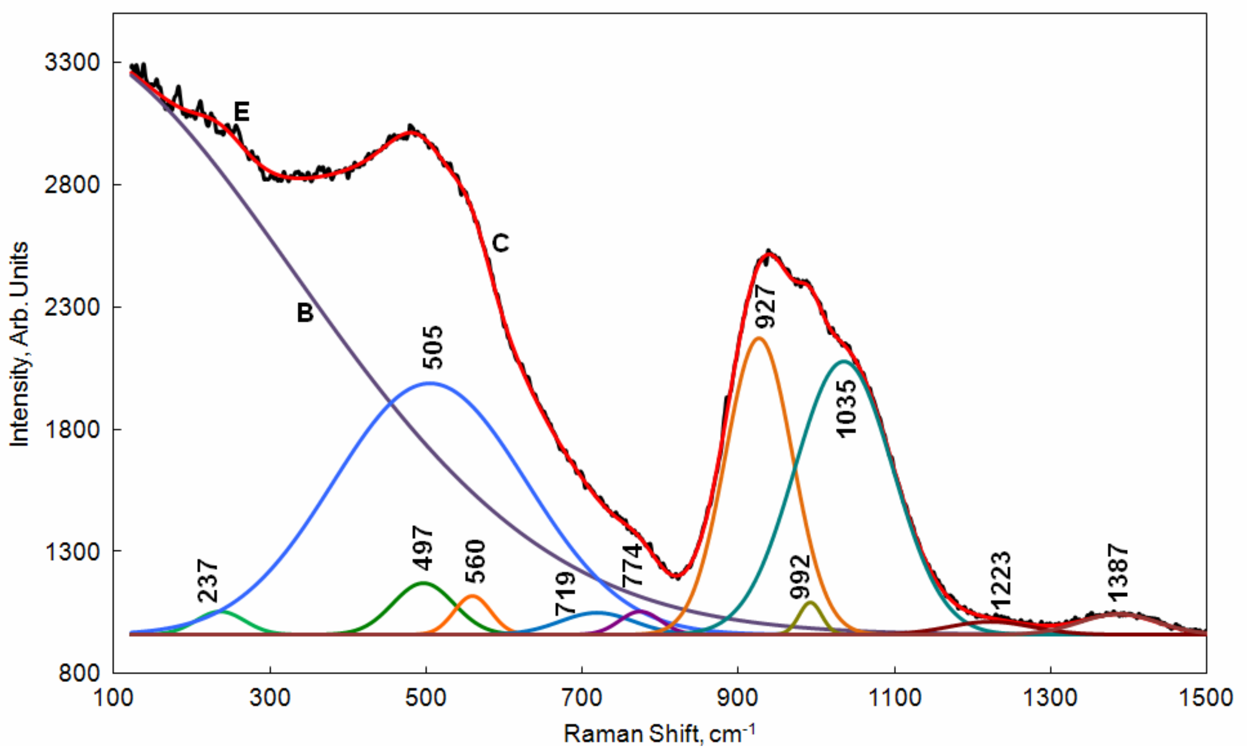

Figure 26. Computer fitting of the Raman spectra of the sample #43.

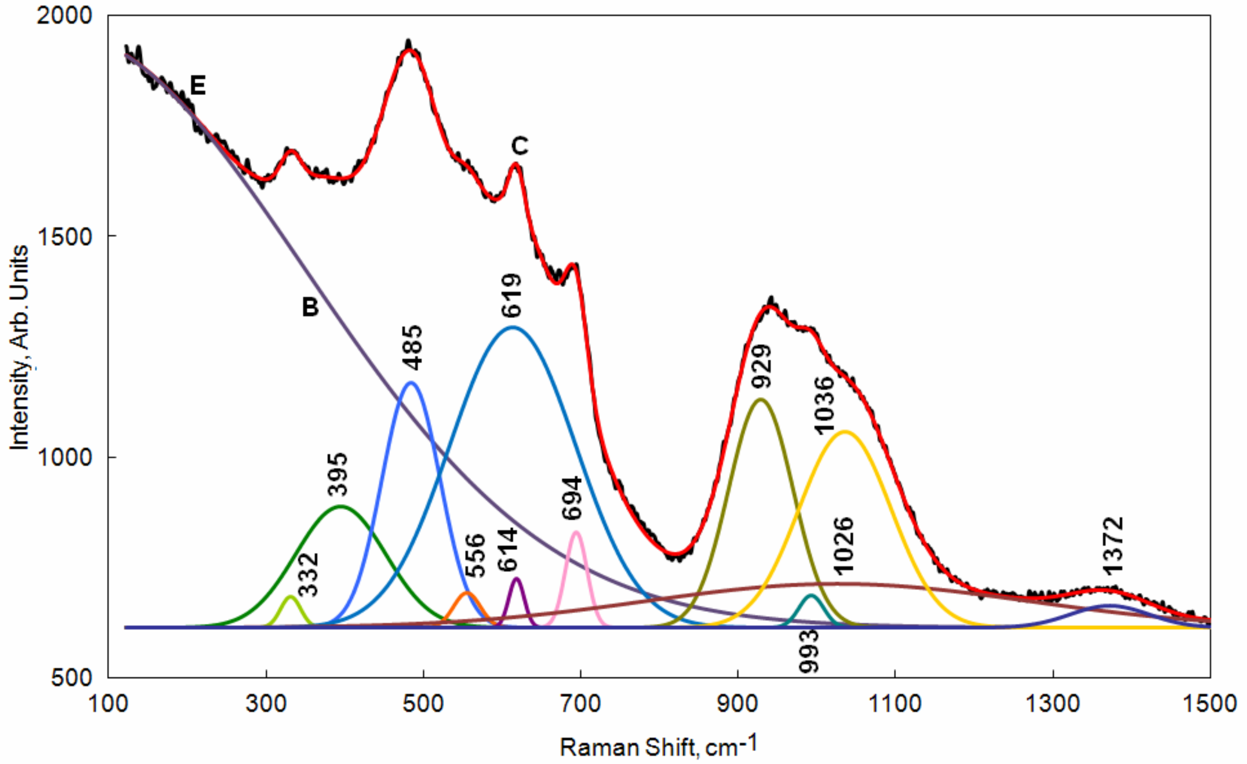

Figure 27. Computer fitting of the Raman spectra of the sample #44.

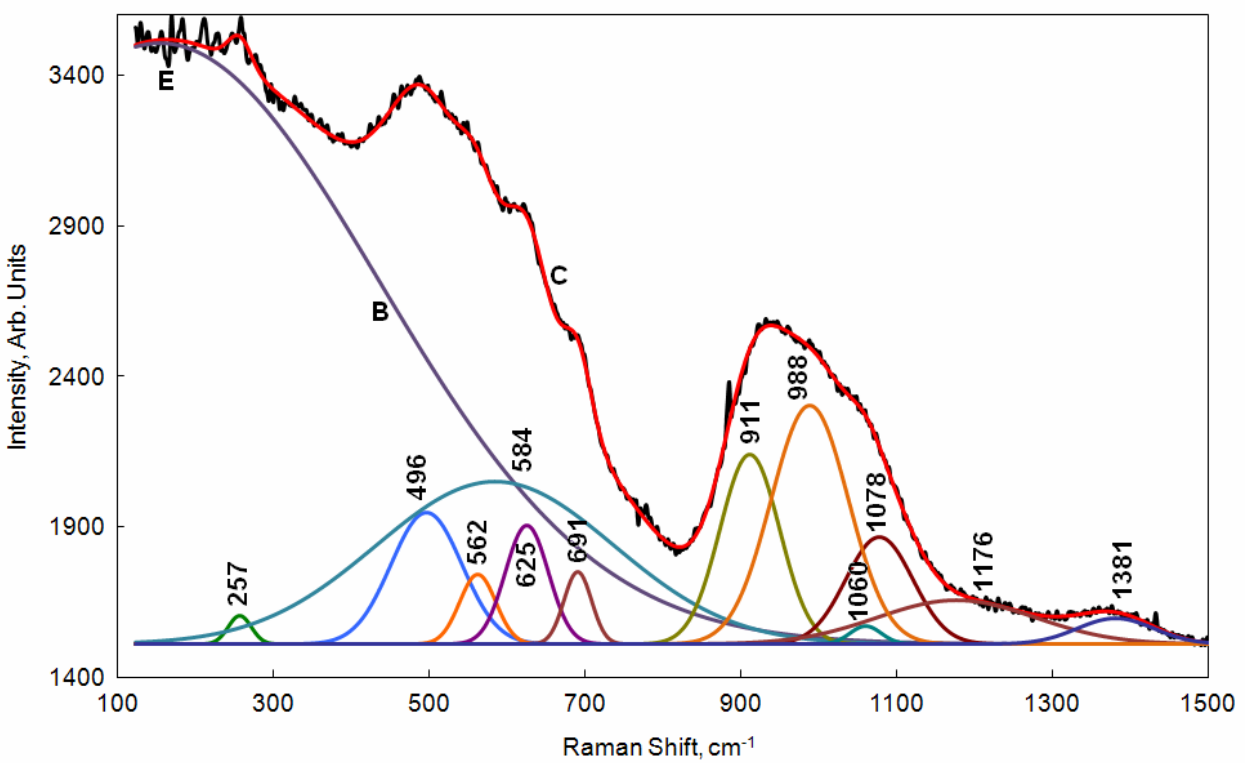

Figure 28. Computer fitting of the Raman spectra of the sample #45.

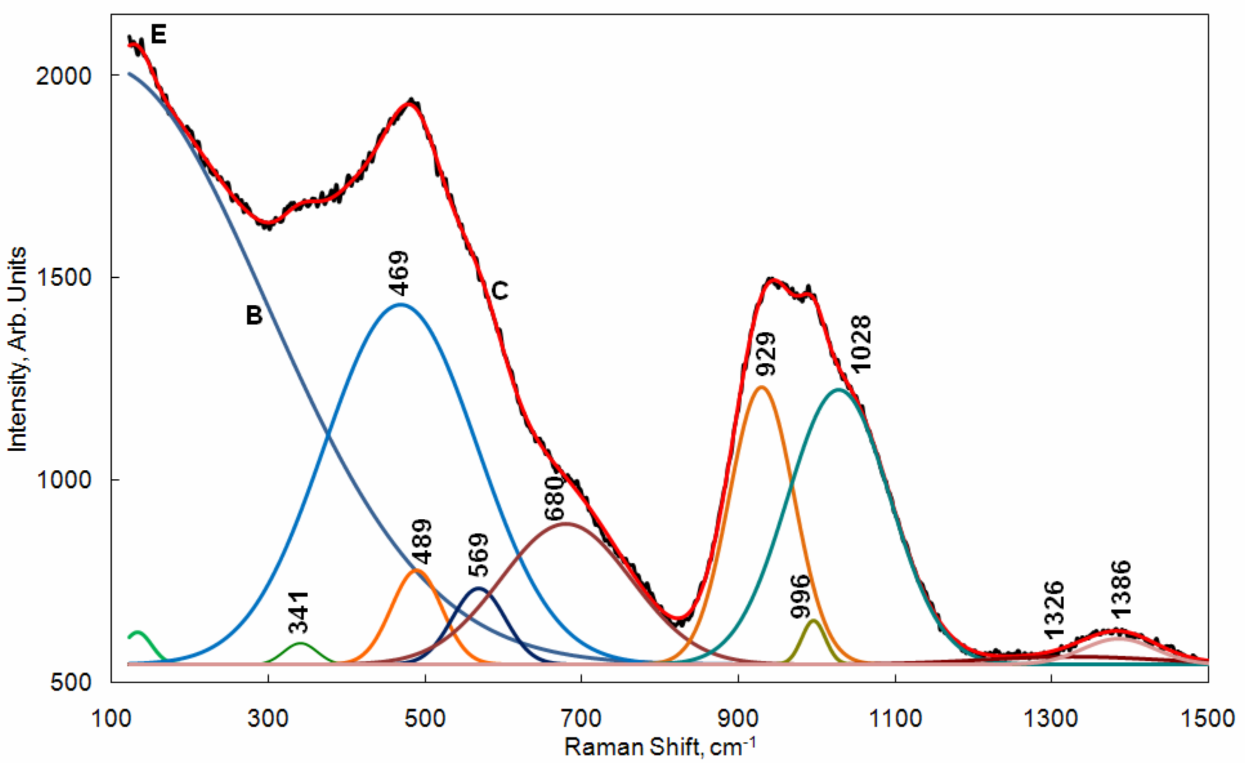

Figure 29. Computer fitting of the Raman spectra of the sample #46.

of Me—O bonds in MeO_n polyhedra as well the bands due to stretching and bending vibrations of Me—O bonds in spinel. This makes attribution of the bands in this range rather difficult and ambiguous.

Nevertheless some general suggestions concerning attribution of the bands within this range may be done. If to compare Raman spectra of the glasses #45 (Figure 28) and #46 (Figure 29) related to two different groups, then we can see some similarity in behavior of the bands: i) occurrence of strong broad band due to bending vibrations of the bonds in silica-oxygen network and bridging bands Si—O—Me bonding SiO_4 and MeO_4 tetrahedra; ii) occurrence of the bands with maxima at 496 cm^{-1} or 489 cm^{-1} and 562 cm^{-1} or 569 cm^{-1} (for the glasses #45 and #46, respectively). At the same time the spectrum of the glass #46 contains broad band centered at 680 cm^{-1} whereas in the spectrum of the glass #45 weak narrow band centered at 691 cm^{-1} is present. Moreover the spectrum of the glass #45 contains an additional narrow band centered at 625 cm^{-1}. If broad bands are due mainly to vibrations in low-symmetry structural units in random glass network, then narrow band are due probably to vibrations in high-symmetry structural units of the spinel structure phase.

Chemical composition of spinel may be represented by general formula $(Mg,Mn,Ni,Cu)^{2+}(Fe,Al)^{3+}O_4$. Taking into account low MgO, NiO and CuO contents, major contribution to these bands make vibration of Fe—O and Al—O bonds in FeO_4 and AlO_4 tetrahedra, and in much less extent, Mn—O and Fe—O bonds in MnO_6 and FeO_6 octahedra. Thus, the bands within the range of 300-500 cm^{-1} may be associated with vibrations of Mn—O and Fe—O bonds in MnO_6 and FeO_6 octahedra in the spinel structure. The bands at 550-650 are due mainly to vibrations of Fe—O bonds in FeO_4 tetrahedra in both spinel and glass structures and, in some extent in FeO_6 octahedra. Vibrations of Al—O bonds in AlO_4 tetrahedra in both spinel and glass are positioned at 650-750 cm^{-1}. For more precise simulation of the spectra within the range of 300-850 cm^{-1} special studies with the use of model compounds (surrogates) with the known structure are required.

XAS study

XAS spectrum of Fe K-edge was found to be the same in all the glasses studied (Figure 30). This spectrum corresponds to Fe^{3+} ions in mixed octahedral and tetrahedral surrounding [12]. EXAFS (Figure 31) and Fourier transform of EXAFS spectrum demonstrate that only first coordination shell is appeared whereas contributions from the second and subsequent shells are negligible. This shows the Fe^{3+} ions are rather homogeneously distributed in glass and fraction of spinel is minor.

Nevertheless the peak due to the first coordination shell is markedly asymmetric (Figure 32). Results of computer fitting of major peak are given in Table III.

Table III. Fitting of the Fe K Edge EXAFS Spectra of Glasses.

Bond	Distance, Å	Coordination Number	Debye-Waller Factor
Fe—O_1	1.74±0.02	1.6±0.2	0.003
Fe—O_2	1.94±0.02	2.4±0.2	0.003
Fe—O_3	2.07±0.02	5.9±0.3	0.004

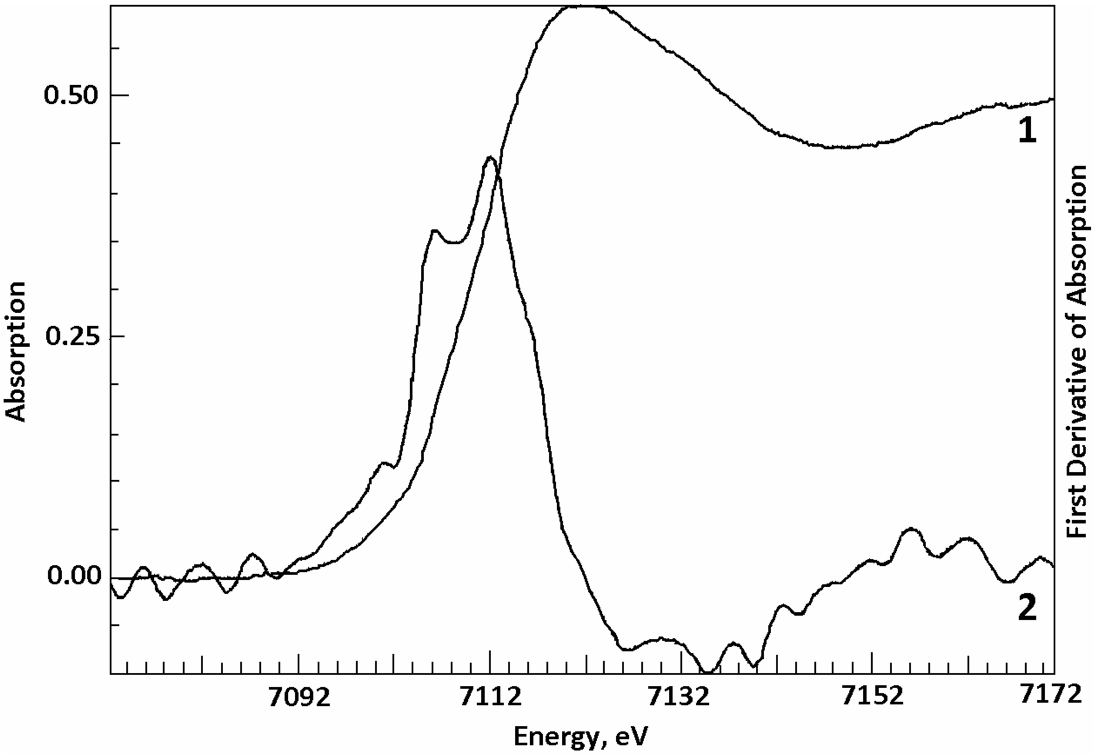

Figure 30. XAS (1) spectra of Fe K-edge and its XANES range (2) of the glasses.

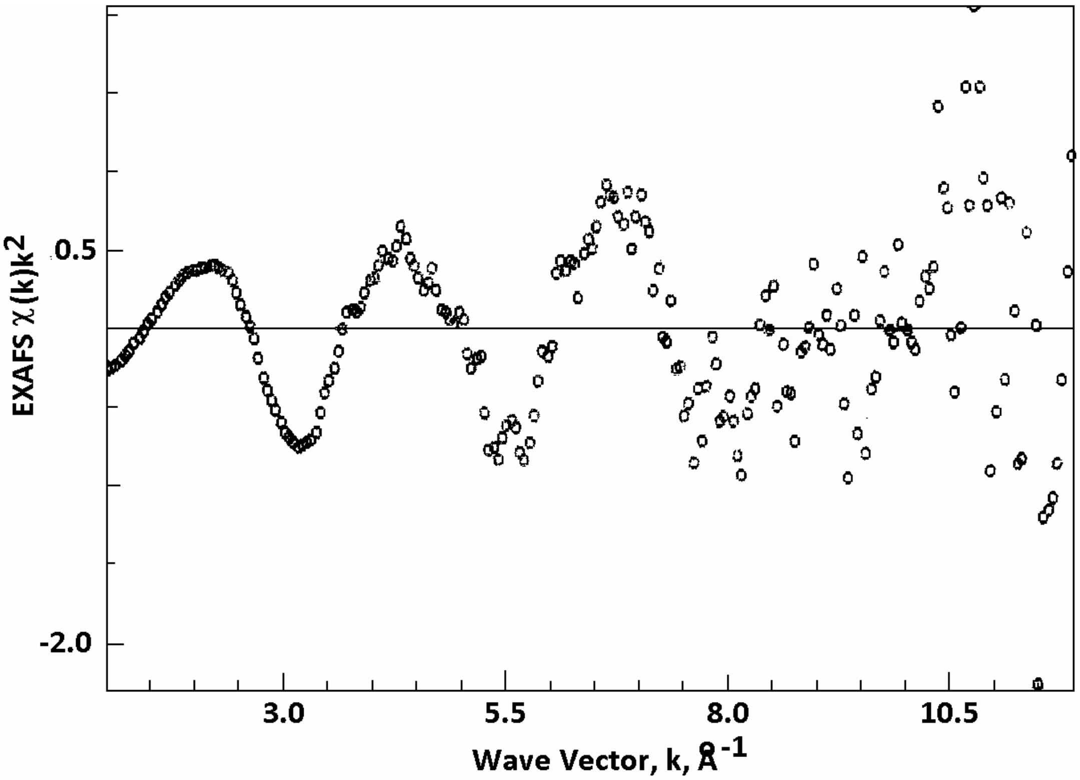

Figure 31. EXAFS of Fe K-edge of glasses.

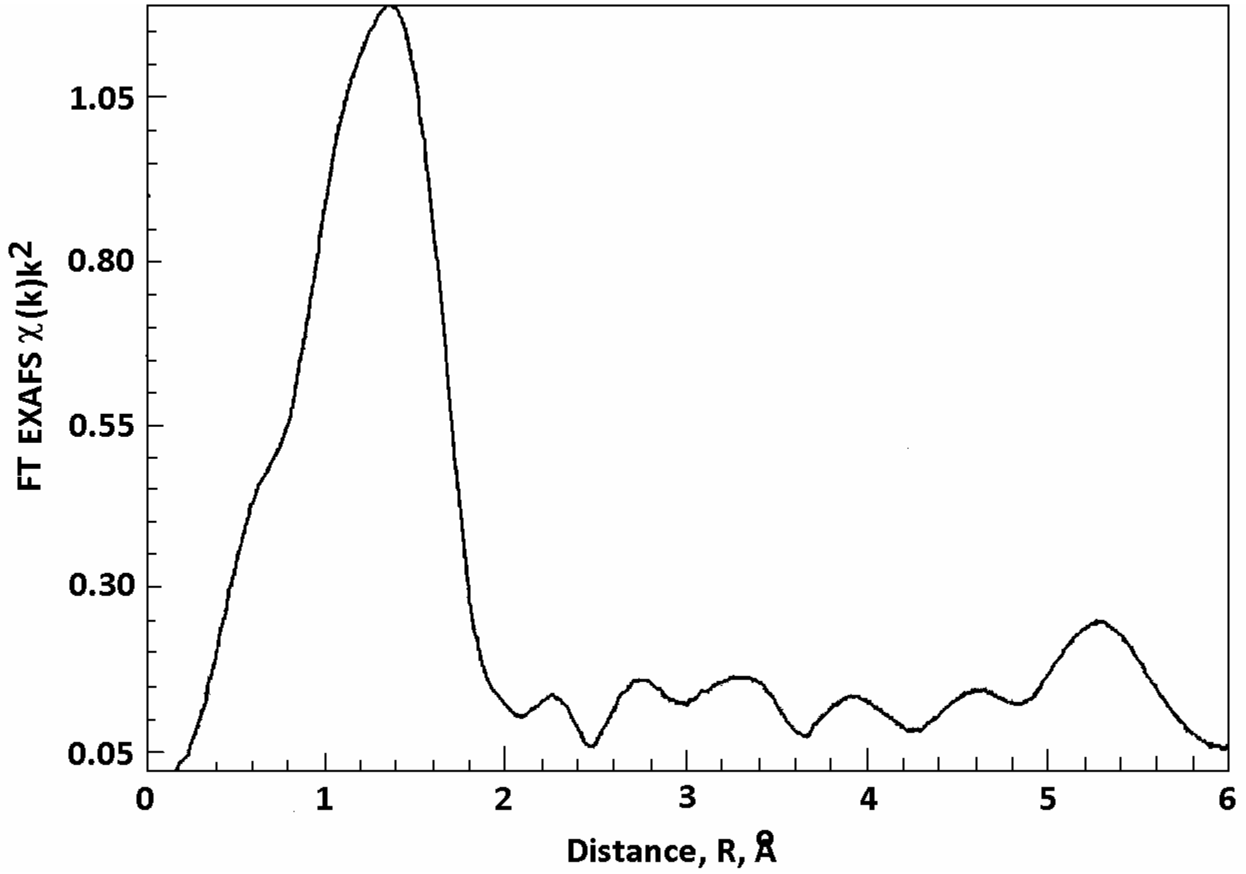

Figure 32. Fourier Transform of EXAFS Fe K-edge spectrum of glasses.

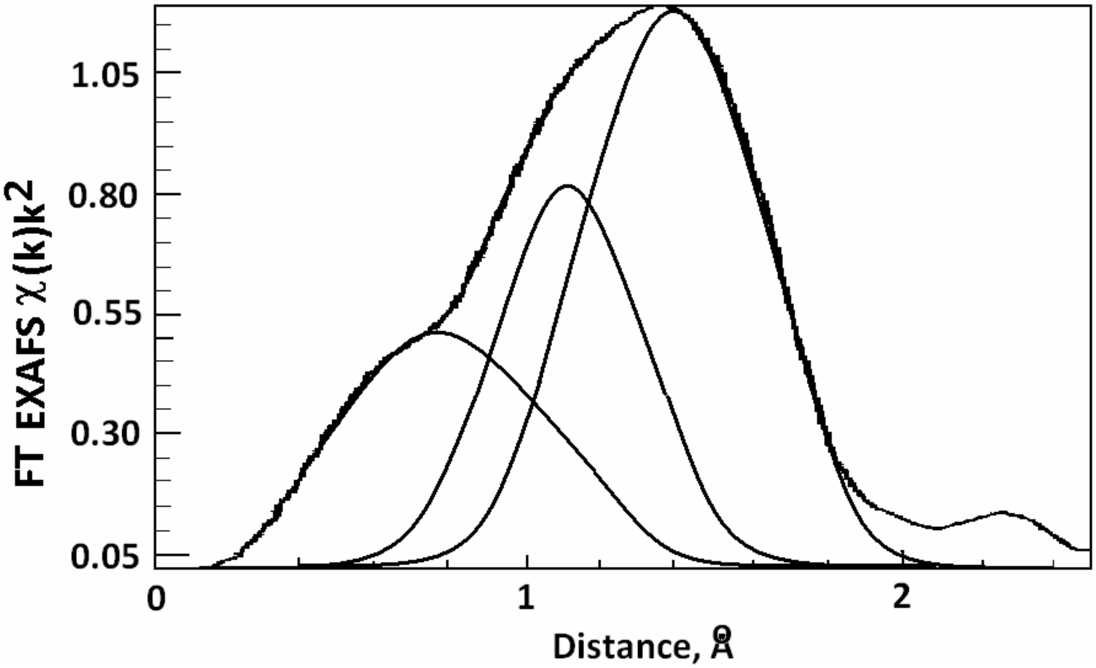

Figure 33. Computer fit of major peak in EXAFS spectrum of Fe K-edge in glasses.

The first two distances are due to Fe—O bonds in distorted tetrahedron. The third Fe—O distance is close to that in FeO_6 octahedra [13]. Contribution due to Fe—O distances in spinel is very low.

CONCLUSIONS

All the glasses studied are composed of predominant vitreous phase and minor spinel structure phase. Spinel forms both isometric grains and cubic microcrystals (~1 μm). Microcrystals are aggregated in bands with variable glass and spinel contents. IR and Raman spectroscopic study the structure of all the glasses are similar and is composed of metasilicate chains and rings containing incorporated AlO_4 and FeO_4 as well as minor BO_4 tetrahedra. FeO_6 octahedral units may be also present. In the structure of all the glasses trigonally-coordinated boron dominats over tetragonally-coordinated. At that, major BO_4 tetrahedra and BO_3 triangles form complex borate units and are present as separate constituent.

As follows from XAS data, iron is predominantly present as Fe^{3+} ions. Major Fe^{3+} ions are tetrahedrally-coordimated and built in silicon-oxygen network. Minor Fe^{3+} ions are octahedrally-coordinated and may be considered as network-modifiers. Contribution due to spinel is negligible.

REFERENCES

1. A.A. Appen, *Chemistry of Glass* (Russ.), Khimiya, Leningrad (1974).
2. B. Ravel and M. Newville, *J. Synchrotron Radiat.* **12** 537-541 (2005).
3. A.L. Ankudinov and J.J. Rehr, *Phys. Rev.* B **56** 1712-1716 (1997).
4. H. Funke, A.C. Scheinost and M. Chukalina, *Phys. Rev. B*, **71**, 094110 (2005).
5. H. Funke, M. Chukalina and A.C. Scheinost, *J. Synchrotron Radiat.* **14**, 426-432 (2007).
6. www.esrf.fr/exp_facilities/BM20/Software/Wavelets.html.
7. V.A. Kolesova, *Glass Phys. Chem.* (Russ.) **12** [10] 4-13 (1986).
8. V.N. Anfilogov, V.N. Bykov, and A.A. Osipov, *Silicate Melts* (Russ.), Nauka, Moscow (2005).
9. I.I. Plyusnina, *Infrared Spectra of Minerals* (Russ.), MGU, Moscow (1977).
10. K. Nakamoto, *Infrared Spectra of Inorganic and Coordination Compounds*, John Wiley & Sons, Inc. New York – London (2009).
11.
12. G.E. Brown, Jr., G.A. Waychunas, C.W. Ponader, W.E. Jackson, and D.A. McKeown, *EXAFS and Near Edge Structure IV – J. de Physique*. **47** C8, suppl. Au n°12, C8-661 – C8-668 (1986).
13. G. Licheri, G. Paschina, G. Piccaluga, G. Pinna, M. Magini, and G. Cocco, *J. Non-Cryst. Solids*, 72, 211-220 (1985).

Distribution:

J. W. Amoroso, 999-W
A. B. Barnes, 999-W
A. L. Billings, 999-W
A. S. Choi, 773-42A
Y. T. Collazo, DOE-EM
C. L. Crawford, 773-42A
D. A. Crowley, 773-43A
S. D. Fink, 773-A
B. J. Giddings, 786-5A
A. M. Han, DOE-EM
C. C. Herman, 999-W
C. M. Jantzen, 773-A
F. C. Johnson, 999-W
J. C. Marra, 773-42A
S. L. Marra, 773-A
D. H. Miller, 999-W
D. K. Peeler, 999-W
F. M. Pennebaker, 773-42A
S. P. Schneider, DOE-EM
G. L. Smith, DOE-EM
J. D. Vienna, PNNL